UNIVERSITY OF SOUTHAMPTON

FACULTY OF PHYSICAL AND APPLIED SCIENCES

Electronics and Computer Science

Modelling Partial Discharge in Gaseous Voids

by

George Callender

Thesis for the degree of Doctor of Philosophy

March 26, 2018

UNIVERSITY OF SOUTHAMPTON

ABSTRACT

FACULTY OF PHYSICAL AND APPLIED SCIENCES
Electronics and Computer Science

Doctor of Philosophy

MODELLING PARTIAL DISCHARGE IN GASEOUS VOIDS

by George Callender

The measurement of partial discharge (PD) activity is a commonly used tool to quantify the health of electrical insulation material in high voltage plant. Models of PD activity have been developed in order to provide insight into the physical conditions present in PD systems. Modern PD models typically use the approach taken in the work of Niemeyer in early 1990's, and so far have been primarily limited to investigating PD activity from simple controlled experiments. PD models have typically focused on PD activity in gaseous voids, which is also the case in this thesis.

In this work a new PD activity model was developed. It addressed several of the shortcomings present in other PD activity models in order to provide a more physically accurate description of PD phenomena and to extend the scope of the model. The model was validated against experimental data in the literature, and was then used to simulate PD activity from a three-phase cable experiment, which is indicative of the more complex PD systems present in operational plant. However, despite this contribution it became evident that many of the assumptions and concepts used in the model, despite having a basis in the literature, have limited justification.

A drift diffusion model was then used to test some of the physical concepts that are employed when modelling PD in voids. The results showed that many of these concepts may be erroneous, with discrepancies between the canonical reasoning and the simulation results. For example, the residual electric field, the electric field after a discharge, is significantly lower than the estimates used by PD activity models in the literature. It is concluded that in their current form PD activity models may not be fit for purpose, and it is suggested that a new approach to modelling PD activity is required moving forward.

Contents

Declaration of Authorship

I, George Callender , declare that the thesis entitled *Modelling Partial Discharge in Gaseous Voids* and the work presented in the thesis are both my own, and have been generated by me as the result of my own original research. I confirm that:

- this work was done wholly or mainly while in candidature for a research degree at this University;
- where any part of this thesis has previously been submitted for a degree or any other qualification at this University or any other institution, this has been clearly stated;
- where I have consulted the published work of others, this is always clearly attributed;
- where I have quoted from the work of others, the source is always given. With the exception of such quotations, this thesis is entirely my own work;
- I have acknowledged all main sources of help;
- where the thesis is based on work done by myself jointly with others, I have made clear exactly what was done by others and what I have contributed myself;
- parts of this work have been published as:

    1. G. Callender, J.A. Hunter, P. Rapisarda, and P.L. Lewin. Physical models for field based partial discharge measurements. In Electrical Insulation Conference, 2015. EIC 2015. IEEE, June 2015.
    2. G. Callender, P. Rapisarda, and P.L. Lewin. Investigating the dependence of partial discharge activity on applied field structure. In Electrical Insulation Conference, 2016. EIC 2016. IEEE, June 2016.
    3. G. Callender, P. Rapisarda, and P.L. Lewin. Investigation of void erosion on partial discharge activity using simulation. In International Conference on Dielectrics, 2016. ICD 2016. IEEE, July 2016.
    4. G. Callender, P.L. Lewin, J.A. Hunter, and P. Rapisarda. Modeling partial discharge in a three-phase cable joint experiment with minimal adjustable parameters. IEEE Transactions on Dielectrics and Electrical Insulation, 24(1):279-287, 2017.

5. R.D. Nimmo, G. Callender, and P.L. Lewin. Methods for wavelet-based autonomous discrimination of multiple partial discharge sources. IEEE Transactions on Dielectrics and Electrical Insulation, 24(2):1131-1140, 2017

6. G. Callender, P. Rapisarda, and P.L. Lewin. Improving Models of Partial Discharge Activity using Simulation. In Electrical Insulation Conference, 2017. EIC 2017. IEEE, June 2017.

7. T. Tanmaneeprasert, P.L. Lewin and G. Callender. Analysis of Degradation Mechanisms of Silicone Insulation Containing a Spherical Cavity Using Partial Discharge Detection. In Electrical Insulation Conference, 2017. EIC 2017. IEEE, June 2017.

8. G. Callender, I.O. Golosnoy, P. Rapisarda, and P.L. Lewin. Critical analysis of partial discharge dynamics in air filled spherical voids. Journal of Physics D: Applied Physics, 51(12):125601, 2018.

Signed:.....

Date:.....

Acknowledgements

The completion of this thesis was greatly assisted by the support and friendship of a large number of people throughout my time at Southampton.

I am very grateful to my main supervisor, Prof. Paul Lewin, for his consistent support, the freedom he allowed me in my research and for his many insightful discussions. I am also thankful to his wife, Nicki Lewin, who suggested I pursue this subject area for my PhD in the first place. I would like to thank my secondary supervisor Prof. Paolo Rapisarda for his discussions and advice. I am indebted to Dr. Richard Chippendale, who was always available to discuss and assist with the many issues I encountered with COMSOL. The simulation files provided by Dr. Trung Nam Tran, along with the experimental data given to me by Dr. Jack Hunter and Thanarat Tanmaneeprasert, is also greatly appreciated and was invaluable to my research. My gratitude also goes to Prof. Igor Golosnoy and Dr. Kevin Goddard for their technical insight that significantly improved my own understanding. I am also grateful to Prof. George Chen and Prof. George Georghiou for acting as my viva examiners and their comments and suggestions which improved my thesis.

Throughout my research I have been continually assisted by the encouragement of my friends and family. I am eternally thankful for the love and support of my wife Helen, along with her sage advice to occasionally stop working. I am profoundly grateful for the love and good humour of my mother, Margaret, my father, Mark and my brother, Robert. A special mention must also go to my grandfather, George Harrison, for his enthusiasm and interest in my research. The companionship and advice of my good friend, Dr. Matthew Spencer, was also invaluable.

The financial support of EPSRC is gratefully acknowledged.

Nomenclature

This nomenclature lists all significant variables, parameters and acronymns used in this report. An overview of the notation used can be found in Appendix A

A_{gen}	Area covered by generation points (mm^2)
B	Ionisation parameter of air ($\text{m}^{1/2}$ $\text{Pa}^{1/2}$)
$c_{\alpha\, ijk}$	The constant of proportionality between the surface charge density at generation point i and the local electric field component at inception point j for the spatial distribution of surface charge k.
c_{e}	Free parameter in equation for electron generation rate from metallic surface (mm^3 kV^{-3})
$c_{\text{l}\, ijk}$	The constant of proportionality between the local electric field component at generation point i and the local electric field component at inception point j for the spatial distribution of surface charge k.
$c_{q'\, ij}$	The constant of proportionality between the local electric field component at inception point i and the apparent charge on the measuring electrode for the spatial distribution of surface charge j.
$\vec{D}$	Electric displacement field (nC mm^{-2})
D_{e}	Electron Diffusion Coefficient (m^2 s^{-1})
D_{phase}	Distance of phase centre from joint centre (mm)
d_{v}	Distance along the void surface
$\vec{E}_0$	Applied Electric field (kV mm^{-1})
$\vec{E}$	Electric field (kV mm^{-1})
E_{cr}	Critical Electric Field to maintain a discharge (kV mm^{-1})
E_{inc}	Inception Electric Field (kV mm^{-1})
E_{res}	Residual Electric Field (kV mm^{-1})
$\vec{E}_{\text{l}}$	Local Electric field (kV mm^{-1})

$\vec{e}$	Unit vector in a given direction
G	A region in the PD system
G_{v}	The void region in the PD system
L_{plate}	Separation between plate electrodes (mm)
I'	Apparent Current (mA)
J'	Apparent Current Density (mA)
L_{spike}	Spike length (mm)
m_{PSA}	PSA delay reconstruction vector size
$\vec{n}$	Normal unit vector to a surface
N_{dt}	Detrappable charge population
N_{gen}	Number of generation points
N_{inc}	Number of inception points
$\dot{N}_{\mathrm{e}}$	Electron Generation Rate (s^{-1})
n_{e}	Electron Number Density (m^{-3})
$\dot{N}_{\mathrm{e\ s}}$	Electron Generation Rate due to Surface Emission (s^{-1})
n_{n}	Negative Ion Number Density (m^{-3})
n_{p}	Positive Ion Number Density (m^{-3})
p	Pressure (kPa)
p_e	Probability a free electron is available
q'_{PD}	PD apparent charge (nC, pC or mV)
q_{PD}	PD physical charge (nC, pC or mV)
R	A random number selected from a uniform distribution between 0 and 1
r	Radial distance in spherical coordinates
r_{c}	Radial distance in cylindrical coordinates
R_{d}	Deformation radius (mm)
R_{joint}	Joint radius (mm)
R_{phase}	Phase radius (mm)
$R_{\mathrm{spike\ bottom}}$	Radius of the bottom of the spike conical frustum (mm)
$R_{\mathrm{spike\ top}}$	Radius of the top of the spike conical frustum (mm)
R_{v}	Radius of a spherical void (mm)
S_{ph}	Photoionisation Rate ($\mathrm{m}^{-3}\ \mathrm{s}^{-1}$)
T	Temperature (°C)

t	Time (s)
t_{AC}	Time in AC cycle when applied field is maximal (s)
t_{PD}	Time PD occurs (s)
U_0	Applied voltage maximum (kV)
V	Electric potential (kV)
$\vec{W}_{\mathrm{e}}$	Electron Drift Velocity (m s^{-1})
$\vec{W}_{\mathrm{n}}$	Negative Ion Drift Velocity (m s^{-1})
$\vec{W}_{\mathrm{p}}$	Positive Ion Drift Velocity (m s^{-1})
$\vec{x}$	Spatial coordinates
$\vec{x}_{\partial G}$	Spatial coordinates at the boundary of region G
$\vec{x}_{\mathrm{gen}\,i}$	Spatial coordinates of the ith generation point
$\vec{x}_{\mathrm{inc}\,i}$	Spatial coordinates of the ith inception point
x, y, z	Cartesian coordinates
α	Ionisation coefficient (m^{-1})
α_{PD}	Maximum surface charge density in a charge spot (nC mm^{-2})
β	Recombination coefficient ($\mathrm{m}^3\ \mathrm{s}^{-1}$)
χ_{s}	Fraction of traps which are shallow
η	Attachment coefficient (m^{-1})
η_{d}	Angular gradient of void surface at deformation boundary
η_{PD}	Spatial decay constant of surface charge density at charge spot boundary (mm^{-1})
γ	Ionisation parameter of air
κ_s	Surface Conductivity (S)
λ_{d}	Angular spread of deformation
λ_{PD}	Charge Spot Length Scale (mm)
ω	AC Cycle Angular Frequency (s^{-1})
Φ	Workfunction (eV)
ϕ	Polar angle
ρ	Volume charge density (nC mm^{-3})
σ	Surface charge density (nC mm^{-2})
$\Delta\sigma_{\mathrm{gen}\,i\,\mathrm{PD}\,j}$	Change in surface charge density at generation point i due to the jth discharge (nC mm^{-2})

σ_{m}	Material conductivity (S m^{-1})
$\sigma_{\mathrm{PD}\,i}$	Surface charge density deployed by the ith discharge (nC mm^{-2})
$\tau_{\mathrm{dt\ d}}$	Time decay constant of detrappable charge population in deep traps (s)
$\tau_{\mathrm{dt\ s}}$	Time decay constant of detrappable charge population in shallow traps (s)
τ_{PSA}	PSA time delay
τ_{σ}	Time decay constant of surface charge density (s)
Θ	Central angle
θ	Azimuthal angle
θ_E	Azimuthal angle of the electric field
ε_r	Relative permittivity
$\varepsilon_{r\ \mathrm{e}}$	Relative permittivity of epoxy resin
$\varepsilon_{r\ \mathrm{o}}$	Relative permittivity of oil
$\varepsilon_{r\ \mathrm{p}}$	Relative permittivity of Crêpe paper
$\varepsilon_{r\ \mathrm{v}}$	Relative permittivity of the void
φ_{PD}	PD phase angle

AC	Alternating current
DBSCAN	Density based spatial clustering of applications with noise
DC	Direct current
LDPE	Low Density Polyethylene
PD	Partial discharge
PILC	Paper insulated lead covered
PSA	Pulse sequence analysis
SPMD	Swarming pulsive micro discharge

Chapter 1

Introduction

The electric power network is one of the most vital and complex pieces of infrastructure in the modern world. In [1] Hughes argues that electric power networks are "the greatest construction project of the last century." Electric systems operators must therefore maintain network health while simultaneously minimising running costs from the high expenditure of replacing high voltage equipment. This motivates the use of techniques that can quantify component health to ultimately predict the remaining lifetime of high voltage plant. Severe defects in insulation systems are common case of failure in electrical equipment. These defects often have a lower electrical breakdown strength than the surrounding insulation material, which means that discharges can occur inside them. If the discharge does not bridge the gap between electrodes, it is defined as a partial discharge (PD) [2]. Measurements of PD activity are a non-invasive tool that can be used to quantify defect severity prior to failure [3]. Despite sustained research interest, much remains unknown; from the underlying discharge physics to the precise interpretation of phase resolved partial discharge (PRPD) patterns. In conjunction with experiments, modelling PD activity has also received attention to investigate whether complex PD data can be described by a simple system of equations, with the aim of using simulations to gain insight into the PD system. The research conducted in this thesis is intended to contribute to the literature on PD activity modelling.

1.1 Aims

The original aims of thesis were as follows:

1. Critically analyse the existing models of PD activity in the literature and identify shortcomings.
2. Develop an improved model of PD activity that seeks to build upon the shortcomings of earlier work and is more physically accurate.

3. Use this improved model to simulate discharge activity in PD systems which are more indicative of 'real world' conditions that have not previously been investigated.

4. Investigate PD activity from hypothetical scenarios, which cannot be investigated experimentally, to see what insight can be reasonably obtained from simulation.

Over the course of the thesis it became clear that PD activity models in their current form require improvements, so an additional aim of the thesis became:

1. To assess the accuracy of the concept and simplifications used when describing discharge dynamics in PD activity models.

1.2 Contributions

Based on the literature review a PD model was developed. The three key improvements of the model over earlier work in the literature were as follows:

1. Inception and Generation Points - The model considers the inception of a discharge and the electron generation processes governing PD activity at a range of locations in the PD system. Previous models assumed that these processes were governed by the electric field at a single location in the system. This is thought to be more physically descriptive of the system.

2. Two Electron Trap Depths - The detrappable electron population is split between two trap depths. This is different to other approaches in the PD modelling literature, which are not based on experimental evidence, whereas the existence two electron trap depths, while not investigated in PD systems, has been shown to exist as an effective method of modelling charge detrapping.

3. Surface Charge Density Distributions - Surface charge density distributions, due to discharge activity, in an earlier Poisson PD model were discrete, [4], which leads to discontinuities in the electric field at the surface. In this work the distributions were continuous, using logistic functions, which avoids discontinuities and is in approximate agreement with measurements of surface charge density from discharge activity in the literature [5, 6, 7].

Furthermore, when using the model care was taken to minimize the number of free parameters so that there could be increased certainty that the model was representative of the PD system and not simply "curve fitting" the experimental data.

This model was then validated by simulating PD activity from a spherical void in epoxy resin, an experimental arrangement that has been widely investigated in the literature

[4, 8, 9, 10]. The model was able to accurately reproduce the experimental discharge patterns, while using significantly fewer free parameters than earlier work [4]. The hypothetical scenario of discharge activity in deformed voids was then investigated. It was shown that small changes in void geometry can produce significant changes in discharge frequency and PRPD patterns [11]. The model was then used to explore the evolution of discharge patterns due to sustained discharge activity [12]. The investigation allowed some tentative conclusions to be drawn on the changes in the physical conditions in the void due to discharge activity.

Extending the scope of the work, the model was then used to model PD activity from a three phase cable experiment [13]. This is a significant departure from the standard systems investigated by PD models in the literature, and required a fully three dimensional model. Using physical reasoning and some intuitive assumptions, the model was capable of estimating the scale of the defect in the experiment. Further investigations using the model showed that PD activity can be affected by small changes to the applied voltage waveform, and is highly sensitive to phase energisation of the cable. The hypothetical scenario of discharge activity from a spherical void at various locations in the paper surrounding one of the phase conductors was then investigated [14]. This scenario showed the elliptical applied field of three phase cable joints can have a significant impact on PD activity. Furthermore, the results highlighted the dependency of the apparent charge of a discharge on the direction of the discharge with respect to the measuring electrode.

From working with the model the current limitations of PD activity models became fairly apparent, namely the simplistic description of discharge dynamics and the dependence on unmeasurable free parameters. To test the concepts and assumptions used in PD activity models a drift diffusion model of plasma dynamics was developed, and used to simulate PD in a spherical air filled void [15, 16]. The results of the simulation showed noticeable disagreement with much of the canonical reasoning in the literature [17]. In particular, the electric field is reduced to values far below the "residual field" that is commonly assumed. It also appears that the surface charge distributions from discharges are significantly more complex than those currently assumed by PD activity models. The fundamental contribution of this work is therefore that, in their current form, PD activity models are not entirely fit for purpose. Ultimately, to properly model PD activity it is important to have a good description of the electron generation processes, that provide the initial seed charge for PD, and to date this has yet to be fully understood.

1.3 Contents

The work is divided into chapters as follows:

1. Chapter 1 - A brief introduction, outlining the research conducted for the project.

2. Chapter 2 - An analysis of the literature is undertaken, comprising an introduction to PD phenomena, a critique of existing PD models and an overview of PD data analysis.

3. Chapter 3 - A general PD model is developed that improves on previous work by considering electron generation and PD inception processes at multiple locations in a defect, rather than at a single point. It also introduces the concept of splitting the detrappable charge population between "deep" and "shallow" traps.

4. Chapter 4 - The PD model is validated against experimental data of PD activity in a spherical void in epoxy resin. Following this the model is used to investigate the potential impact of void deformation on PD activity.

5. Chapter 5 - In order to extend the scope of the model, PD activity from three phase cable experiments is then investigated. It was found that PD activity from an experiment where a spike was fabricated on one the ferrules of the phase conductors could be simulated using the model. However, a number of other experiments produced PD data that was too noisy and complex to investigate using the model without making a large number of unjustifiable assumptions. The potential impact of the elliptical applied field, present in three phase cable, on PD activity was then investigated.

6. Chapter 6 - Based on the shortcomings identified in PD activity models over the course of this work, a drift diffusion plasma model was developed to test whether some of the assumptions and simplifications were truly justified. The results showed that a rethink of PD activity models may be required in the future.

7. Chapter 7 - The conclusions of the work are presented, and future projects that could be developed from this work discussed.

For clarity a new style of notation for the governing equations in the PD activity model is developed and used for all equations presented in Chapters 2 to 5. The style is explained in Appendix A. This notation is not used in Chapter 6 as a fundamentally different model is introduced, the notation in that chapter follows the standard approach in the literature, as an example the reader is referred to [7]. The work conducted in this thesis is intended to contribute to the literature on the subject of modelling PD activity in gaseous voids. This subject area has already received research attention, an analysis is undertaken in the next chapter.

Chapter 2

A Review of Partial Discharge Modelling

In this chapter an introduction to partial discharge (PD) phenomena and its modelling are presented. As the aim of this research is to develop an improved PD activity model, existing models will be investigated to gain insight into current methods and to inform the research performed in this report. Common methods of interpreting PD data are discussed, and the issues present in analysing field data are introduced. The chapter concludes with the motivation for modelling PD in high voltage plant, and the possible improvements that can be made based on the previously reported work in the literature.

2.1 Introduction

Van Brunt defines a PD as "a highly localised or confined electrical discharge within an insulating medium between two conductors" [2]. In high voltage plant the electric breakdown strength of insulating materials is very high, so PDs typically occur within insulation defects, such as gaseous voids, where the electric breakdown strength is far lower. By relating PD activity to defect properties PD measurements can be used to quantify insulation health. It should be noted that due to the broad definition of PD a large variety of discharges are categorised as PD, which has led to classification issues [18]. The focus in this work is on PDs in gaseous voids, and henceforth the discussion will be restricted to these cases.

Standard reasoning states that for a PD, or indeed any discharge, to occur in a void two conditions must be met:

1. Inception Condition - A sufficiently high electric field in the void that exceeds the PD inception field, E_{inc}.

2. Free Electron Condition - A free electron is available in the void to begin ionisation.

The free electron is accelerated by the electric field sufficiently to cause the ionisation of atoms and molecules within the defect generating further electrons which initiate electron avalanches that propagate the discharge [19]. In the case of PD in voids that are bounded by dielectric material, the charge deployed by the discharge at the dielectric boundary itself will oppose the electric field that initiated it, eventually stopping the discharge.

There are many different physical mechanisms that generate electron avalanches to propagate discharges; in [20] Morshuis classifies them into two main groups of interest: Townsend-like mechanisms and streamer-like mechanisms. In Townsend-like discharges an electron avalanche is sustained by the successive ionisation of atoms to create new electrons in a chain reaction; the ionising electrons for this process can be generated by cathode emission [21]. Due to the higher mobility of electrons compared to ions, electrons will congregate in an area known as the avalanche head, ions are more disperse to due their lower mobility, and in a region behind the avalanche head, known as the avalanche tail. Due to the polarity of the charges, the avalanche tail will move in the direction of the electric field and the avalanche head will move in the opposite direction. Townsend-like discharges cannot give rise to self-sustaining discharges without external electron generation. However, at higher electric fields streamer-like discharges can occur, which have a different physical mechanism and are self sustaining [22, 23]. In streamer-like discharges, the electric field between the avalanche head and avalanche tail is sufficiently high to oppose the external field. This results in a region of positive and negative charge, between the avalanche head and tail, in a low electric field leading to a high level of recombination, producing photons. These photons ionise atoms at other locations in the gas, generating successive electron avalanches. These avalanches form a self sustaining ionising wave which can propagate across the void [24]. Due to the greater number of charged particles and the higher electric fields involved streamer-like discharges create significantly higher currents (10 mA - 1000 mA) than Townsend-like discharges (10^{-3} mA - 1 mA) at the standard conditions present during PD activity [25].

For most practical PD systems streamer discharges, the namesake of the streamer-like group, are of greatest interest [9]. The reason for this is that they are detectable, significantly damage insulation material and are a common precursor to more intense discharge types [17]. It should be noted that multiple discharge types can occur simultaneously, and Townsend-like avalanches are common in pre-streamer conditions [26]. The time scale for these discharges is typically in the order of nanoseconds [27].

The charge deployed by PD results in a change in charge, and therefore current, on the surface of all electrodes in the system, this can be measured by sensors, attached to a measuring electrodes, which are connected to digital oscilloscopes [20]. Clearly the magnitude of the induced current and charge, which are referred to as the apparent current and charge, will be dependent on the location of the defect relative to the measuring

electrode. For most experimental PD systems, the apparent charge is in the order of 100's of pC [4, 9].

The apparent current is also commonly referred to as the PD signal or PD pulse and measurement systems typically need to have bandwidths of at least the order of MHz to accurately detect it [28]. Due to the impedance of the PD system, dispersion, attenuation and reflection of the signal can occur, which can alter the characteristics of the PD signal [29]. Noise from PD signals can be reduced using various methods including the wavelet transform [30], and analysis of the pulses can be used to cluster PDs into distinct groups [3]. Typically the main features used to classify PDs in AC equipment are the apparent charge q'_{PD}, also referred to as magnitude, and the angle of occurrence in the AC cycle, known as the phase angle φ_{PD}. The apparent charge q'_{PD} is distinct from the physical charge, q_{PD}, deployed by the PD.

For PDs in gaseous voids discharge activity can be affected defect size, shape, temperature, gas pressure, surface chemistry and electrical stress [31, 32]. The overall aim of this research is to develop new models for PD behaviour that allow insight into the more complex PD activity measured from high voltage plant in the field.

2.2 Partial Discharge Models

In this section physical models of PD behaviour in the literature are analysed. All of the models discussed in this section have been used to model PD from voids surrounded by solid material, their use in other systems will not be discussed, because it is not relevant to the current work. The discharges occurring inside voids, for the electric field magnitudes present, in these systems are typically assumed to be streamers [17]. However, in the majority of these models the specific physics of streamer discharges are not considered in the models due to the computational cost of simulating the physical processes. PDs are simply classified by phase angle and magnitude and the models try to reproduce these values. Due to the timescales of an AC cycle compared to a discharge event, these models typically treat discharges as instantaneous processes. The first attempts to model PD activity used ABC or "Three Capacitance" models [33, 34, 35, 36]. However, as ABC models have been largely discredited, [19, 37, 38], and have received little attention since the early 1990's they will not form part of this review. It should be noted that the vast majority of PD behaviour models to date have been used to replicate measurements in parallel plate systems.

2.2.1 Niemeyer's Model

Niemeyer's work can be considered the foundation for the majority of the current literature on PD modelling. In this model the two conditions for a discharge to occur are

considered at each time step in a computer simulation. The electric field within the void is considered to be uniform, and the apparent charge from the PD is calculated from equations derived in the earlier theoretical work of Crichton *et al.* [39].

The inception condition, whether the field is sufficiently high for PD to occur, is treated as deterministic, with the magnitude of the electric field in the void compared to an inception value at each time step. The inception field is dependent on the length of the void in the direction of the discharge and the gas pressure. For air the inception field formula and is taken from the work of McAllister *et al.* [40]. It should be noted that this inception field equation is derived based on breakdown measurements between metallic parallel plate electrodes, [41], and as such its applicability to air voids surrounded by dielectric material may be questionable. After a discharge has taken place it is assumed that the electric field is reduced to a residual value E_{res}, which for air is dependent on the pressure. E_{res} is set to be equal to the field in the discharge channel of the streamer [9]. The justification for this is not entirely clear, and it would seem reasonable to suppose that the field after the discharge would be affected by recombination of charge in the gas, as well as the surface charge at dielectric boundaries. Furthermore, the field in the discharge channel appears to be determined from streamers between metallic electrodes in a needle-plane system [42], which may not be representative of conditions in many PD systems.

The free electron condition, that is if a free electron is available that could start the ionisation process, is considered to be a stochastic process. At each time step a probability, dependent on the electron generation rate $\dot{N}_{\mathrm{e}}$ is compared to a random number uniformly distributed between 0 and 1. If the probability exceeds this number, the free electron condition is met. $\dot{N}_{\mathrm{e}}$ itself is a sum of the electron generation rate from surface emission, $\dot{N}_{\mathrm{e\,s}}$, and the electron generation rate in the void volume from background radiation, $\dot{N}_{\mathrm{e\,v}}$. There are other possible physical mechanisms for electron generation, but these are assumed to be negligible at the physical conditions present in the PD systems under consideration. For voids surrounded by dielectric surfaces, surface emission occurs when the charge deposited by previous PDs is emitted back into the void. As this process is clearly only active after the first PD has occurred for PD in voids surrounded by dielectric material the free electron for the first PD, in the absence of other external sources such as X-rays, is assumed to be generated in the void volume due to background radiation [17]. The long inception delay that is often observed before the first PD suggests that the rate of background radiation is very low, and such the dominant mechanism to produce free electrons for discharges is surface emission. In [17] an equation, which has subsequently been widely used, governing the electron generation rate from surface emission, $\dot{N}_{\mathrm{e\,s}}$, for insulator surfaces is introduced,

$$\dot{N}_{\mathrm{e\,s}}(E_{\mathrm{v}}, N_{\mathrm{dt}}; T, \Phi) = \nu_0 N_{\mathrm{dt}} \exp\left(\frac{1}{k_{\mathrm{B}} T}\left[\sqrt{\frac{e^3\,|E_{\mathrm{v}}|}{4\pi\varepsilon_0}} - \Phi\right]\right) \tag{2.1}$$

where ν_0 is the fundamental phonon frequency, N_{dt} is the number of electrons in detrappable traps at the surface, E_{v} the electric field inside the void, Φ an effective work function and T is the temperature. Niemeyer assumes that immediately after a discharge N_{dt} is equal to the total number of electrons deployed into the dielectric surface by that discharge, and between discharges it obeys an exponential decay. It should be noted that there is no physical evidence for these assumptions, and there is still a limited understanding of the electron generation rate from trapped charge in insulators. Furthermore, model results are highly dependent on both Φ and the time constant governing the decay of N_{dt}, both of which are treated as free parameters that are adjusted such that the model is in agreement with experimental data. A thorough literature investigation has also revealed that there are some inconsistencies with this equation. Firstly, in the original work, [10], the Schottky term is not included. More significantly, it appears (2.1) is developed from an equation proposed in earlier work to explain the electron generation rate from surface charge deposited by discharges between concentric glass tubes in a vacuum [43]. However, the Schottky term in this earlier work has a magnitude twice as large. This is because the potential of the electron in Schottky term is based on the method of images at a metallic boundary, whereas at a dielectric boundary the potential energy is between an electron and a hole [43]. It is not thought that this effect will significantly influence any of the previous results which have used (2.1), but it should be noted that based on a literature study it does appear to be erroneous. If surface emission from metallic surfaces is considered, Niemeyer proposes that the numerous surface emission processes that are possible, including ion impact, obey Richardson-Schottky thermionic emission law scaling [17]. This seems highly incorrect as thermionic emission itself will be insignificant at the temperatures present in most PD systems of interest, and it is not clear what evidence there is that fundamentally different physical processes will obey the same scaling.

The model is completed with an equation for the decay of the local field due to movement and eventual recombination of surface charge along the dielectric surface. The original model then has 3 free parameters if surface conductivity is neglected: the work function Φ, the time decay constant for the decay of N_{dt} and the pressure which is used to calculate E_{res} and E_{inc}. These free parameters are then adjusted to fit experimental data. Simulations using the model were able to give approximate agreement for PRPD patterns for spherical voids in epoxy resin under a variety of conditions [10]. In [17], it is argued that the model can be applied to a variety of different gaseous defects surrounded by solid boundaries, with a look up table for 15 different defect configurations provided. However, the model is only applied to a spherical air filled void in epoxy and an electrode protrusion in SF_6. In [9] the model was used to investigate the changes in PRPD patterns due to discharge activity from a spherical void in epoxy resin over extended periods of time. To accurately reproduce the standard "rabbit ear" discharge patterns observed in the experiment, a scaling factor was introduced to (2.1), and it was argued that it is harder to emit charge from negatively surfaces compared to positively charged surfaces,

adding a parameter to the model. This assumption has subsequently been used in future work, [4, 8, 44], however there is no empirical evidence to support it. Furthermore, there are alternative assumptions that can give rise to the observed PRPD patterns. These include introducing a variation in the effective work function of the surface, that adds two free parameters, which was used to describe PRPD patterns from discharge activity in epoxy resin for a range of applied voltage frequencies [45, 46].

In conclusion, Niemeyer's model has been successful at replicating a range of PD experiments in gaseous voids. However, there are inconsistencies in some of the governing equations, and it is not entirely clear whether many of the fundamental assumptions are justified. Furthermore, the model is heavily dependent on unmeasurable free parameters, which have to be adjusted significantly to fit different experimental data sets.

2.2.2 Finite Element Analysis PD Models

Advances in computational power have allowed finite element analysis (FEA) software to be used to model PD activity. Two of the main authors in this field are Cecilia Forssen from KTH Royal Institute of Technology and Hazlee Illias from University of Malaysia, formerly University of Southampton. In these models, an equation for the electric field is solved numerically on the PD geometry, voids do not need to be described as equivalent ellipsoids. Generally the governing equation for the electric field has been

$$\vec{\nabla} \cdot \left(\sigma_{\mathrm{m}}(\vec{x},t)\vec{\nabla}V(\vec{x},t) + \varepsilon_0\varepsilon_r(\vec{x})\frac{\partial}{\partial t}(\vec{\nabla}V(\vec{x},t)) \right) = 0, \tag{2.2}$$

where σ_{m} is the conductivity of material, ε_r is the relative permittivity of the material and V is the electric potential [8, 44]. More recently, FEA models have been developed that use the standard electrostatic Poisson equation,

$$\nabla^2 V(\vec{x},t) + \frac{\rho(\vec{x},t)}{\varepsilon_0\varepsilon_r(\vec{x})} = 0, \tag{2.3}$$

where ρ is the volume charge density [4, 47, 48]. For both (2.2) and (2.3), the boundary conditions used for V match the experimental conditions, and the electric field $\vec{E}$ can be determined through

$$\vec{E}(\vec{x},t) = -\vec{\nabla}V(\vec{x},t). \tag{2.4}$$

In the following discussion models that use (2.2) as the governing equation will be referred to as conducting models, models that use (2.3) will be referred to as Poisson models.

Conducting models model a discharge as altering the conductivity of the void to reduce the electric field in the centre of the void to the residual value E_{res}. This approach leads to an approximately uniform electric field in the void, which in line with Niemeyer's assumption. In Poisson models the surface charge density at the void surface is altered during PD to reduce the electric field in the centre of the void toE_{res}. This leads to an

inhomogeneous electric field inside the void, but these models still assume that electron emission and PD inception are controlled by the electric field at a single point in the void, typically the centre. These models have frequently used a discrete distribution for the surface charge density, this leads to an infinite electric field at the boundary of the surface charge distribution, which is clearly unphysical. Another point of clarity is that the residual field E_{res} has often been described as the extinction field E_{ext}. This is somewhat misleading, as the extinction voltage has a clear meaning in the IEC standard, as the applied voltage at which repetitive PD activity stops [49]. It is not clear that the electric field associated with this voltage can be associated with the residual field.

Instead of (2.1) most FEA models use an alternative electron generation equation for surface emission that does not have a work function and has a different dependency on the electric field [44]. This equation is used because it is easier to fit the parameters to experimental data, it is not based on experimental measurements. The concept of a detrappable electron population is still used. FEA models have also used unphysical values for electron generation from volume ionisation in order to fit experimental data, with values 3 orders of magnitude higher than physical estimates in [10].

An advantage offered by FEA models is that the apparent charge from PDs can be calculated directly, rather than relying on approximate equations in [39]. For models with (2.2) as the governing equation, a time integral of the current is performed. Models that use (2.3) integrate the change in surface charge density. In both cases the integral is performed over the measuring electrode, typically the ground electrode in a parallel plate system. Surface conductivity can also be considered more explicitly, either by altering the conductivity of the void in conducting models, or solving a surface charge density continuity equation, [50, 51], in Poisson models [4].

FEA PD models have been applied to analyse PD behaviour from a variety of systems. These include the variation of PD activity in spherical void and cylindrical voids under AC conditions with temperature, applied field amplitude and applied field frequency, [4, 8, 44, 52]. Recently PDs due to impulse voltages in a cylindrical void, and PDs from an artificial defect in a system approximating a high voltage cable have also been considered [47, 48]. FEA models represent a major improvement over Niemeyer's model for two main reasons. Firstly, the electric field is calculated throughout the PD system at each time step, greatly increasing physical accuracy. Secondly, explicitly modelling the surface charge density, or conductivity, allows real and apparent charges to be calculated directly, rather than through equations based on approximations of the PD system geometry [39]. The simulations have shown very good agreement with experimental data, in terms of both PDs per cycle and maximum PD amplitude. The models suffers from a large number of curve fitting parameters, approximately 6, and a simplified description of electron generation. Poisson models appear to be more representative of the discharge process as opposed to a conducting models, because recombination of charge in the gas is likely to be a fairly rapid process and it seems likely that the description of PDs

by altering the surface charge density at the void surface is therefore more physically accurate.

2.2.3 Plasma PD Models

PD models are typically interested in reproducing experimental measurements for a large number PDs. As such, the discharge process is heavily simplified, as has been shown in the previous sections. A more rigorous approach is to use models that explicitly consider the plasma dynamics of the discharge. A well established approach is to use drift diffusion equations that describe the dynamics of electrons, and "abstract" positive and negative ions [24]. A large number of these simulations have been used in the literature, typically to model discharges from a needle-plane electrode configuration with no solid dielectric materials present [53, 54]. Investigations have also been made into dielectric barrier discharges [55, 56]. These simulations have often been used to provide insight into systems where discharge activity is desired, such as sterilisation, or material processing [24]. This means that the majority of these investigations offer limited insight into PD activity for systems of interest as they are conducted under significantly different physical conditions. Most notably discharges often take place applied voltage frequencies in the order of kHz, whereas PD systems of interest are typically at power frequencies of 50-60 Hz.

However, there are some models of PD using plasma models in the literature. Serdyuk *et al.* showed that a single discharge in an air gap between electrodes covered in polyethylene consisted of an electron avalanche transitioning into a positive streamer [57]. Earlier work had shown similar results for a discharge in air where only one electrode was covered in a dielectric material [58]. Testa *et al.* presented a one dimensional model for single PDs that considered the transport of electrons, positive ions and electron energies for air gaps in polymers [59]. Models that consider multiple PDs have also been developed. In [60] drift diffusion equations were used to model a large number of PD in an air gap bounded by an electrode above and an electrode covered with a dielectric material below. Unfortunately, the numerical techniques used in this work, by necessity to reduce the computational cost, mean that its results must be approached with some caution. Recently a more rigorous model was successful at modelling several discharges in a spherical air void [61]. It should be noted that the emphasis of this work was in the development of numerical techniques to solve the governing equations, the analysis of the results at is pertains to PD activity is somewhat limited. Furthermore, despite axisymmetric physics and geometry, the presented results, solved in a three dimensional geometry, display a high level of asymmetry, the reasons for which are unclear.

2.3 Partial Discharge Data Analysis

Analysing PD data is a non-trivial activity and there are many statistical measures and graphical representations that can be used for this task. In this section a brief overview of statistical measures that have been used and two of the more common representations of PD data, pulse sequence analysis (PSA) plots and phase-magnitude discharge patterns, are discussed [62].

Common statistical measurements of PD data include arithmetic mean, skewness and kurtosis of PD pulses [30]. The distribution of phase angle is similarly investigated. In addition to these common measures, chaotic measures have been used to classify PD data. These include fractal dimensions [63, 64] and measures of complexity [3], which have been shown to reveal additional structure in PD data. These statistical measures have been used in neural networks to identified features to distinguish PD patterns in different experiments [30, 65]. Weibull distributions have also been applied to investigate PD data. Apparent charge magnitudes from certain PD sources have been shown to be well described by Weibull distributions [66]. Weibull distributions have also been employed to make lifetime estimates of high voltage plant based on PD measurements [67, 68].

In addition to analysing PD data quantitatively through statistics, qualitative information can be gained through appropriate graphical representations. The two most widely used graphical representations are scatter plots of φ_{PD} and q'_{PD}, known as phase resolved partial discharge (PRPD) plots and two dimensional histograms of φ_{PD} and q'_{PD}, known as φ-q-n plots. φ-q-n plots have been used to determine physical parameters [69] and classify distinct PD sources [62]. Examples of PRPD and φ-q-n plots are shown in Figures 2.1 and 2.2 respectively for the same data set.

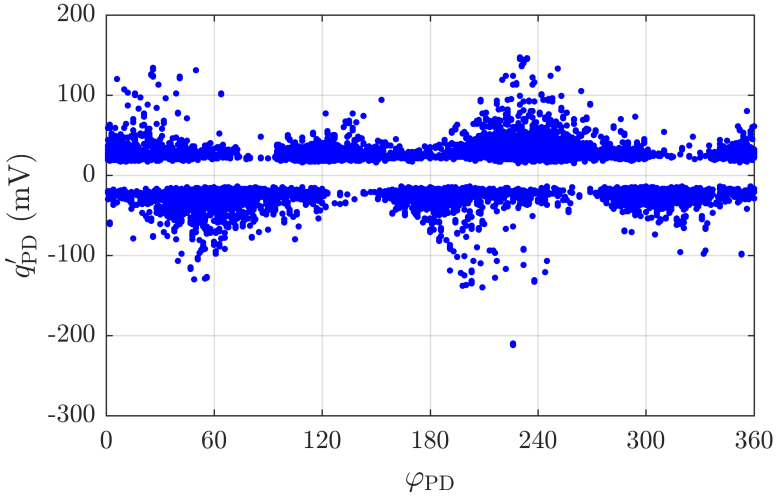

FIGURE 2.1: Figure showing PRPD plot of PD data taken from three-phase paper insulated lead covered (PILC) cable in Glaucus Road (London).

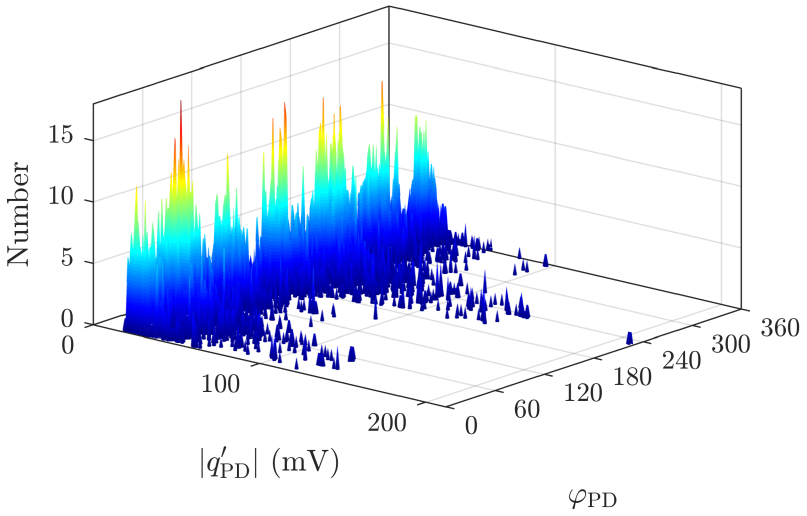

FIGURE 2.2: Figure showing φ-q-n plot with 200×200 bins of PD data taken from three-phase PILC cable in Glaucus Road (London).

Despite their usefulness, PRPD and φ-q-n plots convey no information on any potential relationships between consecutive discharges, to investigate this PSA plots are used. PSA is performed by taking a vector of realisations of a time dependent variable and constructing a delay reconstruction vectors from it. The size of the delay construction vector, m_{PSA}, and the time delay used, τ_{PSA}, are specified by the user. An example of such a PSA plot with $m_{\mathrm{PSA}} = 2, \tau_{\mathrm{PSA}} = 1$ is shown in Figure 2.3 using the same data as Figures 2.1 and 2.2. PSA plots can be used to investigate strange attractors within a PD system by employing Takens' theorem and finding appropriate values of m_{PSA} and τ_{PSA} [64].

Research attention has also been focused on discriminating individual sources from PD data. In this work it is assumed that the current pulse from each PD source will be unique. Pulses are decomposed using a variety of techniques, including time frequency mapping, normalised auto-correlation functions and discrete wavelet decomposition [70, 71, 72]. Each pulse is represented as an N dimensional position vector in a feature space. A clustering algorithm is then used to identify clusters in this space, discriminating sources of PD. One of the most common clustering algorithms used for this is "density based spatial clustering with noise" (DBSCAN), [73], which requires dimensional reduction to be performed on feature space before clustering can take place [22, 72]. However, it is not the only clustering algorithm available and the choice of decomposition and clustering algorithms for PD source discrimination is still a topic of current research [74, 75].

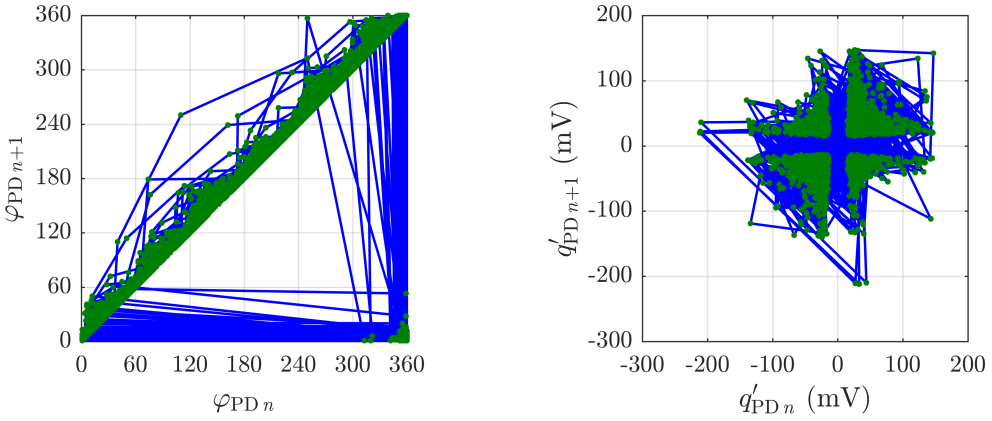

(a) (b)

FIGURE 2.3: Figure showing PSA ($m_{\mathrm{PSA}} = 2, \tau_{\mathrm{PSA}} = 1$) plots of (a) phase angle (φ_{PD}) and (b) apparent charge (q'_{PD}) of PD data taken from three-phase PILC cable in Glaucus Road (London).

2.4 Conclusion

This chapter has provided an introduction to PD and a summary of the PD modelling literature to date. A range of PD models have been developed, fundamentally many of the concepts can be traced back to the foundational work of Niemeyer. PD models have been successful at reproducing PRPD patterns for a variety of experiments, typically cylindrical or spherical air filled voids surrounded by a solid dielectric material, often polyethylene or epoxy resin. Despite this success, there are numerous shortcomings, and in some cases inconsistencies, in many of the PD models used in the literature which have been outlined in this review. The purpose of this work will be to develop an improved model of PD in gaseous voids.

By consideration of the literature review, it is proposed that a Poisson PD model is developed, and solved using FEA. A Poisson model is preferred over Niemeyer's model, or an ABC model, as it allows the defect geometry to be fully resolved, and allows explicit calculation of the apparent charge and provides knowledge of the electric field at all locations in the PD system. A Poisson model is proposed instead of a conducting model, because recombination of charge in the gas is likely to be a fairly rapid process and it seems likely that the description of PDs by altering the surface charge density at the void surface is more physically accurate. The model will attempt to address the shortcomings of previous FEA Poisson models, especially the dependence on high number of free parameters. Many previous models have used a relatively high number of free parameters, and it is argued that this provides a more physical description of the PD process and allows the model results to fit experimental data. An issue with this

is that the model increasingly becomes an exercise in curve fitting, and loses physical relevance. It is not possible to remove free parameters completely, due to the limited information available from the PD system, but an effort will be made in this research to minimise their number. It should be noted that as the description of the discharge process is still a significant simplification in this model, and it will not be possible to remove many of the shortcomings associated with previous PD models. Once validated, the model will be used to investigate PD activity from three-phase cable experiments [76]. This is because they provide a middle ground between the controlled experiments that have been widely investigated using PD models and the complex PD data sets taken from field measurements.

Over the course of the research conducted in this work it became clear that the shortcomings of the improved PD model are still significant. In particular it is not clear whether many of the concepts used in the model are justified. As a result of this a drift diffusion plasma model of PD was developed, with the aim of testing these concepts. This work forms the fundamental contribution of the thesis, which is that a significant rethink of PD modelling is required, especially if the more complex PD systems present in the field are going to be considered.

Chapter 3

General Model for Partial Discharge in Voids

In this chapter a general PD model for discharges in a gaseous void bounded by solid material is introduced. From the literature survey performed in Chapter 2, a FEA Poisson model of PD is used. The discharge process is simulated by changing the surface charge density at the void boundary, the distributions and values of which can be checked, approximately, against experimental measurements [5, 6, 77]. Certain equations used in this model have been previously introduced in the literature review, Chapter 2, however to make this chapter self contained all equations used in the model will be given. Due to the computational cost, surface conductivity is not modelled using FEA, the justification is given in Section 3.3.

3.1 Electric Field

The electrostatic potential V is found by numerically solving the electrostatic Poisson equation over the PD system geometry,

$$\nabla^2 V(\vec{x},t) + \frac{\rho(\vec{x},t)}{\varepsilon_0 \varepsilon_r(\vec{x})} = 0, \tag{3.1}$$

where $\vec{x}$ is a spatial coordinate, t is time, ρ is the volume charge density. The electric field $\vec{E}$ is then found by calculating

$$\vec{E}(\vec{x},t) = -\vec{\nabla} V(\vec{x},t). \tag{3.2}$$

The interior boundary conditions of the model are as follows

$$(E_1(\vec{x}_{\partial G_1 \cap \partial G_2}, t) - E_2(\vec{x}_{\partial G_1 \cap \partial G_2}, t)) \cdot \vec{e}_{\parallel}(\vec{x}_{\partial G_1 \cap \partial G_2}) = 0 \quad (3.3)$$

$$(D_1(\vec{x}_{\partial G_1 \cap \partial G_2}, t) - D_2(\vec{x}_{\partial G_1 \cap \partial G_2}, t)) \cdot \vec{n}_{12}(\vec{x}_{\partial G_1 \cap \partial G_2}) = \sigma(\vec{x}_{\partial G_1 \cap \partial G_2}, t), \quad (3.4)$$

where the 1 and 2 subscripts denote values in the regions G_1 and G_2 respectively, $\partial G_1 \cap \partial G_2$ is the boundary between the regions, $\vec{x}_{\partial G_1 \cap \partial G_2}$ are spatial coordinates at the boundary, $\vec{D}(\vec{x}, t) = \varepsilon_0 \varepsilon_r(\vec{x}) \vec{E}(\vec{x}, t)$ is the electric displacement field, $\vec{n}_{12}$ is a unit vector normal to the boundary pointing from G_1 to G_2, $\vec{e}_{\parallel}$ is any unit vector tangential to the boundary and σ is the surface charge density. (3.3) and (3.4) are the standard boundary conditions at boundaries between materials of different permittivity in electrostatics [78]. The exterior boundaries of the PD system will either have Dirichlet conditions where V is set based on the applied voltage conditions in the PD system, or the following Neumann condition for V,

$$\vec{E}(\vec{x}_{\partial G}, t) \cdot \vec{n}(\vec{x}_{\partial G}) = 0, \quad (3.5)$$

where ∂G is an exterior boundary of the region G, $\vec{x}_{\partial G}$ are spatial coordinates at the boundary and $\vec{n}$ is a vector normal to the boundary. Throughout this work it will be assumed that metallic domains are at a constant voltage at any given time and are therefore not included in the model geometry.

In the systems considered by the model, it will be assumed that charge is not present in the bulk of the material. Charge is only present at the boundary of the void where it is deposited by discharges. ρ can therefore be written as

$$\rho(\vec{x}, t) = \delta(\varsigma) \sigma(\vec{x}_{\partial G_{\mathrm{v}}}, t), \quad (3.6)$$

where δ is the Dirac delta function, ς is a spatial coordinate which is zero at the void boundary and non-zero everywhere else, σ is the surface charge density, G_{v} is the void region and $\vec{x}_{\partial G_{\mathrm{v}}}$ are spatial coordinates at the void boundary ∂G_v. The Dirac delta function in (3.6) implies that the volume charge density ρ is infinite on the void surface, which makes physical sense as a finite charge is enclosed within an infinitesimal volume.

3.2 Inception and Generation Points

In all PD models to date, the conditions for a discharge are based on the electric field at a single point for each PD source. In this model, inception and generation processes are considered at multiple points, known as inception points and generation points respectively. The location of inception and generation points will depend on the physics and geometry of the PD system. Inception points will be located in regions where the electric field is highest on the discharge paths. In other words for a PD to occur, the

discharge path must at some point have an electric field that exceeds an inception field. Generation points will be located where electron generation processes take place, this will depend on the physical mechanism being considered. To avoid location bias, inception and generation points must be evenly distributed in the regions they span. The number of inception points, N_{inc}, and the number of generation points, N_{gen}, are increased until the results of the model no longer change.

If a discharge occurs at the ith inception point, located at $\vec{x}_{\text{inc}\,i}$, at a time t_{PD} then the electric field must satisfy

$$\left|\vec{E}(\vec{x}_{\text{inc}\,i}, t_{\text{PD}}^{-}) \cdot \vec{e}_{\text{inc}\,i}\right| > E_{\text{inc}}, \tag{3.7}$$

where $\vec{e}_{\text{inc}\,i}$ is a unit vector that defines the direction the discharge is propagating at $\vec{x}_{\text{inc}\,i}$, the $-$ superscript denotes the time immediately before t_{PD} and E_{inc} is the inception field. (3.7) will be referred to as the inception condition. The other necessary condition is that a free electron is available at the ith generation point

$$\dot{N}_{\text{e}}(\vec{x}_{\text{gen}\,i}, t_{\text{PD}}^{-})\Delta t > R, \tag{3.8}$$

where $\dot{N}_{\text{e}}$ is the electron generation rate, Δt is the time step used in the model and R is a random number selected from a uniform distribution between 0 and 1 at each time step. (3.8) will be referred to as the free electron condition and has been widely used in previous models [8, 17, 44, 79].

The discharge will then propagate until the residual condition is met,

$$\left|\vec{E}(\vec{x}_{\text{inc}\,i}, t_{\text{PD}}^{+}) \cdot \vec{e}_{\text{inc}\,i}\right| = E_{\text{res}} \tag{3.9}$$

where the $+$ superscript denotes the time immediately after t_{PD}. For simplicity it will be assumed that the E_{inc} and E_{res} take the same value at all inception points. As the discharge should oppose the field that initiated it, it is required that $E_{\text{inc}} > E_{\text{res}}$.

Depending on the PD system it may occur that inception and generation points coincide, or that for a PD to occur the inception condition must be met at inception point i and the free electron condition met at generation point j. For a PD to occur at given time, both the inception and free electron conditions must be satisfied. It should be noted that there are models in the literature which have considered inception and generation conditions at multiple points in the defect. However, this was designed to capture multiple PD sources, with one inception and generation point per source. The approach introduced here is novel in that for each PD source in the model the inception and generation processes are captured at all the locations in the defect where they occur.

3.3 Surface Charge Dynamics

The surface charge density at the void boundary is initially set to zero. Discharges will change the surface charge density at the defect, such that the extinction condition is met at the inception point that initiated the discharge. In this model discharges are treated as instantaneous events, so that for the ith PD the surface charge density can be written as

$$\sigma(\vec{x}_{\partial G_\mathrm{v}}, t^+_{\mathrm{PD}\,i}) = \sigma(\vec{x}_{\partial G_\mathrm{v}}, t^-_{\mathrm{PD}\,i}) + \sigma_{\mathrm{PD}\,i}(\vec{x}_{\partial G_\mathrm{v}}) \tag{3.10}$$

where $\sigma_{\mathrm{PD}\,i}$ is the surface charge density of the charge deployed by the ith PD. Experimental evidence suggests that the charge distribution from PDs, σ_{PD}, is bipolar, an assumption also used in previous PD models [6, 10], and the distribution charge of deposited by PD will be approximately discrete. However, a discrete charge distribution, which has been used in earlier work [4], is not physically sensible or numerically stable. The distribution of surface charge in σ_{PD} is therefore described by two logistic functions, which are smooth step functions, of equal magnitude and opposite polarity. To describe the logistic functions three values are required: α_{PD} the height of the step, λ_{PD} the spatial spread of the step, and η_{PD} the gradient of the step. It will be assumed that discharges impact the void surface at a two points, $\vec{x}^+_{\partial G_\mathrm{v}\,\mathrm{PD}\,i}$ and $\vec{x}^-_{\partial G_v\,\mathrm{PD}\,i}$, which are the centres of the positive and negative charge spots respectively. The points of impact, $\vec{x}^+_{\partial G_\mathrm{v}\,\mathrm{PD}\,i}$ and $\vec{x}^-_{\partial G_v\,\mathrm{PD}\,i}$, will be assumed to be the intersection of a line in the direction of the electric field that met the inception condition and the void surface. The logistic function is dependent on the distance from the centre of the charge spots over the surface of the defect. The height of the step α_{PD} is adjusted such that the extinction condition is met. The explicit functional form of $\sigma_{\mathrm{PD}\,i}$ is then

$$\begin{aligned}
\sigma_{\mathrm{PD}\,i}(\vec{x}_{\partial G_\mathrm{v}}, \vec{x}^+_{\partial G_\mathrm{v}\,\mathrm{PD}\,i}, \vec{x}^-_{\partial G_\mathrm{v}\,\mathrm{PD}\,i}, \alpha_{\mathrm{PD}\,i}; \lambda_{\mathrm{PD}}, \eta_{\mathrm{PD}}) &= \ldots \\
\underbrace{\frac{\alpha_{\mathrm{PD}\,i}}{1+\exp\left(\eta_{\mathrm{PD}}\left[d_\mathrm{v}\left(\vec{x}_{\partial G_\mathrm{v}}, \vec{x}^+_{\partial G_\mathrm{v}\,\mathrm{PD}\,i}\right) - \lambda_{\mathrm{PD}}\right]\right)}}_{\text{Positive Charge Spot}} &- \ldots \\
\underbrace{\frac{\alpha_{\mathrm{PD}\,i}}{1+\exp\left(\eta_{\mathrm{PD}}\left[d_\mathrm{v}\left(\vec{x}_{\partial G_\mathrm{v}}, \vec{x}^-_{\partial G_\mathrm{v}\,\mathrm{PD}\,i}\right) - \lambda_{\mathrm{PD}}\right]\right)}}_{\text{Negative Charge Spot}}&,
\end{aligned} \tag{3.11}$$

where d_v is a distance function for the distance along a surface between two points on the void surface. The logistic function approximates "saddle" distributions of charge, which have been observed from impulse corona [5]. It also provides a rough agreement with experimental measurements of surface charge distributions from PD, [77], and from detailed streamer simulations [57]. The use of Gaussian functions to model charge distributions were also investigated, as they have been used in the literature [80], but it was

found that PDs of sufficient magnitude could not be generated without the charge spots overlapping. A plot of (3.11) is shown in Figure 3.1.

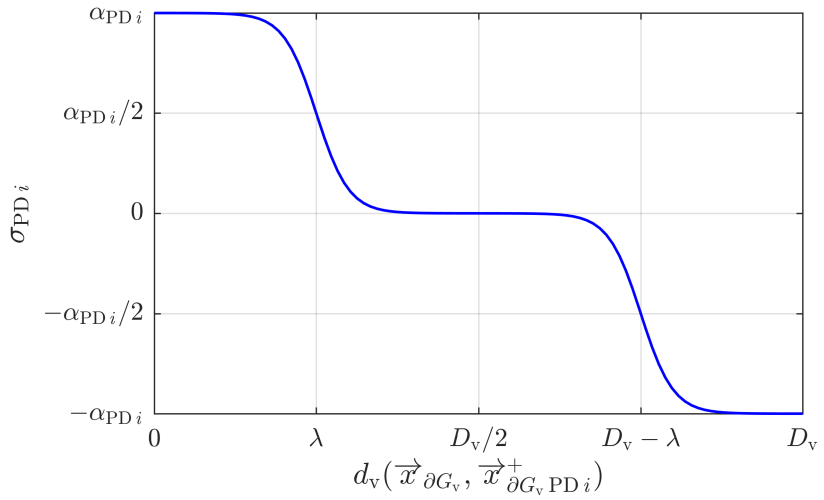

FIGURE 3.1: Figure showing $\sigma_{\mathrm{PD}\,i}$ along a geodesic on the surface of the defect between $\vec{x}^{+}_{\partial G_{\mathrm{v}}\,\mathrm{PD}\,i}$ and $\vec{x}^{-}_{\partial G_{\mathrm{v}}\,\mathrm{PD}\,i}$, $D_{\mathrm{v}} = d_{\mathrm{v}}\left(\vec{x}^{+}_{\partial G_{\mathrm{v}}\,\mathrm{PD}\,i}, \vec{x}^{-}_{\partial G_{\mathrm{v}}\,\mathrm{PD}\,i}\right)$.

Between discharges surface charge density can decay through a number of physical mechanisms. One of these is surface conduction leading to recombination of charge on the defect surface. In previous Poisson PD models the conduction of charge along the surface of the defect has been modelled using FEA [4]. However, in this model it will be neglected for the sake of practicality. This is because to model surface conduction using FEA must be solved on the surface of the defect a transport equation for the surface charge must be solved at all time steps [51, 81, 82]. For a three-dimensional geometry solving (3.1) once requires a computational time in the order of hours in current implementation of the model. If (3.1) had to be solved for every time step, this leads to a total simulation run time in the order of 10^6 hours, which is clearly impractical. The issue is compounded by the fact that the surface conductivity κ_s is a free parameter, which means that multiple simulation runs may be required with different values of κ_s. It should also be noted that surface charge may decay through mechanisms other than surface conduction, notably by emission back into the void. In the model it will be assumed that if the decay of surface charge is important, σ obeys an exponential decay between discharges as follows

$$\sigma(\vec{x}_{\partial G_{\mathrm{v}}}, t; \tau_\sigma) = \sigma(\vec{x}_{\partial G_{\mathrm{v}}}, t^{+}_{\mathrm{PD}\,i}) \exp\left(-\frac{t - t_{\mathrm{PD}\,i}}{\tau_\sigma}\right) \text{ where } t_{\mathrm{PD}\,i} \leq t < t_{\mathrm{PD}\,i+1}, \tag{3.12}$$

where τ_σ is a time decay constant. The assumption of an exponential decay of surface charge, and the electric field it creates, has been used previously by other researchers [45, 79].

3.4 Electron Generation

Electron generation processes have been used to introduce stochastic components to PD modelling, an approach which is adopted here through (3.8). In the PD systems considered using this model, only two mechanisms of electron generation will be considered. Surface emission from insulators and surface emission from metals. The electron generation rate must be computed at all generation points in the PD system, in order to avoid location bias the points must be evenly spaced.

Surface emission from insulators is governed by the equation developed by Niemeyer, (2.1). Adapting this for multiple generation points gives

$$\dot{N}_{\mathrm{e}\,s\,i}(N_{\mathrm{dt}\,i}, E_{\mathrm{gen}\,i}; T, \Phi) = \nu_0 N_{\mathrm{dt}\ i} \exp\left(\frac{1}{k_{\mathrm{B}}T}\left[\sqrt{\frac{e^3 E_{\mathrm{gen}\,i}}{4\pi\varepsilon_0}} - \Phi\right]\right), \tag{3.13}$$

where $\dot{N}_{\mathrm{e}\,s\,i}$ is the electron generation rate due to surface emission at generation point i, $N_{\mathrm{dt}\ i}$ is the detrappable charge population in the vicinity of the ith generation point and $E_{\mathrm{gen}\,i}$ is the field governing emission at generation point i, which is explicitly

$$E_{\mathrm{gen}\,i} = |\vec{E}(\vec{x}_{\mathrm{gen}\,i}, t) \cdot \vec{n}(\vec{x}_{\mathrm{gen}\,i})| \tag{3.14}$$

where $\vec{n}$ is a normal vector on the insulator surface [1]. However, the model departs from Niemeyer's work in assuming that the detrappable charge population N_{dt} is distributed between two traps of different depths, referred to as deep and shallow. It will be assumed that a fraction χ_{s} of the total detrappable charge from a PD moves into shallow traps with time decay constant $\tau_{\mathrm{dt\ s}}$. The remaining detrappable charge moves into deep traps with time decay constant $\tau_{\mathrm{dt\ d}}$. The amount of detrappable charge is reset at each PD event, based on the change in the charge population at each generation point. The detrappable charge population at the ith generation point after the jth discharge is then

$$N_{\mathrm{dt}\,i}(t, t_{\mathrm{PD}\,j}; \chi_{\mathrm{s}}, \tau_{\mathrm{dt\ s}}, \tau_{\mathrm{dt\ d}}) = \ldots$$
$$N_{\mathrm{dt}\,i\,\mathrm{PD}\,j}\left[\chi_{\mathrm{s}} \exp\left(-\frac{t - t_{\mathrm{PD}\,j}}{\tau_{\mathrm{dt\ s}}}\right) + (1 - \chi_{\mathrm{s}}) \exp\left(-\frac{t - t_{\mathrm{PD}\,j}}{\tau_{\mathrm{dt\ d}}}\right)\right] \tag{3.15}$$

where $t_{\mathrm{PD}\,j} < t < t_{\mathrm{PD}\,j+1}$ and $N_{\mathrm{dt}\,i\,j\,0}$ is the detrappable charge population in the vicinity of the ith generation point immediately after the jth discharge. It will be assumed that all of the charge deployed by a discharge is initially detrappable following Niemeyer's

[1] It was noted in the literature review that (3.13) appears to be incorrect. This error was only discovered after the work in this thesis had already been conducted, however, the use of this equation does not invalidate any of the conclusions resulting from this work.

model [17]. This means that

$$N_{\mathrm{dt}\,i\,j\,0}(\Delta\sigma_{\mathrm{gen}\,i\,\mathrm{PD}\,j}; A_{\mathrm{gen}}, N_{\mathrm{gen}}) = \frac{|\Delta\sigma_{\mathrm{gen}\,i\,\mathrm{PD}\,j}|\, A_{\mathrm{gen}}}{N_{\mathrm{gen}} e}. \tag{3.16}$$

where $\Delta\sigma_{\mathrm{gen}\,i\,\mathrm{PD}\,j}$ is the change in surface charge density at the ith generation point due to the jth PD, which is explicitly

$$\Delta\sigma_{\mathrm{gen}\,i\,\mathrm{PD}\,j} = \sigma(\vec{x}_{\mathrm{gen}\,i}, t^{+}_{\mathrm{PD}\,j}) - \sigma(\vec{x}_{\mathrm{gen}\,i}, t^{-}_{\mathrm{PD}\,j}). \tag{3.17}$$

(3.16) can be understood as follows. Firstly, the area of the surface associated with each generation point is $A_{\mathrm{gen}}/N_{\mathrm{gen}}$. In this area is sufficiently small, i.e. a large number of generation points, it is reasonable to assume that the surface charge density within this area is uniform. Therefore the number of charge carriers that will be deposited at a generation point by a PD is simply the change in surface charge density at the generation point, divided by the charge e, multiplied by the area associated with that generation point.

The concept of a two trap depths was first used to model the decay of trapped charge in polymers [83, 84]. Subsequently, it was also found to provide a good description of charge detrapping in ice [85]. This is an encouraging result as it implies that a two level exponential decay of detrappable charge may occur in a variety of systems. It should be noted that charge detrapping from PD has not been explicitly measured, the assumption of two trap levels was used, because it is a mechanism which is able to explain observed PD activity, and has a basis in the literature.

In Niemeyer's work the equation for the electron generation rate from surface emission from metallic surfaces is said to obey the Richardson-Schottky law [17]. As was noted in the literature this seems highly erroneous, and emission from metals in PD systems is likely to a combination of complex physical mechanisms. To simplify this emission from metallic surface will be assumed to scale with the cube of the electric field,

$$\dot{N}_{\mathrm{e\,s}\,i}(E_{\mathrm{gen}\,i}; c_e, N_{\mathrm{gen}}) = \frac{c_e}{N_{\mathrm{gen}}} |E_{\mathrm{gen}\,i}|^3, \tag{3.18}$$

where c_e is a free parameter. This is based on a previous fitting function used in the literature to describe the electron generation rate for PD activity from metallic electrodes [79], it should not be seen as having a physical meaning.

3.5 Measurable Quantities of PD

This model is applied to PD systems under AC conditions. In these systems, PDs are classified by an apparent charge, q'_{PD}, and a phase angle φ_{PD}. The phase angle is simply the point in the point in the AC cycle where the PD occurs, which means that for a PD

at time $t_{\mathrm{PD}\,i}$ the phase angle of the PD in radians is

$$\varphi_{\mathrm{PD}\,i} = \omega t_{\mathrm{PD}\,i} \pmod{2\pi}. \tag{3.19}$$

The apparent charge is the change in the charge across a measurement electrode. Therefore by definition for the ith discharge the apparent charge $q'_{\mathrm{PD}\,i}$ is

$$q'_{\mathrm{PD}\,i} = \int_S \left(\vec{D}(\vec{x}_{\partial G_\mathrm{m}}, t^+_{\mathrm{PD}\,i}) - \vec{D}(\vec{x}_{\partial G_\mathrm{m}}, t^-_{\mathrm{PD}\,i}) \right) \cdot \vec{n}(\vec{x}_{\partial G_\mathrm{m}})\, dS, \tag{3.20}$$

where ∂G_m is boundary of the measuring electrode and $\vec{n}$ is the normal vector an outward facing normal unit vector at the measuring electrode surface.

3.6 Model Implementation

The equations that govern the PD model cannot be solved analytically in the cases considered, the equations must be solved numerically using the appropriate software. The approach adopted, which is has been previously used in PD modelling, is to use MATLAB linked with COMSOL, to make use of MATLAB's coding environment and COMSOL's meshing and finite element method numerical solver [52, 86]. For the problems under consideration the numerical solution of the equations was not particularly complex, and the details of the mesh used will not be discussed, in all cases mesh refinement was performed until the variation in the electric field was less than 1%. As mentioned in Section 3.3 for complex three dimensional geometries it is not possible to solve FEA model at all time steps. Fortunately, this can be avoided by making certain observations and splitting the electric field into applied components, $\vec{E}_0$, and local components, $\vec{E}_\mathrm{l}$, as follows

$$\vec{E}(\vec{x}, t) = \vec{E}_0(\vec{x}, t) + \vec{E}_\mathrm{l}(\vec{x}, t). \tag{3.21}$$

The applied field $\vec{E}_0$ is found through

$$\vec{E}_0(\vec{x}, t) = -\vec{\nabla} V_0(\vec{x}, t), \tag{3.22}$$

where V_0 is the applied voltage which satisfies

$$\nabla^2 V_0(\vec{x}, t) = 0, \tag{3.23}$$

on the PD system, with all Dirichlet boundary conditions the same as for V. The components of the applied field will be directly proportional to the voltages on all electrodes in the system. Using this the applied field can be found for all t, using only a few solutions of (3.1), with the exact number of solutions dependent on the PD system under consideration. It should be noted that under AC conditions all components of $\vec{E}_0$ will have the same period as the AC cycle.

The local electric field $\vec{E}_\mathrm{l}$ can be found by solving

$$\vec{E}_\mathrm{l}(\vec{x},t) = -\vec{\nabla}V_\mathrm{l}(\vec{x},t), \tag{3.24}$$

where V_l is the local potential which satisfies

$$\nabla^2 V_\mathrm{l}(\vec{x},t) + \frac{\rho(\vec{x},t)}{\varepsilon_0\varepsilon_r(\vec{x})} = 0, \tag{3.25}$$

on the PD system, with all Dirichlet boundary conditions set to zero. By definition, V_l and E_l are both directly proportional to ρ as (3.25) is a linear equation and $V_\mathrm{l} = 0$ when $\rho = 0$. From (3.10) and (3.12), it is clear that after N_PD PDs σ can be written using the superposition principle as

$$\sigma(\vec{x}_{\partial G_\mathrm{v}}, t; \tau_\sigma) = \sum_{i=1}^{N_\mathrm{PD}} \sigma_{\mathrm{PD}\,i}(\vec{x}_{\partial G_\mathrm{v}})\exp\left(-\frac{t - t_{\mathrm{PD}\,i}}{\tau_\sigma}\right), \tag{3.26}$$

which means

$$\vec{E}_\mathrm{l}(\vec{x},t;\tau_\sigma) = \sum_{i=1}^{N_\mathrm{PD}} \vec{E}_{\mathrm{l}\,\mathrm{PD}\,i}(\vec{x})\exp\left(-\frac{t - t_{\mathrm{PD}\,i}}{\tau_\sigma}\right) \tag{3.27}$$

where $\vec{E}_{\mathrm{l}\,\mathrm{PD}\,i}$ is the local electric field from the ith discharge immediately after it occurs, which is from (3.6)

$$\vec{\nabla}\cdot\vec{E}_{\mathrm{l}\,\mathrm{PD}\,i}(\vec{x}) = \delta(\varsigma)\sigma_{\mathrm{PD}\,i}(\vec{x}_{\partial G_\mathrm{v}}). \tag{3.28}$$

Therefore in order to determine E_l all that is required is to determine the electric field from the surface charge distribution of each PD $\sigma_{\mathrm{PD}\,i}$. Furthermore, the constant of proportionality between the electric field due to discharge i, $\vec{E}_{\mathrm{l}\,\mathrm{PD}\,i}$, and the surface charge density from it, $\sigma_{\mathrm{PD}\,i}$, will clearly be independent of the charge spot magnitude, $\alpha_{\mathrm{PD}\,i}$; it will only depend on the spatial distribution of charge, $\sigma_{\mathrm{PD}\,i}/\alpha_{\mathrm{PD}\,i}$. Therefore, in order to determine the local field for all time steps a single FEA solution is required for each spatial distribution of $\sigma_{\mathrm{PD}\,i}$ in order to determine the appropriate constants of proportionality. It should be noted that the model is only dependent on a single component of the electric field at the inception and generation points: (3.7), (3.9) and (3.13). The constants of proportionality of interest are the following tensors:

- $c_{\mathrm{l}\,ijk}$- The constant of proportionality between the local electric field component at generation point i and the local electric field component at inception point j for the spatial distribution of surface charge k.

- $c_{\alpha\, ijk}$- The constant of proportionality between the surface charge density at generation point i and the local electric field component at inception point j for the spatial distribution of surface charge k.

- $c_{q'\, ij}$- The constant of proportionality between the local electric field component at inception point i and the apparent charge on the measuring electrode for the spatial distribution of surface charge j.

In each case the constant of proportionality is relative to the local electric field component at each inception point. This is because the local electric field at a single inception point when a discharge occurs is known, it will be adjusted during a discharge such that the residual condition is met, (3.9). These constants of proportionality allow the other model variables to be determined from them.

The stages of model implementation are therefore as follows:

1. Build and mesh the PD system geometry in COMSOL and using the electrostatics physics library implement the correct boundary conditions.

2. Solve as required to find the applied electric field at all inception and generation points.

3. For all spatial distributions of surface charge, $\sigma_{\mathrm{PD}\,i}$, find the local electric field at all inception and generation points, and the apparent charge on the measuring electrode. Use this to determine the constants of proportionality. This calculation is often implemented using MATLAB with COMSOL.

4. Implement the governing equations for the model in MATLAB, using the proportionality constants calculated previously the electric field at all inception and generation points can now be determined at all times.

5. Run the model with different free parameter combinations until a reasonable fit with experimental data is achieved.

It should be realised that splitting the electric field into local and applied components is simply a technique to reduce the computational cost, it does not change the model.

3.7 Discussion

Some of the extensions introduced in this chapter have addressed issues raised in the discussion section of the previous chapter. The three key improvements are as follows:

1. Inception and Generation Points - The model considers the inception of a discharge and the electron generation processes at a range of locations in the PD system. Previous models assumed that these processes were governed by the electric field at a single point in the system. This is thought to be more physical description of the system.

2. Two Electron Trap Depths - Based on measurements and modelling of charge detrapping in the literature, [83], the detrappable electron population is split between two trap depths. This is different to other approaches in the PD modelling literature, where it was concluded that either charge detrapping was dependent on the polarity of the surface charge [4, 17], or that the effective work function of the surface is altered due to discharge events [45]. However, neither of these approaches are based on experimental evidence, whereas the existence two electron trap depths, while not investigated in PD systems, has been shown to exist as an effective method of modelling charge detrapping.

3. Surface Charge Density Distributions - Surface charge density distributions, due to discharge activity, in an earlier Poisson PD model were discrete, [4], which leads to discontinuities in the electric field at the surface. In this work the distributions were continuous, using logistic functions, which avoids discontinuities and is in approximate agreement with measurements of surface charge density from discharge activity in the literature [5, 6, 7].

These improvements result in a model which is thought to capture more of the physics present in PD systems, while fixing some of the shortcomings in earlier work.

3.8 Conclusion

Extensions have been proposed to existing PD models to more accurately describe PD activity in a variety of systems. The general PD model proposed has in full 9 unmeasurable physical parameters: E_{inc}, E_{res}, η_{PD}, λ_{PD}, τ_{σ}, Φ, χ_{s}, $\tau_{\text{dt s}}$ and $\tau_{\text{dt d}}$. The number of free parameters, i.e. those adjusted such that the model matches experiment, will depend on the PD system under consideration, and care will be taken to try and use as few free parameters as possible. In the systems considered 3 or 4 free parameters were required for the model to give physically sensible results.

Chapter 4

Modelling Partial Discharges in Voids between Parallel Plate Electrodes

In this section the model introduced in Chapter 3 is validated against experimental data in the literature for PD activity inside a spherical air filled void surrounded by epoxy resin [4]. For completeness all stages of the model implementation will be discussed, this will not be the cases with the other models presented in this work as the process is essentially the same. Once the model was successfully able to reproduce experimental measurements it was used to investigated the possible impact of void deformation on PD activity. The work presented in this chapter is an improvement of earlier work by the author [11].

4.1 Model Geometry

The model geometry is set to match the experimental arrangement, it is axisymmetric, containing a spherical air filled void with a radius, R_{v}, of 0.7 mm centred between parallel plates with a separation, L_{plate}, of 2 mm [4]. As the system is axisymmetric an axisymmetric cylindrical coordinate system is used, with height z and radial distance r_{c}, centred on the void. The model geometry is shown in Figure 4.1.

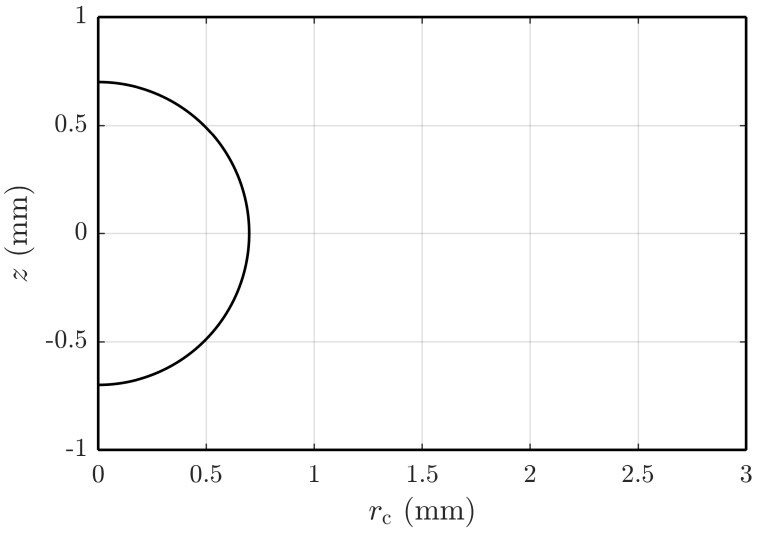

FIGURE 4.1: Model geometry used in the validation of the PD model.

4.2 Electric Field

In the example there is only a single interior boundary, at the intersection between the spherical void and the epoxy resin, where the interior boundary conditions, (3.3) and (3.4), are applied. Inside the void $\varepsilon_r = \varepsilon_{r\,\mathrm{v}} = 1$ and in the epoxy resin $\varepsilon_r = \varepsilon_{r\,\mathrm{e}} = 4.4$. The external boundary conditions for the electrostatic potential $V(r_\mathrm{c}, z, t)$, in axisymmetric cylindrical coordinates, with origin at the centre of the void, are

$$V\left(r_\mathrm{c}, {}^{L_\mathrm{plate}}/_2, t; U_0, \omega\right) = U_0 \sin(\omega t) \tag{4.1}$$

$$V\left(r_\mathrm{c}, {}^{-L_\mathrm{plate}}/_2, t\right) = 0 \tag{4.2}$$

$$\frac{\partial}{\partial r_c}\left(V(r_\mathrm{c} \gg R_\mathrm{v}, z, t)\right) = 0. \tag{4.3}$$

where $U_0 = 18$ kV is the maximum applied voltage and $\omega = 100\pi$ is the angular frequency of the AC cycle. Charge is only present at the boundary of the sphere, so ρ can be written as

$$\rho(r, \phi, t) = \delta(r_c^2 + z^2 - R_\mathrm{v}^2)\sigma(\phi, t), \tag{4.4}$$

where ϕ is the polar angle on void surface

$$\phi = \pi/2 - \arctan(z/r_\mathrm{c}). \tag{4.5}$$

4.3 Inception and Generation Processes

In the example only electron generation from surface emission will be considered, as it is likely to be the dominant physical process and simplifies the problem. In this case, surface charge from previous PDs emits free charge into the void, which can begin a discharge. As previously mentioned surface emission will be dependent on the field normal to the void surface so at each generation point has a normal vector $\vec{n}$ associated with it to calculate the surface emission rate (3.13). Discharges are likely to align with the direction of the electric field as they move through the void. This means that the paths of all discharges are likely to coincide with points near the centre of the void. As charge is deposited at the boundary of the void, the electric field in the centre of the void has the highest magnitude. Therefore, only a single inception point is required, $N_{\text{inc}} = 1$, which is at the centre of the void. Furthermore, it is assumed that the discharge will be propagating in alignment with the electric field at the centre of the void. Therefore,

$$\vec{x}_{\text{inc}\,1} = (0, 0) \tag{4.6}$$

and

$$\vec{e}_{\text{inc}\,1} = \vec{e}_z \tag{4.7}$$

where $\vec{e}_z$ is a unit vector in the z direction, using the same coordinate system as (4.1), (4.2) and (4.3). The next step is to determine the generation points. As surface emission occurs at all points on the void surface, it is required that the generation points span the entire surface of the void. To avoid location bias, this means generation points must be evenly spaced on the surface of a sphere. As the system is axisymmetric this means that each generation point must cover a ring of area $4\pi R_{\text{v}}^2/N_{\text{gen}}$. A distribution of points that achieves this is

$$\phi_{\text{gen}\,i} = \arccos\left(\cos(\phi_{\text{gen}\,i-1}) - \frac{2}{N_{\text{gen}}}\right) \tag{4.8}$$

where $\phi_{\text{gen}\,i}$ is the polar angle of the ith generation point and

$$\phi_{\text{gen}\,1} = \arccos\left(1 - \frac{1}{N_{\text{gen}}}\right). \tag{4.9}$$

A derivation of (4.8) and (4.9) is provided in Appendix B. For streamer discharges in an air filled void, occurring in an approximately uniform electric field, E_{inc} and E_{res} can be related to the air pressure in the void, p, as follows

$$E_{\text{inc}} \;=\; (E/p)_{\text{cr}} p \left(1 + \tfrac{B}{(2pR_{\text{v}})^{1/2}}\right) \tag{4.10}$$

and

$$E_{\text{res}} = \gamma (E/p)_{\text{cr}} p \tag{4.11}$$

where p is the pressure in the void, $(E/p)_{\text{cr}} = 25.2$ V Pa^{-1} m^{-1} is the constant of proportionality between the critical electric field E_{cr} required to sustain the discharge and p, $B = 8.6$ Pa$^{1/2}$ m$^{1/2}$ and $\gamma = 0.35$ [17, 39, 40]. A schematic showing the inception point and one of the generation points is provided in Figure 4.2.

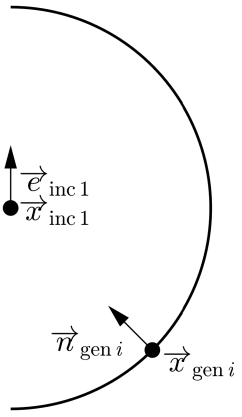

FIGURE 4.2: Schematic showing the inception point and one of the generation points on the void surface with their associated unit vectors.

4.4 Surface Charge Dynamics

In this case the simplifying assumption that discharges are propagating along the symmetry axis has been made. Therefore the charge spots will be centred along the symmetry axis, so

$$\phi^{+}_{\text{PD}\,i} = 0 \text{ and } \phi^{-}_{\text{PD}\,i} = \pi \tag{4.12}$$

if

$$\vec{E}(0, 0, t^{-}_{\text{PD}}) \cdot \vec{e}_z > 0 \tag{4.13}$$

and

$$\phi^{+}_{\text{PD}\,i} = \pi \text{ and } \phi^{-}_{\text{PD}\,i} = 0, \tag{4.14}$$

if

$$\vec{E}(0, 0, t^{-}_{\text{PD}}) \cdot \vec{e}_{\text{z}} < 0. \tag{4.15}$$

This means that $\sigma_{\mathrm{PD}\,i}$ can be written explicitly as

$$\begin{aligned}\sigma_{\mathrm{PD}\,i}(\phi, \alpha_{\mathrm{PD}\,i}; \lambda_{\mathrm{PD}}, \eta_{\mathrm{PD}}) &= \underbrace{\frac{\alpha_{\mathrm{PD}\,i}}{1+\exp\left(\eta_{\mathrm{PD}}\left[\phi R_{\mathrm{v}} - \lambda_{\mathrm{PD}}\right]\right)}}_{\text{Charge Spot at Top of Void}} \cdots \\ &- \underbrace{\frac{\alpha_{\mathrm{PD}\,i}}{1+\exp\left(\eta_{\mathrm{PD}}\left[(\pi-\phi) R_{\mathrm{v}} - \lambda_{\mathrm{PD}}\right]\right)}}_{\text{Charge Spot at Bottom of Void}}\end{aligned} \tag{4.16}$$

A plot of $\sigma_{\mathrm{PD}\,i}$ on the surface of the void is shown in Figure 4.3. The experiment is performed in a virgin void so it is expected that the surface conductivity is likely to be very low, as such the decay of surface charge will be neglected.

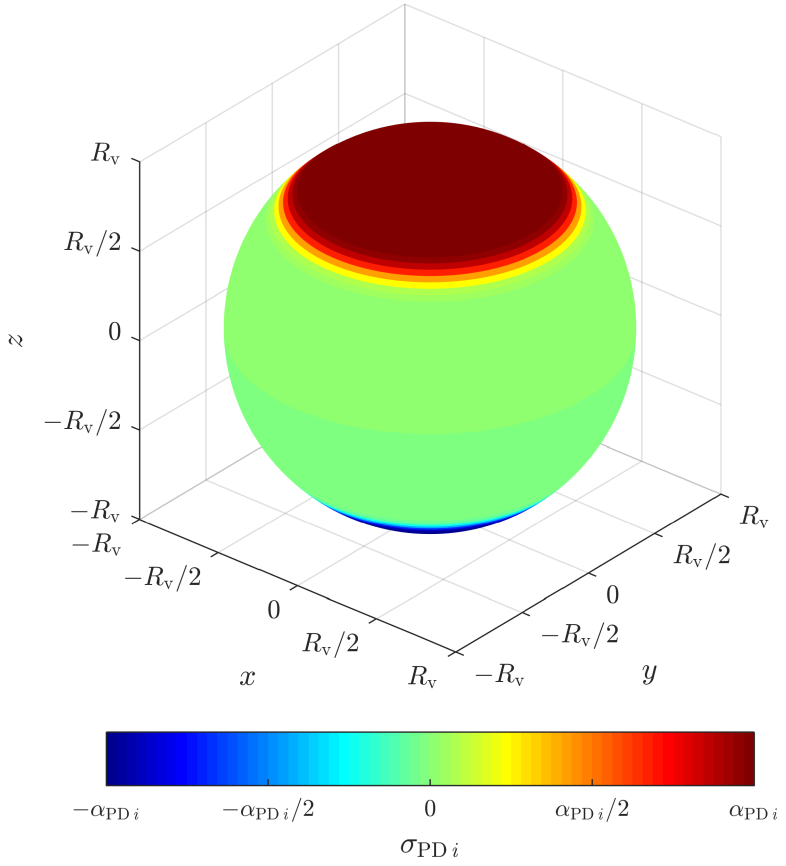

FIGURE 4.3: Figure showing $\sigma_{\mathrm{PD}\,i}$ on the surface of the spherical void with $\vec{E}(0,0,t_{\mathrm{PD}}^{-}) \cdot \vec{e}_z > 0$, $\eta_{\mathrm{PD}} = 100/\pi R_{\mathrm{v}}$ and $\lambda_{\mathrm{PD}} = \pi R_{\mathrm{v}}/4$.

4.5 Measurable Quantities of PD

The phase angle from the discharge can be determined using (3.19). The measuring electrode is the ground electrode, which means the apparent charge is explicitly

$$q'_{\mathrm{PD}\,i} = \int_{r_\mathrm{c}=0\ \mathrm{mm}}^{r_\mathrm{c}=3\ \mathrm{mm}} \left(\vec{D}(r_\mathrm{c}, {}^{-L_\mathrm{plate}}\!/_2, t^+_{\mathrm{PD}\,i}) - \vec{D}(r_\mathrm{c}, {}^{-L_\mathrm{plate}}\!/_2, t^-_{\mathrm{PD}\,i})\right) \cdot \vec{e}_z\, 2\pi r_\mathrm{c}\, dr_\mathrm{c}. \quad (4.17)$$

4.6 Model Implementation

In this case the applied field is directly proportional to the voltage on the high voltage plate, so only one solution of the electrostatic equation is required to find $\vec{E}_0$, for simplicity the high voltage electrode is set to U_0. A plot of the applied field for $V\left(r_\mathrm{c}, {}^{L_\mathrm{plate}}\!/_2, t; U_0, \omega\right) = U_0$ is shown in Figure 4.4.

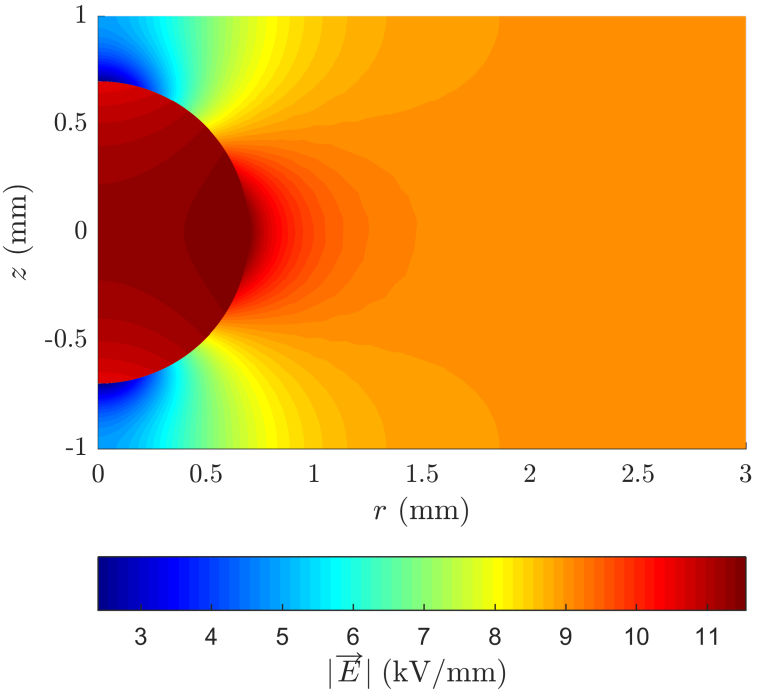

FIGURE 4.4: Plot of electric field magnitude from the numerical solution to determine $\vec{E}_0$.

Using this numerical solution the applied component of the electric field at the inception point and the generation points can be determined as simply the value from this calculation multiplied by $\sin(\omega t)$.

The local component of the electric field requires one solution per spatial distribution of surface charge, in this case 20 distributions each with different λ_{PD} were considered, in all cases η_{PD} was set to $100/\pi R_{\mathrm{v}}$ as it was not found to significantly impact the model results. The local electric field for $\lambda_{\mathrm{PD}} = \pi R_{\mathrm{v}}/4$, $\eta_{\mathrm{PD}} = 100/\pi R_{\mathrm{v}}$ with α_{PD} set to a token value of 0.1 nC/mm^2 is shown in Figure 4.5.

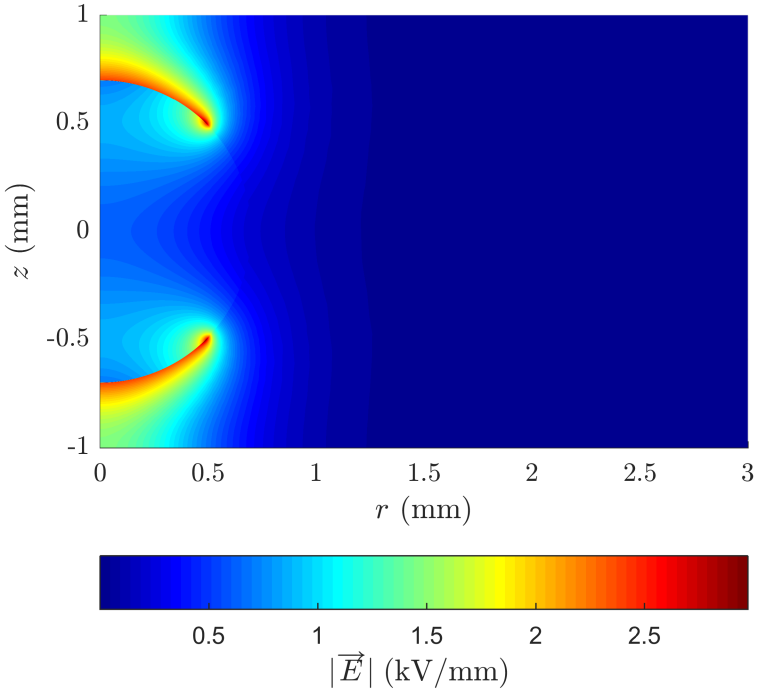

FIGURE 4.5: Plot of electric field magnitude from the numerical solution to determine $\vec{E}_{\mathrm{l}}$.

This FEA calculation is then used to determine three constants of proportionality that will be required, namely:

1. $c_{\mathrm{l}ij}$ - The constant of proportionality between the local electric field normal to the surface at generation point i and the local electric field, in the direction of the discharge, at the inception point for surface charge distribution j.

2. $c_{\alpha ij}$ - The constant of proportionality between the surface charge density magnitude, $\alpha_{\mathrm{PD}\,i}$ and the local electric field, in the direction of the discharge, at the inception point for surface charge distribution j.

3. $c_{q'i}$ - The constant of proportionality between the apparent charge and the local electric field, in the direction of the discharge, at the inception point for surface charge distribution i.

4.7 Parameters

Using these constants of proportionality the PD model can be implemented in MATLAB and run with different free parameter combinations until a suitable fit with experimental data is achieved. For this case the four free parameters are the spread of charge along the void surface λ_{PD}, the work function of the void surface Φ the fraction of traps which are shallow χ_{s} and the time decay constant of shallow traps τ_{s}. The decay of surface charge and the time decay constant of deep traps will both be neglected. This is because it is not thought they will significantly impact the discharge activity, and it will also reduce the number of free parameters in the model. The pressure p, which is used to determine E_{inc} and E_{res}, is not regarded as a free parameter. This is because the PD with the minimum apparent charge will result from a discharge occurring at E_{inc}. The value of λ_{PD} determines the constant of proportionality between the electric field due to a discharge, which for the smallest magnitude PD will be $E_{\mathrm{inc}} - E_{\mathrm{res}}$, and the apparent charge. Therefore once λ_{PD} is set, (4.10) and (4.11) can be used to determine the pressure that will result in the minimum apparent charge in the model matching the minimum apparent charge in the experiment. For the parameters chosen this resulted in an air pressure in the void of 61.2 kPa, which is close to previous values of air pressure set for PD in spherical air filled voids in epoxy [9]. All of the parameters used in the model are provided in Table 4.1.

Parameter Group	Parameter	Value
Geometry	L_{plate}	2 mm
	R_{v}	0.7 mm
Electric Field	$\varepsilon_{r\,\mathrm{v}}$	1
	$\varepsilon_{r\,\mathrm{e}}$	4.4
	U_0	18 kV
	ω	100π
Inception	p	61.2 kPa
Surface Charge Dynamics	η_{PD}	$\frac{100}{\pi R_{\mathrm{v}}}$
	$\lambda_{\mathrm{PD}}{}^{*}$	$\frac{R_{\mathrm{v}}\pi}{4}$
Electron Generation	Φ^{*}	1.25 eV
	T	27 °C
	$\chi_{\mathrm{s}}{}^{*}$	0.999
	$\tau_{\mathrm{dt\,s}}{}^{*}$	1 ms

* Free parameter

TABLE 4.1: Model Parameter Values for PD Activity in a Spherical Void

4.8 Partial Discharge Activity in a Spherical Void

The model was able to reproduce the PD activity observed in the experiment, with the typical 'rabbit ear' PRPD pattern shown in Figure 4.6. Due to the stochastic nature of the model 5000 simulated AC cycles were simulated such that the statistical quantities of PD activity were reproducible between simulation runs. The simulated PRPD pattern only shows discharge activity over 500 AC cycles as it allows regions of 'dense' PD activity to be identified visually.

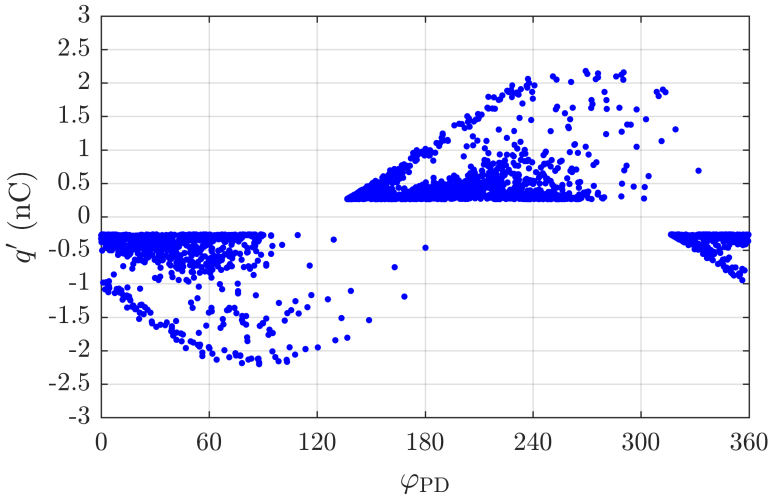

FIGURE 4.6: Simulated PD activity from a spherical void in a parallel plate system.

There is also good agreement between the statistical quantities of PD activity in the model and experiment, an overview is provided in Table 4.2.

Quantity	**Model**	**Experiment [4]**
PDs per AC cycle	5.8	5.7
Mean q'_{PD} (pC)	482	562
Min q'_{PD} (pC)	263	263
Max q'_{PD} (pC)	2302	2056

TABLE 4.2: Statistical Quantities of PD Activity in a Spherical Void

The model has been shown to be capable of reproducing PRPD patterns from experimental measurements of PD activity inside a spherical void surrounded by epoxy resin [4]. In the original work, the PD activity was simulated with a similar PD activity model and the agreement achieved with experiment was closer than the results presented in Table 4.2. However, it should be noted that in this work, 8 free parameters were used to fit the model to the experiment, whereas in this work only 4 were required. As was noted

in Chapter 2, the use of a large number of free parameters is a shortcoming of many PD models in the literature.

4.9 Partial Discharge Activity in Deformed Voids

The model has now been validated against experimental data, moving forward it is of interest to see what possible insight the model can give to PD activity from systems which cannot be investigated experimentally. It is thought that spherical voids may become deformed due to discharge activity, which is why earlier work has investigated, at least theoretically, the impact of ellipsoidal voids on PD [17, 39]. However, other deformations are clearly possible, it is proposed in this section to investigate the impact of void deformation on PD activity. Clearly in reality voids deformed by PD activity will have complex three dimensional geometries and will be subject to significant changes in surface chemistry, which is the beyond the scope of a simple PD model to fully capture. Instead it proposed to isolate the impact of void geometry on PD activity by rerunning the model with the same parameters as those Table 4.1, with the only change being the surface of the void. The void boundary will be considered as a parametric surface, with $r_c = R(\phi)\sin(\phi)$, $z = R(\phi)\cos(\phi)$ and

$$\begin{aligned} R(\phi; R_v, R_d, \eta_d, \lambda_d) &= R_v + \frac{R_d}{1+\exp(\eta_d(\phi-\lambda_d))} + \dots \\ &\quad \frac{R_d}{1+\exp(\eta_d(\pi-\phi-\lambda_d))}, \end{aligned} \tag{4.18}$$

where R_d is the radius of the deformation, λ_d is the angular spread of the deformation and η_d is the angular gradient of the deformation. Clearly when $R_d = 0$ the void is spherical and the results of the previous section will be recovered. To narrow the scope of the investigation, η_d and λ_d are set to $100/\pi$ and $\pi/10$ respectively. These values give rise to significantly deformed voids that have physically sensible dimensions. The model will be used to investigate the dependence of PD activity on the deformation radius R_d. The shape of the void surface is shown in Figure 4.7, for the two cases considered.

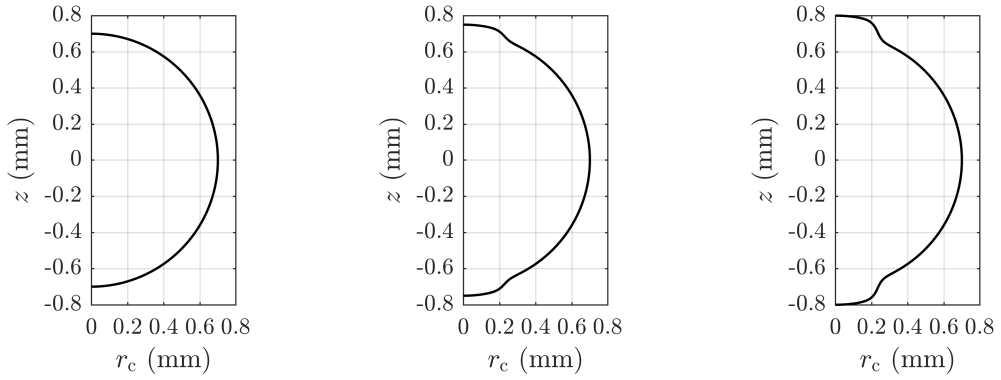

FIGURE 4.7: Figure showing the void surface with (a) $R_d = 0$ mm, (b) $R_d = 0.05$ mm and (c) $R_d = 0.1$ mm. In all plots $R_v = 0.7$ mm, $\eta_d = {}^{100}/_{\pi}$ and $\lambda_d = {}^{\pi}/_{10}$.

The model implementation for deformed voids is completely analogous to that of the spherical void and the for the sake of brevity it will not be discussed in detail. It should be noted however, that distributing the generation points evenly on the surface is no longer as trivial as it was in the spherical case. The approach taken is outlined in Appendix B.3.

The PRPD patterns for the two deformed voids that were considered are shown in Figure 4.6.. The PRPD patterns are noticeably different from the spherical void, with the formation of a second "ear" like structure. As before PD activity is simulated over 5000 AC cycles, with the PRPD patterns showing discharge activity for the first 500 AC cycles.

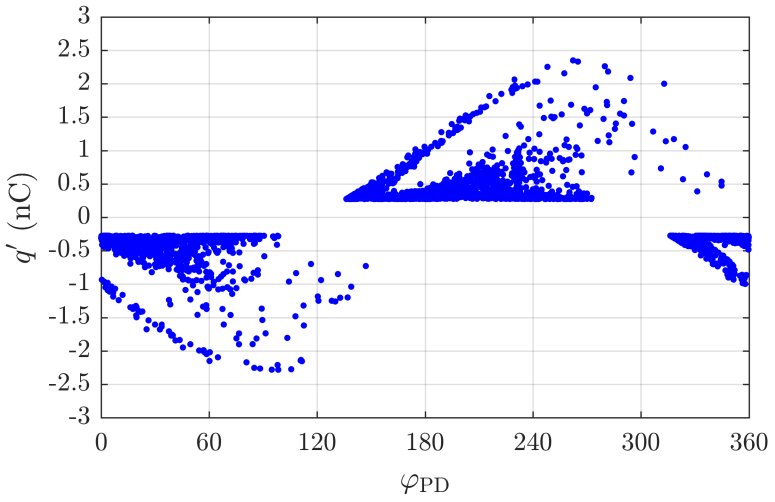

(a)

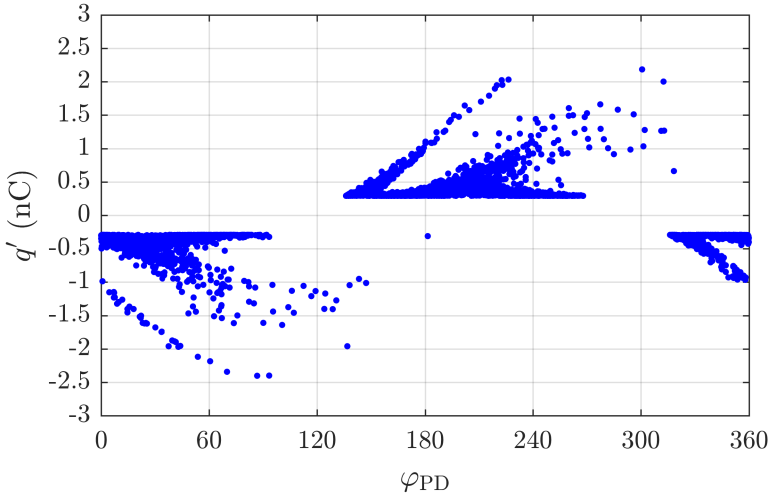

(b)

FIGURE 4.8: Simulated PD activity from deformed voids in a parallel plate system: (a) $R_{\mathrm{d}} = 0.05$ mm and (b) $R_{\mathrm{d}} = 0.1$ mm.

Compared to the results obtained for the spherical void case, the apparent charge magnitudes have also increased with the deformation radius, as has the number of PDs per AC cycle, see Table 4.3.

Quantity	$\boldsymbol{R_{\mathrm{d}} = 0.05}$ **mm**	$\boldsymbol{R_{\mathrm{d}} = 0.1}$ **mm**
PDs per AC cycle	6.9	8.5
Mean q'_{PD} (pC)	448	410
Min q'_{PD} (pC)	274	291
Max q'_{PD} (pC)	2355	2484

TABLE 4.3: Statistical Quantities of PD Activity in Deformed Voids

The model also shows how dependent PD activity can be on void geometry. The variation in PRPD structure and in PD statistical quantities with deformation is explained by the dependence of the electric field at the void surface on R_d. As R_d increases the electric field at the void surface increases around $\phi = \lambda_\mathrm{d}$ due to increase curvature, this increases the electron generation rate, which means PDs often occur as soon as the inception field is reached, hence the more distinct horizontal line structures in the PRPD patterns. This can result in nearly no net charge on the void surface after a half cycle. Furthermore, these low magnitude PDs do not deposit large amounts of charge the electron generation rate can quickly become very low, due to a small value of $\sigma(\vec{x}_{\mathrm{gen}\,i}, t^{+}_{\mathrm{PD}\,j}) - \sigma(\vec{x}_{\mathrm{gen}\,i}, t^{-}_{\mathrm{PD}\,j})$ in (3.16). This leads to the new "ear" structure, which is centered at the maximum of the applied electric field at 90° and 270°. The increase in apparent charge per cycle is a combination of two factors. Firstly, the increase in void size with R_d, so more charge is required at the boundaries to reduce the electric field in the void centre. Secondly, with increasing R_d the void surface becomes closer to the measuring electrode, and as such the charge at the surface has a greater influence on the electric field at the measuring electrode.

Investigations into the dependence of PD activity on variables such that void size, AC cycle frequency and temperature on spherical gaseous voids in epoxy resin has been previously conducted in the literature [8, 52]. From these investigations it was shown that PD magnitude and frequency are both highly dependent on these variables. However, the majority of PRPD patterns from these experiments exhibited the basic "rabbit ear" structure. From the modelling work conducted here it is suggested that void deformation can lead to markedly different PRPD patterns, as well as altering PD magnitude and frequency, even when the defect may not appear visually significant.

Despite the interesting results displayed by the model, there are improvements to be made in future work. An important point to consider is that deformations are likely to influence the spread of charge across the surface, which is dependent on λ_PD, although without using a plasma model of the discharge it is not clear what values of λ_PD would be appropriate for deformed voids. Furthermore, the aim of this work was to isolate the influence of void geometry, holding all other parameters constant. The fabrication of deformed voids would allow the simulation work conducted here to be validated against experiment.

4.10 Sustained Partial Discharge Activity in a Spherical Void

It is well known that sustained PD activity in voids can degrade insulation material and may ultimately initiate more severe processes which can lead to failure of high voltage plant [20]. PRPD patterns during sustained PD activity have been found to change with

time [9, 12, 87]. This is thought to be due to PD activity altering the gaseous composition of the void and surface chemistry at the void-dielectric boundary [20]. In [9], Gutfleisch and Niemeyer used a PD model to investigate PRPD patterns at different stages of ageing for a spherical void in epoxy resin. While the results appear to justify their approach, a significant omission in this work is that the statistical quantities of PD activity are not provided. The only comparison between simulated PD activity and experimental data is the shape of the PRPD patterns, which are shown with the apparent charge normalised. This means that it is not clear how well the model is able to reproduce the experimental data.

In this section an attempt is made to model PDs in a spherical void in silicone rubber during sustained discharge activity in order to provided insight into the physical processes taking place. The full experimental arrangement has been outlined in earlier work, [12], and for brevity will not be reproduced here. The model geometry is analogous to that shown in Figure 4.1, with a void radius of 0.825 mm and a plate separation of 3 mm. The applied voltage maximum U_0 was set to 23.4 kV to match experimental conditions. The model development and implementation was identical to the approach outlined in Sections 4.1 to 4.6.

In the experiment PD activity was measured at 30 minute intervals over 30 hours with each measuring session lasting approximately 10 minutes [12]. From analysis of the PRPD patterns, PD activity could be classified approximately into 5 distinct stages, shown in Table 4.4.

Stage	**Time (hours)**	**PD Activity**
1	0	'Rabbit-like' PRPD patterns
2	0.5-20	'Turtle-like' PRPD patterns
3	20-25	'Wing-like' PRPD patterns
4	25-27.5	'Rabbit-like' PRPD patterns with surface discharges
5	28-30	Swarming Pulsive Micro Discharges (SPMD) activity

TABLE 4.4: Stages of PD activity in a Spherical Void in Silicone Rubber

It should be noted that this is only an approximate overview of the discharge activity, and that even during the 10 minute measuring sessions significant variations in PD activity were observed. In order for experimental data to be permissible to modelling a data set is required where PD activity is consistent over a large number of AC cycles. For stages 1 to 4, data sets were extracted where PD activity produced a clearly defined PRPD pattern over a large number of AC cycles which was indicative of the PD activity over the stage as a whole. This was not found to be possible for Stage 5, as SPMD activity is associated with failure of the sample [12], and corresponds to infrequent low magnitude discharges. In Figure 4.9 the raw and extracted data sets are provided.

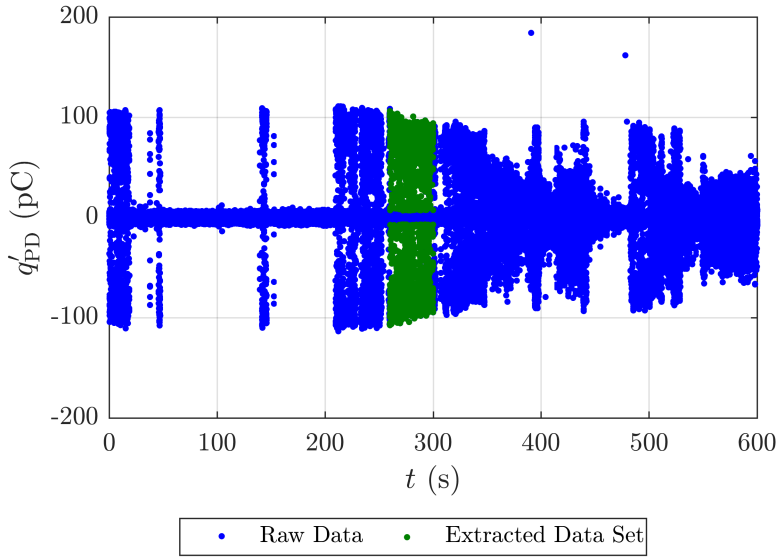

FIGURE 4.9: Figure showing the raw PD data measured 4 hours into the experiment with the data set, indicated by colour, which is indicative of PD activity during stage 2.

The PD model was then used to try and simulate PD activity for each of the data sets produced for stages 1 to 4. The fixed model parameters, assumed to be the same at all stages, are provided in Table 4.5.

Parameter Group	**Parameter**	**Value**
Geometry	L_{plate}	3 mm
	R_{v}	0.825 mm
Electric Field	$\varepsilon_{r\,\mathrm{v}}$	1
	$\varepsilon_{r\,\mathrm{r}}$	4
	U_0	23.4 kV
	ω	100π
Surface Charge Dynamics	η_{PD}	$\frac{100}{\pi R_{\mathrm{v}}}$
Electron Generation	T	27 °C

TABLE 4.5: Fixed Model Parameter Values for Sustained PD Activity in a Spherical Void

In stage 1, the free parameters were set in a similar manner to that outlined in Section 4.7. For the other stages it is not reasonable to assume that the void still contains air, it is very likely that a significant amount of oxygen has been removed from the air in the formation of by-products at the void surface. It is therefore inappropriate to use (4.10) and (4.11) to determine the inception and residual fields from the pressure [87]. As such

for stages 2 to 4 the inception field will be another independent free parameter, with the residual field set such that the minimum PD magnitude in the model matches that of the experiment. Furthermore, it was found that a significantly better fit with experiment could be achieved for stages 2 and 3 if the surface charge density was allowed to decay, (3.12), which introduces are extra free parameter τ_σ. The free model parameters are provided in Table 4.6.

Parameter Group	**Free Parameter**	**Stage**			
		1	2	3	4
Inception	p (kPa)	13.1	-	-	-
	E_{inc} (kV/mm)	-	9.1	7.7	6.2
Surface Charge Dynamics	λ_{PD} (mm)	$\frac{R_{\text{v}}\pi}{4}$	$\frac{R_{\text{v}}\pi}{4}$	$\frac{R_{\text{v}}\pi}{4}$	$\frac{R_{\text{v}}\pi}{4}$
	τ_σ (ms)	-	10	5	-
Electron Generation	Φ (eV)	1.29	1.14	1.22	1.24
	χ_{s}	0.95	0.999	0.9	0.9
	$\tau_{\text{dt s}}$ (ms)	2	0.01	0.01	0.1

TABLE 4.6: Free Model Parameter Values for Sustained PD Activity in a Spherical Void

The PRPD patterns of experiment and simulation are shown in Figures 4.10 to 4.13, with statistical quantities provided in Tables 4.7 to 4.10.

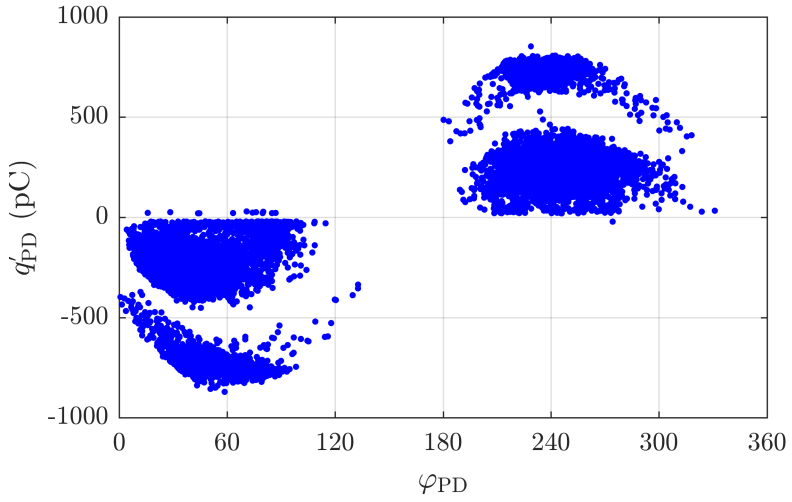

(a)

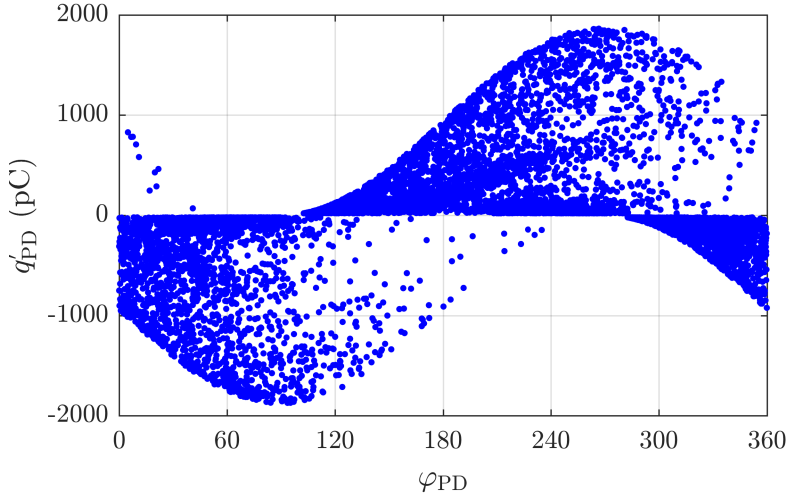

(b)

FIGURE 4.10: PRPD patterns at stage 1 of ageing: (a) experiment and (b) simulation.

Quantity	**Experiment**	**Simulation**
PDs per AC cycle	3.8	3.9
Mean q'_{PD} (pC)	473	431
Min q'_{PD} (pC)	20	20
Max q'_{PD} (pC)	871	1872

TABLE 4.7: Statistical Quantities of Sustained PD Activity in a Spherical Void at Stage 1

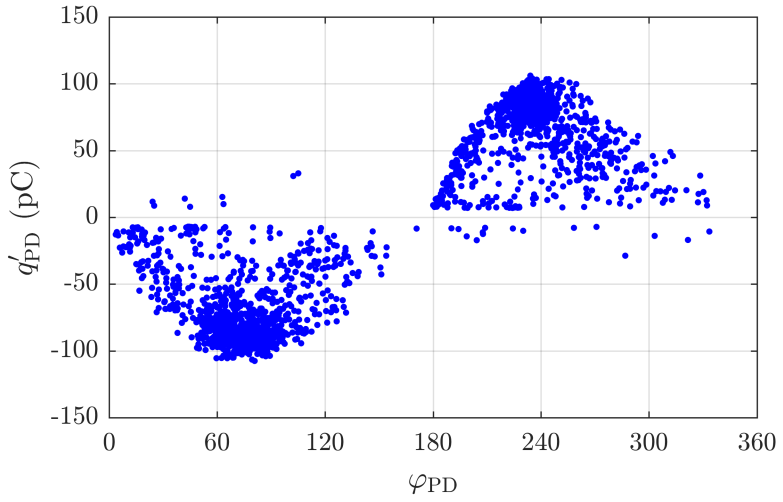

(a)

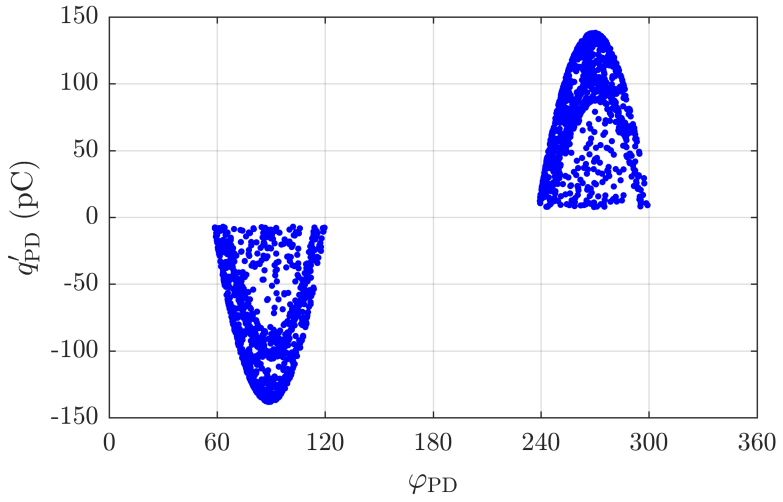

(b)

FIGURE 4.11: PRPD patterns at stage 2 of ageing: (a) experiment and (b) simulation.

Quantity	**Experiment**	**Simulation**
PDs per AC cycle	0.99	0.96
Mean q'_{PD} (pC)	66	76
Min q'_{PD} (pC)	7	7
Max q'_{PD} (pC)	108	138

TABLE 4.8: Statistical Quantities of Sustained PD Activity in a Spherical Void at Stage 2

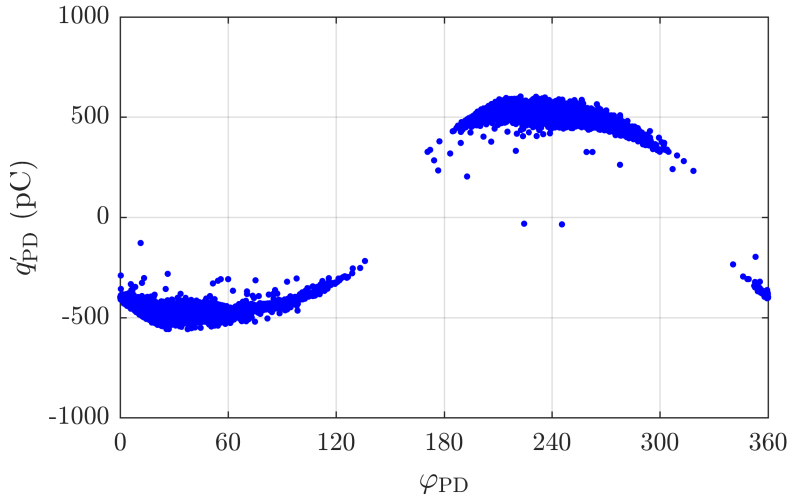

(a)

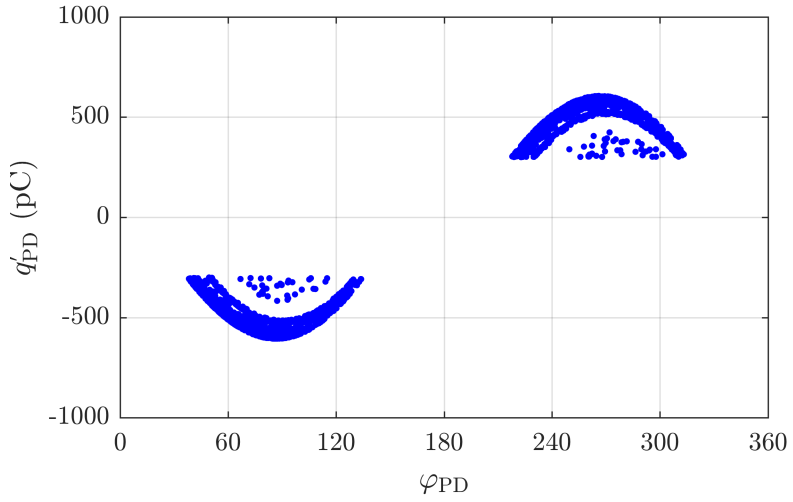

(b)

FIGURE 4.12: PRPD patterns at stage 3 of ageing: (a) experiment and (b) simulation.

Quantity	**Experiment**	**Simulation**
PDs per AC cycle	1.2	1.1
Mean q'_{PD} (pC)	479	475
Min q'_{PD} (pC)	32	300
Max q'_{PD} (pC)	603	606

TABLE 4.9: Statistical Quantities of Sustained PD Activity in a Spherical Void at Stage 3

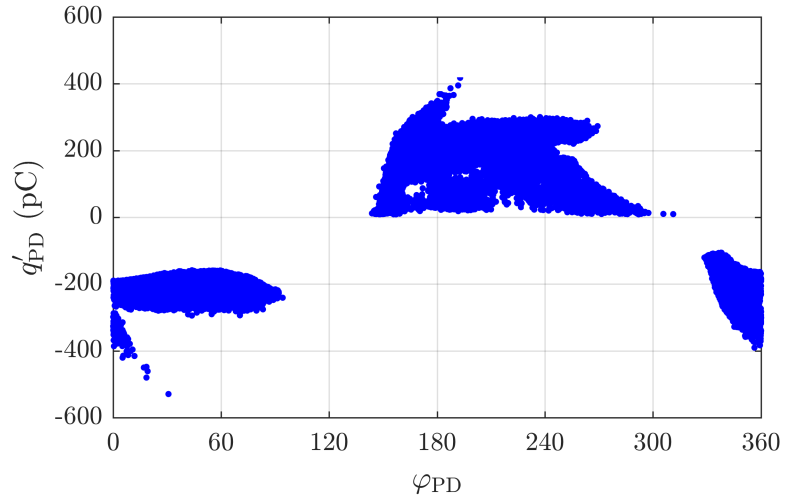

(a)

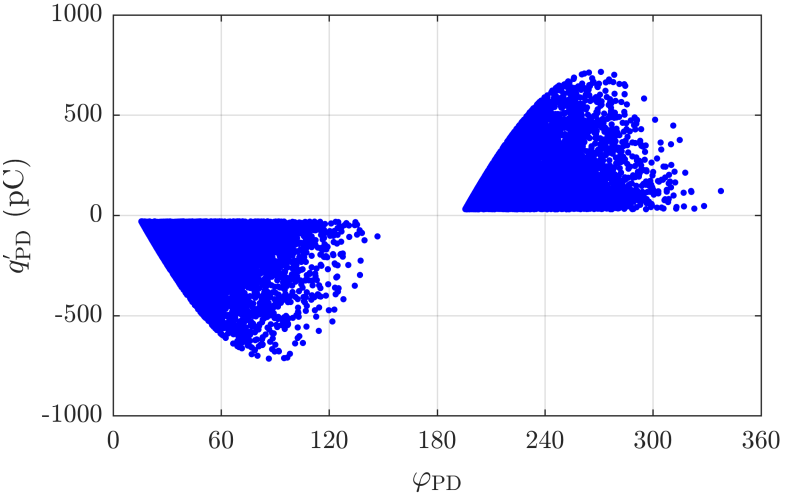

(b)

FIGURE 4.13: PRPD patterns at stage 4 of ageing: (a) experiment and (b) simulation.

Quantity	**Experiment**	**Simulation**
PDs per AC cycle	6.4	6.5
Mean q'_{PD} (pC)	205	180
Min q'_{PD} (pC)	9	30
Max q'_{PD} (pC)	529	716

TABLE 4.10: Statistical Quantities of Sustained PD Activity in a Spherical Void at Stage 4

The results show that the model can only simulate PD activity which is approximately

similar to the experimental data sets. In order to understand this discrepancy, it is necessary to realise that the following assumptions are implicit in this work:

1. The model geometry remains unchanged at all stages.
2. There is only a single source of PD at all stages.

These assumptions are necessary from the perspective of model simplicity. Furthermore, introducing changes to the model geometry or adding another PD source would require additional assumptions which would have limited justification while increasing model complexity. However, this does not imply that the assumptions are valid. It is quite plausible that by-products produced on the void surface, such as oxalic acid crystals in Low Density Polyethylene (LDPE) [20], may create locations of field enhancement and become additional PD sources. There may potentially be additional issues in the experimental arrangement, for example the void may not be approximately spherical, and as was noted in the previous section, deformation of the surface can significantly impact PD activity. Accepting the limitations of the model the following tentative conclusions that can be made, by considering the free parameters in Table 4.6, are:

- Sustained PD activity will lower the inception electric field of the void. This may be due to a change in the chemical composition of the gas inside the void.
- The charge detrapping processes are significantly altered by PD activity due to the formation of by-products at the void surface.
- Decay of charge on the void surface seems to play a more significant role as the dielectric surface is damaged, potentially due to increases in the surface conductivity of the void boundary.

4.11 Conclusion

In this Chapter the model proposed in Chapter 3 has been validated against experimental data. The model was then used to provide insight into the potential impact of void deformation on PD activity. PD activity is shown to highly dependent on void deformation, with PDs per cycle and maximum PD magnitude both increasing with the deformation radius R_{d}. An investigation into the evolution of PRPD patterns due to sustained PD activity was also undertaken. This work demonstrated the complexity of certain PD systems, which may violate the simplifying assumptions necessary for modelling. Additionally, it should be noted that due to their simplicity, there is a limited amount of insight that can be determined from hypothetical scenarios investigated using PD models. Models cannot, at present, be used to investigate the potential PD activity from an experiment a priori. Instead they are used to provide insight into experimental

data by fitting free parameters such that the simulated discharge activity of the experiment matches the model. In the next chapter the model will be used in a similar manner to investigate a more complex PD experiment in a three phase cable joint.

Chapter 5

Modelling Partial Discharges in Three Phase Cable Joints

In this chapter the PD model was used to investigate discharge activity for more complex experiments than those considered in Chapter 4. Three-phase cable experiments provide an appropriate middle ground between the highly controlled parallel plate experiments investigated in the previous chapter, and the complex PD data sets taken from on-site measurements [3]. In this chapter PD activity from a single three-phase cable experiment is investigated, the work in this chapter has been presented by the author in [13] and improves on earlier work in [88]. Following this the model was used to consider hypothetical PD activity from a spherical air filled void in the paper region surrounding one of the phase conductors, and how PD activity will be influenced by void location. This work is presented in [14].

5.1 Introduction

A range of PD experiments that seek to mimic systems indicative of conditions "in the field" were undertaken by Jack Hunter at University of Southampton as part of his PhD [76]. In particular a range of experiments were performed to investigate PD activity from paper insulated lead covered (PILC) three-phase cable joints [89, 90]. PILC cable was investigated as it forms a significant part of the London distribution network, and because it was installed in the 1960's-1970's it is reaching the end of its predicted operational lifespan [76]. Cable joints were investigated as during construction they are fabricated on site, often in challenging conditions, so may be more prone to flaws from human error [76].

5.2 Straight Joint Construction

To fabricate the sample a straight joint was introduced into a three-phase PILC cable using the same methods employed on-site. This type of joint was constructed as they are the most commonly used joint type for three-phase PILC 11kV cable circuits [76]. The first step in constructing a straight lead joint is to cut away the cable oversheath and armour to the required length. The layer of bitumen-impregnated Hessian beneath is removed with a knife and the Bitumen is then cleaned with a cloth and some solvent. At each end of exposed lead the armour wires are bonded to the sheath by soldering with a tin and lead alloy, which is then wrapped with electrical tape which acts as a layer of mechanical protection. The rest of the lead sheath is then removed to expose the paper belt which is discarded to allow access to the paper insulated phase conductors and bedding. At the location where the phase conductors overlap the paper insulation is removed to provide access to the copper conductors. The remaining paper insulation is covered in cotton paper saturated in oil to protect the paper insulation during the ferrule soldering process. Ferrules are used to connect the copper phases and then molten solder is repeatedly applied to create a solid connection, this technique is known as "sweating", see Figure 5.1. Once the solder has cooled, the ferrules are sanded to remove spikes in the solder which could enhance the electric field leading to increased electrical stress on the insulation. The cotton paper is then removed and oil impregnated Crêpe paper is wound several times around each phase to replace the previously removed insulation. A lead capsule is then fabricated to surround the joint and soldered to the lead sheath of the cable at each end. The lead capsule has two holes cut into the top, hot liquid bitumen is then poured through one of these holes with the other left free to allow air out. After the bitumen has cooled the holes are sealed, which completes the joint construction. It should be realised that this a brief summary of the joint construction, for a more detailed description the reader is referred to the source material [76].

FIGURE 5.1: Photograph showing application of molten solder to the ferrules, used with permission from [76].

5.3 Three Phase Cable Joint Partial Discharge Experiments

To narrow the scope measurement data from two experiments from [76] will be discussed in this report. In the first, a spike was placed on the ferrule of phase two during joint construction. It was found that PD activity from this system was permissible to modelling, the model and results are presented in Section 5.6. For the second experiment, a large air void was created in the joint by not completely filling the lead capsule with bitumen. The PD activity measured from this experiment was exceptionally noisy, and as such it could not be investigated using a PD model. This experiment is included in this report because it displays the complexity of PD activity that may be observed in on-site conditions and demonstrates the current limitations of PD modelling capabilities.

5.3.1 Spike on Ferrule

A sample was designed to replicate the effects of poor solder smoothing on the ferrule during joint construction. During the fabrication of the joint used in the experiment, a metal spike was created by applying solder to a wire which was attached to the ferrule on phase two in the direction of phase one. The spike tore through the innermost layers of Crêpe paper when it was wrapped around the ferrule, but was fully surrounded by paper when the insulation application was complete. Due to the time and cost constraints of the experiment, the spike is 14 mm in length so that PD activity occurs as soon as the experiment begins [76]. The spike defect is therefore more extreme than real world cases, but does not cause sufficient damage to cause an immediate breakdown. PD activity is measured on each phase using Omicron's Mtronix MPD600 PD measurement equipment. The input unit from the measuring equipment was connected in series with 1 nF blocking capacitor on each cable phase. The entire experiment was performed at rated volts. Initially the conductor temperature of the joint was held at 16 °C, and no PD activity other than background noise from cable terminations was measured [90]. However, when then the conductor temperature was raised to 65 °C PD activity was immediately observed, with PDs from the spike recording significantly higher magnitudes than the background noise, see Figure 5.2. As the cable sample cooled PD measurements where performed. Two PD data sets, in the following called data set 1 and data set 2, were collected over 19.8 s and 6.4 s respectively are used to provide validation for the modelling work. Both data sets were taken from phase two when the conductor temperature was 56 °C. The conductor temperature was determined by measuring the surface temperature of the joint and using thermal calibration data [90]. In both data sets PD activity from the spike occurs over a narrow range of phase angle, approximately 85° to 165°, with a peak apparent charge of 2.38 nC and an average of 1.2 PDs per cycle.

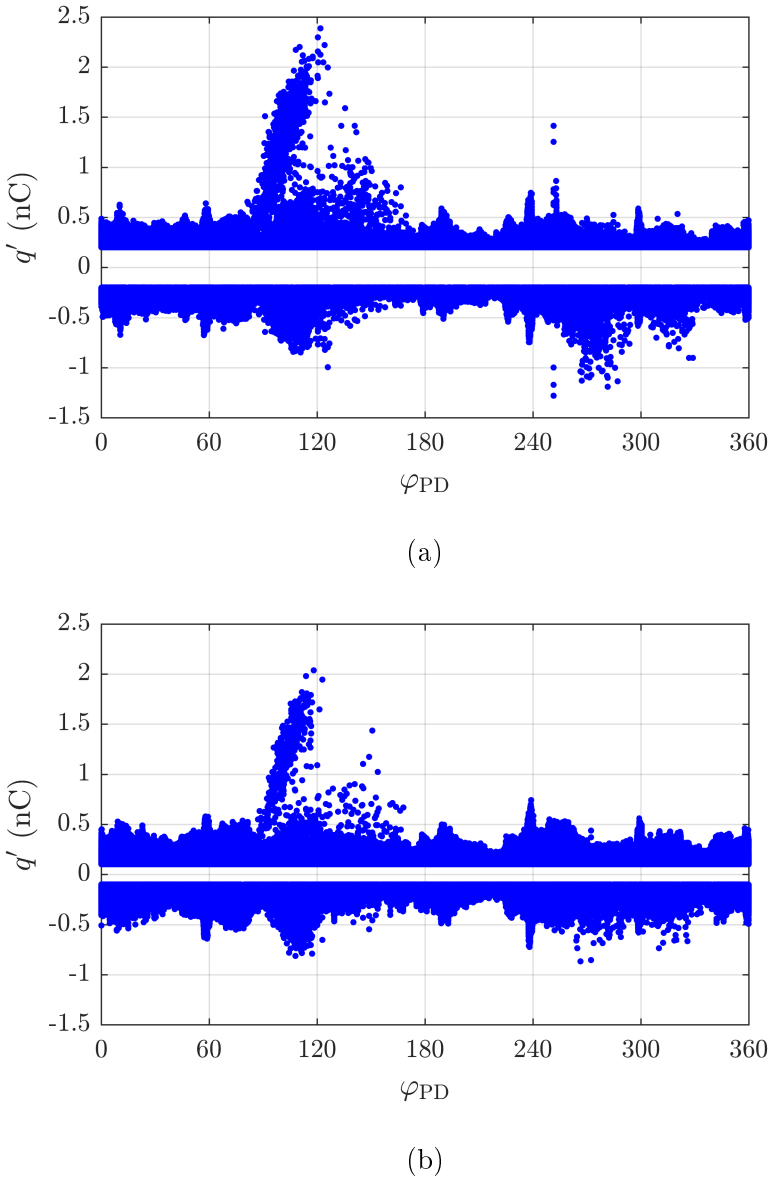

FIGURE 5.2: Figure showing PRPD plots for: (a) data set 1 and (b) data set 2.

5.3.2 Void on Top

A void was created in the joint by only partially filling the lead capsule with bitumen. The capsule was then sealed, and joint construction was finished as standard. The orientation of the capsule meant that a large air void was created in the region of the joint surrounding phase 3. Forensic investigation after the experiment revealed that the void was approximately 30 mm at its widest point, between the paper surrounding phase 3 and the capsule, and very approximately, 200 mm in the axial direction. As with the previous experiment, a large amount of background noise was observed at lower temperatures. When the sample temperature was increased above 40 °C this noise was

somewhat suppressed, and complex PRPD patterns were observed, an example is shown in Figure 5.3.

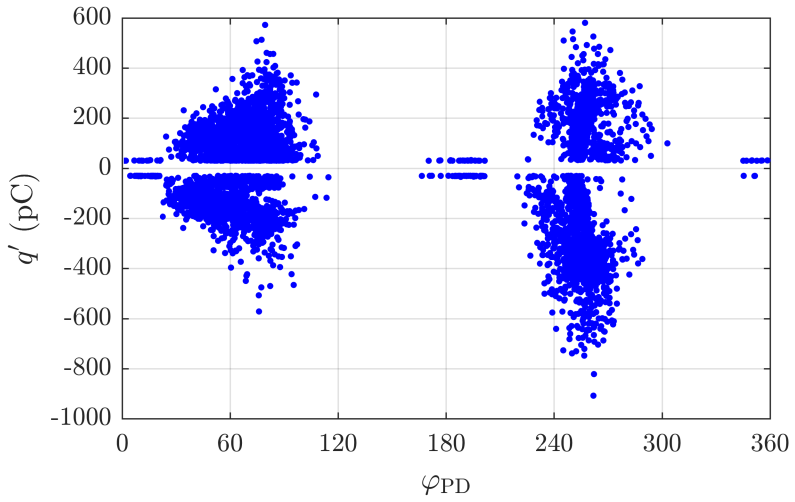

FIGURE 5.3: Figure showing PRPD plot for Void on Top experiment with joint surface temperature at 50 °C.

Due to the large size of the joint a large number of independent discharge channels are possible. These may have a strong influence on each other, and their location within this joint cannot be reliably estimated. Therefore, a simple model of PD activity would have to make such a large number of assumptions with respect to the location of PDs, and their surface charge density distributions, that it would be unable to give any meaningful insight.

5.4 Model Geometry

To find the electric field the electrostatic equation must be solved within the insulation material. The physical boundaries of the computational domain are the cable sheath and the three conductor phases. Each of these phases is surrounded by Crêpe paper, it will be assumed that both the phase conductor and the Crêpe paper are cylindrical. The three phase joint geometry used in all models is shown in Figure 5.4. There are therefore 4 parameters required to specify the three phase joint geometry: the radius of the joint R_{joint}, the distance of the phase conductors from the joint centre D_{phase}, the radius of the conductors from the joint centre R_{phase}.

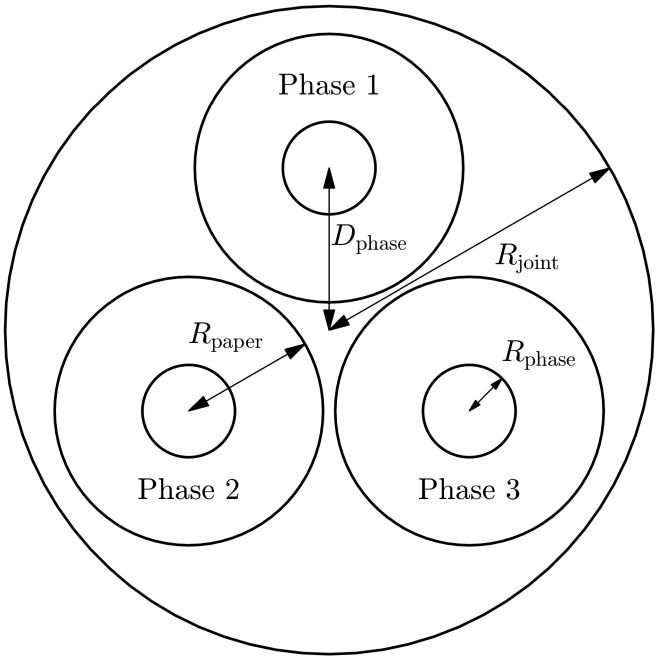

(a)

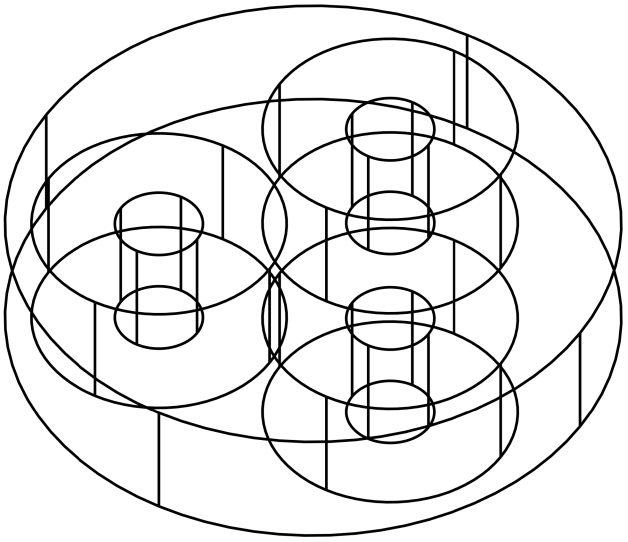

(b)

FIGURE 5.4: Figure showing the three phase cable joint model geometry: (a) labelled cross section and (b) isometric view of the three dimensional geometry.

Due to the fully three-dimensional nature of the defects present in these geometries, which are in the scale of millimetres, the joint geometry extends 3 cm in the axial direction with the defect centred in the central slice. The value of 3 cm was obtained by finding the distance away from the defect at which the electric field approached the applied field without the defect. It should be noted that over the entire length of the joint the cross section does in reality change. However, taking this into account would greatly increase the computational cost of the model, and is not thought to significantly impact the results presented here.

Parameter	**Value**
D_{phase}	35 mm
R_{joint}	70 mm
R_{phase}	8 mm
R_{paper}	28 mm

TABLE 5.1: Geometry Parameters for Three Phase Cable Joint

5.5 Electric Field

The electric field is found by solving the electrostatic Poisson equation, (3.1), with $\varepsilon_r = \varepsilon_{r\,\text{p}} = 3.6$ in the paper, $\varepsilon_r = \varepsilon_{r\,\text{o}} = 2.7$ in the oil and $\varepsilon_r = \varepsilon_{r\,\text{v}} = 1$ inside the void. The boundary conditions are set to be

$$V(\vec{x}, t; U_0, \omega) \begin{cases} 0 & \text{at joint sheath} \\ U_0 \sin(\omega t) & \text{at phase 1} \\ U_0 \sin(\omega t + 2\pi/3) & \text{at phase 2} \\ U_0 \sin(\omega t + 4\pi/3) & \text{at phase 3} \end{cases} \tag{5.1}$$

where $U_0 = \frac{22}{\sqrt{6}}$ kV and $\omega = 100\pi$, and as the cable joint is at rated volts with a 50 Hz supply. At the axial boundaries of the domain the following boundary condition is applied

$$\varepsilon_0 \varepsilon_r \vec{E}(\vec{x}, t) \cdot \vec{e}_z = 0, \tag{5.2}$$

where the z axis is orientated in the axial direction of the cable joint. (5.2) is used because far from the void the electric field approaches the applied field solution for a three-phase cable joint without a defect. The parameters used to calculated the electric field are provided in Table (5.2).

Parameter	Value
U_0	$\frac{22}{\sqrt{6}}$ kV
ω	100π
$\varepsilon_{r\ \mathrm{p}}$	3.6
$\varepsilon_{r\ \mathrm{o}}$	2.7
$\varepsilon_{r\ \mathrm{v}}$	1

TABLE 5.2: Electric Field Parameters for Three Phase Cable Joint

5.6 Modelling Partial Discharge Activity from Spike on Ferrule Experiment

The fundamental simplification used in the model is that the measured discharges are propagating in a spherical void at the tip of the spike. This is because the ferrule is surrounded by oil impregnated Crêpe paper, which has a high electrical breakdown strength, so it is unlikely that the discharges are propagating through the paper. A more plausible explanation that air was trapped around the spike due to the deformation of the paper layers by the spike. The tight wrapping of consecutive layers of paper around the spike would then force trapped air to spike tip. As the Crêpe paper is surrounded by oil at high pressure it is reasonable to suppose that the void has deformed to be approximately spherical. The spike is considered as a conical frustum and a sphere, with the sphere placed such that the spike surface is smooth, see Figure 5.6. The region of the spike surface created by this sphere is hereafter referred to as the spike tip. The base of the frustum is placed such that the entire bottom circle of the frustum is just inside phase 2. The void is assumed to be spherical, with the same origin as the sphere used to define the spike tip. The domain is truncated in the axial direction of the cable joint, as the void is the region of interest for PD modelling. There are therefore four geometry parameters used to define the spike and void: the length of the spike L_{spike}, the top radius of spike conical frustum $R_{\mathrm{spike\ top}}$, the bottom radius of spike conical frustum $R_{\mathrm{spike\ bottom}}$ and the radius of the void R_{v}. All these parameters can be set by the known conditions of the experiment except the void radius R_{v}, which will be adjusted to fit the data. A plot of the geometry with geometry parameters is shown in Figure 5.5, geometry parameter values are shown in Table 5.3.

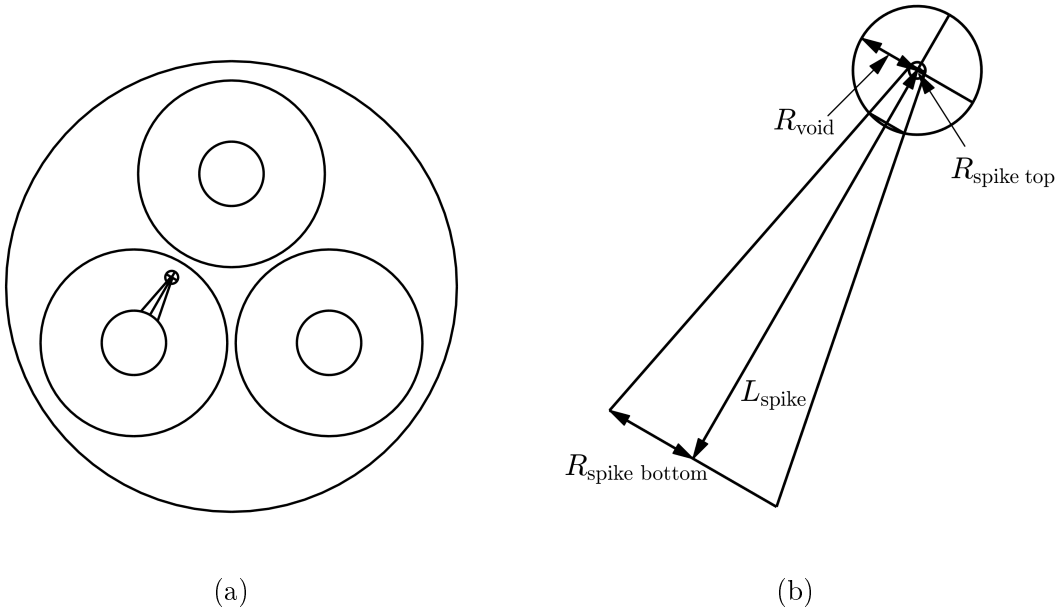

(a) (b)

FIGURE 5.5: Figure showing the model geometry for the spike on ferrule: (a) full geometry and (b) spike and void. It should be noted that the model geometry is fully three dimensional.

When calculating the electric field the spike is assumed to be at the same voltage as phase 2, and the surface charge from PD activity is deposited at the void boundary. The measuring electrode for this system, which is used to calculate the apparent charge, is phase 2.

5.6.1 Inception Process

From the reasoning in Section 3.2, the inception and generation points will coincide and will both be placed at the spike tip, see Figure 5.6. This means that $N_{\text{gen}} = N_{\text{inc}}$, $\vec{x}_{\text{gen}\,i} = \vec{x}_{\text{inc}\,i}$ and $A_{\text{gen}} = A_{\text{inc}}$ so that for a PD to occur the inception condition, (3.7), and free electron condition, (3.8), must both be met at the same point. Discharges will propagate in a direction orthogonal to the spike surface, so $\vec{e}_{\text{inc}}$ are outward facing normal unit vectors from the spike tip. It should be realised that as the spike surface is all at the same voltage, at any given point in time, the electric field is by definition normal to the surface, $\vec{e}_{\text{inc}}$ are included in the discussion for the sake of formality. As the spike tip is a section of a sphere, the inception and generation points will be distributed using a Fibonacci grid algorithm, see Appendix B. The inception points are only placed at the tip of the spike based on experimental images of discharges which only begin near the tip of the point electrodes [91, 92].

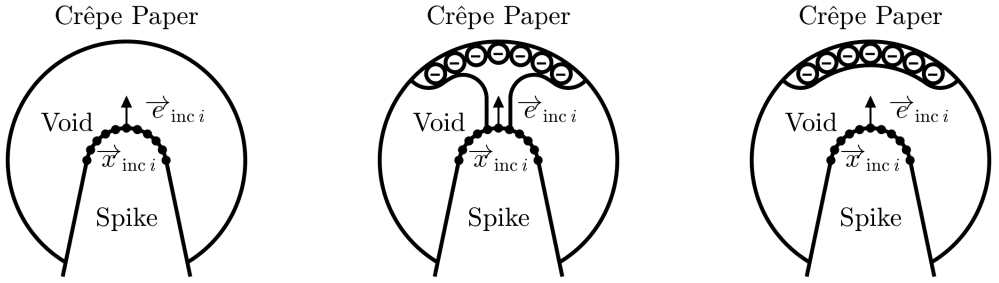

(a) (b) (c)

FIGURE 5.6: Figure showing qualitatively the effect of a single discharge in the void starting from an inception point in the centre of the spike tip: (a) before a discharge $|\vec{E}(x_{\text{inc}i})\cdot\vec{e}_{\text{inc}\,i}| > E_{\text{inc}}$, (b) during a discharge and (c) after a discharge $|\vec{E}(x_{\text{inc}\,i})\cdot\vec{e}_{\text{inc}\,i}| = E_{\text{res}}$. The solid dots represent inception points on the spike tip.

The inception and extinction condition require two parameters, the inception field E_{inc} and the extinction field E_{ext}. It will be shown in Section 5.6.5 that for this PD system both E_{inc} and E_{ext} can be set based on the void radius R_{v} and the experimental PD magnitudes.

5.6.2 Surface Charge Dynamics

The PD will deposit charge on the void surface until the extinction condition is met. Discharges propagate in the direction of the electric field during the negative half cycle, so the charge deposited on the void boundary will be negative, while positive charge will be deposited at the spike surface, as shown in Figure 5.6. Due to the higher surface conductivity of the spike compared to the Crêpe paper, it is assumed that only negative charge will be deposited at the void boundary with the Crêpe paper due to a discharge. It will also be assumed that the charge from a discharge spread across the entire void, while requiring that charge is at least a distance $\frac{\pi R_{\text{v}}}{20}$ from the surface of the spike. The functional form of $\sigma_{\text{PD}\,i}$ is then

$$\begin{aligned}\sigma_{\text{PD}\,i}(\theta,\phi,\Theta,\alpha_{\text{PD}\,i};R_{\text{v}},\theta_{\text{PD}},\phi_{\text{PD}},\eta_{\text{PD}},\lambda_{\text{PD}}) &= \ldots \\ \frac{\alpha_{\text{PD}\,i}}{1+\exp\left(\eta_{\text{PD}}\left(\Theta(\theta,\phi,\theta_{\text{PD}},\phi_{\text{PD}})\cdot R_{\text{v}}-\lambda_{\text{PD}}\right)\right)},&\end{aligned} \tag{5.3}$$

where θ and ϕ are azimuthal and polar angles respectively of a spherical polar coordinate system with origin at the void centre, Θ is the central angle, $\theta_{\text{PD}} = \pi/3$, $\phi_{\text{PD}} = \pi/2$, $\eta_{\text{PD}} = \frac{100}{\pi R_{\text{v}}}$, $\lambda_{\text{PD}} = (\phi_{\text{spike}} + \frac{9\pi}{20})R_{\text{v}}$ and ϕ_{spike} is the largest polar angle on the curve where the void surface and the spike surface intersect. The central angle is the smallest

angle between any two points on a sphere on a great circle that intersects both points, it is shown in Figure 5.7.

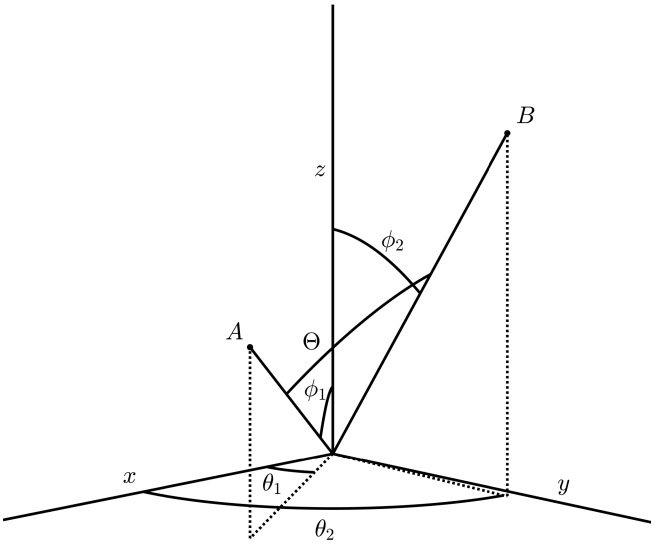

FIGURE 5.7: Figure showing spherical polar co-ordinates for two points, A and B, on a sphere centred at the origin. Θ is the central angle between them.

The physical justification for this choice of σ_{PD} is that the data sets to be modelled are taken after sustained discharge activity, which means that the surface conductivity of the void surface will be much greater than that of the virgin Crêpe paper. Therefore charge from a PD could feasibly spread across a large proportion of the boundary between the void with the Crêpe paper. Charge is prevented from moving too close to the spike, because the electric fields at the surface of the spike will oppose the negative charge from the PD during the negative half cycle, preventing charge spreading close to the spike. The consequence of this assumption is that discharges in the model have a relatively high magnitude, because the charge is distributed across most of the void surface, and a low frequency, because a discharge at any inception point causes a reduction in the electric field at all inception points. This PD behaviour is also observed in the experimental data, where high magnitude PDs, of the order nanocoloumbs, are observed with an average of only 1.2 PDs per AC cycle.

Finally, for PDs to only occur within one half cycle a decay of the deposited charge must occur. If a decay does not occur after a very small number of discharges, the electric field from the deposited charge will oppose the applied electric field such that the inception condition is no longer met at any inception point and discharge activity would cease after a few PDs. (3.12) must therefore be used, with τ_σ as a free parameter set such that the model results match those of experiment. It is possible that PDs from the spike are

occurring in the other half cycle, but as they cannot be distinguished from the PRPD pattern, (5.2), it was decided to simply introduce a decay of the surface charge.

5.6.3 Electron Generation

PDs are only observed in the negative half cycle, resulting in PDs with a positive apparent charge. This is somewhat perplexing, as discharges from a needle electrode would produce discharges in both positive and negative half cycles [93] and the spike is essentially an analog of it. It is possible that discharge are occurring in the positive half cycle, but they are lost in the noisy data, as was previously mentioned. However, it would be expected that discharges in the positive half cycle, with a negative apparent charge, would lead to higher magnitude PDs [93]. Therefore if PDs were only detectable in one half cycle, which is the case here, it is expected that they would have a negative apparent charge. It is unfortunately possible that an inversion of voltage and PD apparent charge polarity has occurred in the data sets used in this analysis. It should be noted that due to the simplicity of the model, which neglects the plasma dynamics of the discharge, a change in polarity in the data would simply result in appropriate polarity changes throughout the model, and would not negate any of the presented analysis. In order to take into account this dependence of PD activity on voltage polarity, the electron generation rate, (3.18), will be set to zero in the positive half cycle. Using the values shown in Table 5.3 the surface capable of generating PDs has an area $A_{\text{gen}} = 0.32$ mm^2. The free parameter c_{e} in (3.18) will be adjusted such that the simulation matches experiment.

5.6.4 Measurable Quantities of PD

The measuring electrode used in the experiment was phase two, so to determine the apparent charge from PDs in the model the integral in (3.20) is evaluated over a surface S comprising of phase two and the spike. The phase angle of PD is evaluated using (3.19).

5.6.5 Parameters

The governing equations and assumptions of the model in this PD system have now been introduced, it remains to choose the free parameters appropriately so that the model results match those of the experiment. The model has 5 free parameters: R_{v}, E_{inc}, E_{ext}, τ_σ and c_e. However, it is possible to reduce this number by setting E_{inc} and E_{ext}based on the void radius R_{v} and the experimental PD magnitudes. This reduces the number of free parameters to 3, which is comparable with existing PD models in the literature [8, 31, 44, 45]. λ_{PD} and η_{PD} are not regarded as free parameters as they are simply set so that the surface charge covers most of the void for a given R_{v}.

To determine R_v the following observations were made. Firstly, PDs only occur in a single half cycle and deploy charge to oppose the electric field that initiated them. Therefore after the first PD for any given inception point i

$$\left|\vec{E}(\vec{x}_{\mathrm{gen}\,i}, t)\cdot\vec{e}_{\mathrm{inc}}(\vec{x}_{\mathrm{inc}\,i})\right| < \left|\vec{E}_0(\vec{x}_{\mathrm{gen}\,i}, t)\cdot\vec{e}_{\mathrm{inc}}(\vec{x}_{\mathrm{inc}\,i})\right|. \tag{5.4}$$

The second observation is that the model is seeking to replicate a system where PDs occur relatively infrequently, with an average of 1.2 PDs per AC cycle, and that between PDs charge decays (3.12). This means that $\vec{E} \approx \vec{E}_0$ when the time between PDs is sufficiently large. The largest PD apparent charge possible in the model, $q'_{\mathrm{PD\ max}}$ will be approximately

$$q'_{\mathrm{PD\ max}} = \max\begin{pmatrix} -c_{q'\,1}\left(\vec{E}_0(\vec{x}_{\mathrm{inc}\,1}, t_{\mathrm{AC}\,1})\cdot\vec{e}_{\mathrm{inc}}(\vec{x}_{\mathrm{inc}\,1}) - E_{\mathrm{res}}\right) \\ \vdots \\ -c_{q'\,i}\left(\vec{E}_0(\vec{x}_{\mathrm{inc}\,i}, t_{\mathrm{AC}\,j})\cdot\vec{e}_{\mathrm{inc}}(\vec{x}_{\mathrm{inc}\,i}) - E_{\mathrm{res}}\right) \\ \vdots \\ -c_{q'\,N_{\mathrm{inc}}}\left(\vec{E}_0(\vec{x}_{\mathrm{inc}\,N_{\mathrm{inc}}}, t_{\mathrm{AC}\,N_{\mathrm{inc}}})\cdot\vec{e}_{\mathrm{inc}}(\vec{x}_{\mathrm{inc}\,N_{\mathrm{inc}}}) - E_{\mathrm{res}}\right) \end{pmatrix} \tag{5.5}$$

where $t_{\mathrm{AC}\,i}$ is the time in the AC cycle where $\vec{E}_0(\vec{x}_{\mathrm{inc}\,i}, t)\cdot\vec{e}_{\mathrm{inc}}(\vec{x}_{\mathrm{inc}\,i})$ takes it highest value. (5.5) follows from the definition of $c_{q'}$, using the fact that only a single distribution of charge is considered in this model. In PRPD pattern from the experiment, the "ear" structure does not have a peak, so a PD with the maximum possible magnitude does not actually occur in the system. Extrapolating from the experimental data $q'_{\mathrm{PD\ max}} \approx$ 2.8 nC. By considering the geometry it is clear that $\vec{E}_0$ at the inception points is not heavily dependent on the void radius, and is more strongly influenced by the geometry of the spike tip. However, c_q will increase as the void radius gets larger as larger voids allow more charge to be deposited, this has been verified by experimental measurements [52].

The fitting can then be performed by finding c_q and $\vec{E}_0$ for a small void radius, starting at $R_\mathrm{v} = 0.5$ mm, and calculating the appropriate E_{ext} from (5.5) such that $q'_{\mathrm{PD\ max}} \approx$ 2.8 nC. If E_{ext} be negative to give a sufficiently high $q'_{\mathrm{PD\ max}}$ it is clearly unphysical and the void is too small. E_{ext} is then recalculated for a new larger void radius, with the void radius increasing in increments of 0.25 mm. The process is repeated until the extinction field required to satisfy (5.5) is positive and of sufficient magnitude, approximately 1 kV mm^{-1}. Once E_{ext} has been found E_{inc} can be determined through the minimum apparent charge, $q'_{\mathrm{PD\ min}}$, because

$$q'_{\text{PD min}} = \min \begin{pmatrix} -c_{q'\,1}\,(E_{\text{inc}} - E_{\text{res}}) \\ \vdots \\ -c_{q'\,i}\,(E_{\text{inc}} - E_{\text{res}}) \\ \vdots \\ -c_{q'\,N_{\text{inc}}}\,(E_{\text{inc}} - E_{\text{res}}) \end{pmatrix}, \tag{5.6}$$

from the experiment, $q'_{\text{PD min}} \approx 0.55$ nC.

Once the void radius has been set, the remaining parameters to fit are the time decay constant τ_σ and the electron generation parameter c_e. To do this a parameter sweep with different combinations of τ_σ and c_e was performed until a combination was found where the PRPD patterns of experiment and simulation were in close agreement. Agreement was determined by visual similarities in the PRPD structure, and by comparing statistical quantities including PDs per AC cycle, maximum and minimum PD magnitudes and the range of phase angle over which PD occurs. The values of the parameters used in the simulation are given in Table 5.3.

Parameter Group	**Parameter**	**Value**
Geometry	L_{spike}	14 mm
	$R_{\text{spike top}}$	0.25 mm
	$R_{\text{spike bottom}}$	2 mm
	R_{v} *	2 mm
Inception	E_{inc}	6.7 kV mm^{-1}
	E_{ext}	3.3 kV mm^{-1}
Surface Charge Dynamics	η_{PD}	$\frac{100}{\pi R_{\text{v}}}$
	λ_{PD}	$(\phi_{\text{spike}} + \frac{9\pi}{20})R_{\text{v}}$
	τ_σ *	15 ms
Electron Generation	c_e *	0.72 kV^{-3} mm^3

* Free parameter

TABLE 5.3: Model Parameter Values for PD due to Metallic Spike Defect

5.6.6 Results

Two different voltage boundary conditions were used in the model, (5.1) and the voltage waveform recorded in the experiment. The voltage waveform of the experiment represents a moderate deviation from a typical sine function which impacts PRPD patterns, see Figure 5.8. Since data set 1 was collected over 990 AC cycles as opposed to data set 2, which was collected over only 320 cycles, the model was fitted to data set 1, it should be noted that the model describes both data sets well with a single choice of parameters due to the similarity between the data sets.

Reasonable agreement was seen between PRPD patterns of experiment and simulation with both boundary conditions, with a comparable number of PDs per cycle and PD magnitudes. Slight discrepancies were observed in the shape of the "rabbit ear" PRPD pattern, with a more pronounced curvature in the model's "ears" compared to the experiment. There are also disparities in the phase magnitude in experiment and simulation. However, the model was in close agreement with the data in the number of PDs per cycle and the phase angle range. A full summary of results is given in Tables 5.4 and 5.5.

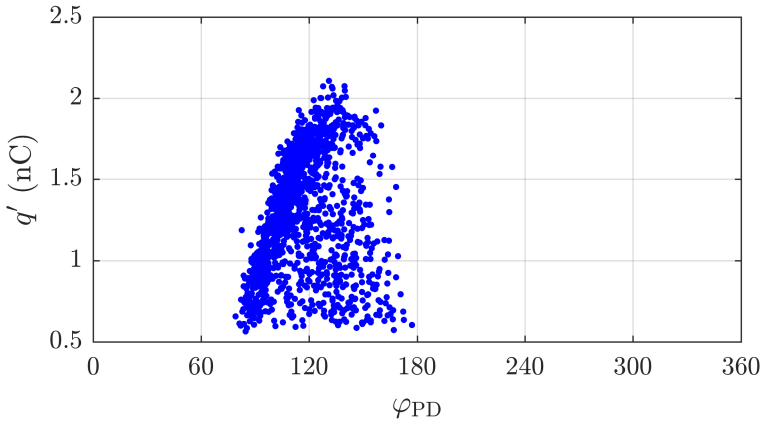

(a)

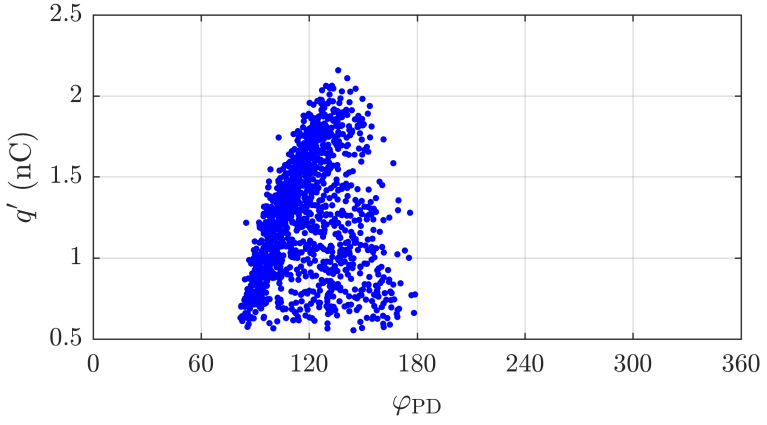

(b)

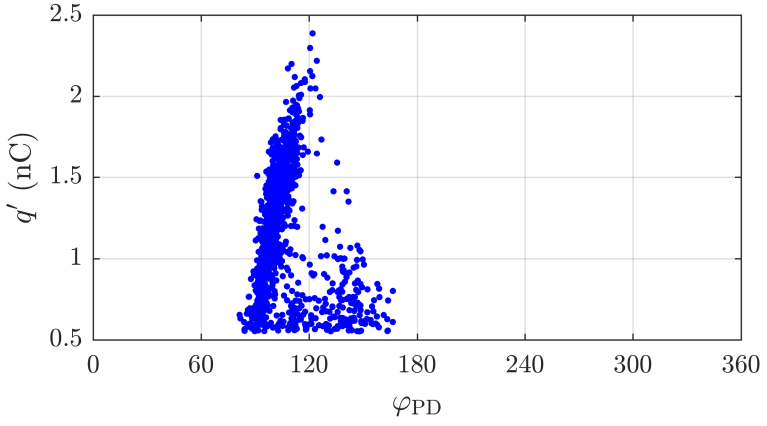

(c)

FIGURE 5.8: Figure showing PRPD patterns from the model and experiment: (a) model with sine wave boundary condition, (b) model with voltage waveform boundary condition, (c) experiment data set 1. All PRPD data is from 990 AC cycles.

	Data Set 1	**Data Set 2**
PDs per cycle	1.2	1.2
Maximum q'_{PD} (nC)	2.38	2.03
Minimum q'_{PD} (nC)	0.55	0.55
Mean q'_{PD} (nC)	1.16	1.18
Phase Angle Range (°)	85°	79.9°

TABLE 5.4: PD Data Experimental Results

	Sine Wave AC Cycle	**Experiment AC Cycle**
PDs per cycle	1.3	1.5
Maximum q'_{PD} (nC)	1.9	1.73
Minimum q'_{PD} (nC)	0.56	0.56
Mean q'_{PD} (nC)	1.08	0.92
Phase Angle Range (°)	92°	86°

TABLE 5.5: PD Data Model Results

In addition to modelling the experimental data, the model is used to investigate an alternative testing environment, see Figure 5.9. In many commercial tests, three-phase cable experiments are conducted with only a single energised phase. As the defect is located near phase 2, the model was run with only phase 2 energised, with all other phases set to ground. This produced markedly different results, with far fewer PDs and a significantly different PRPD pattern which was phase shifted by $\sim 15°$. The phase-shift is due to the fact the the electric field only depends on the phase angle of phase 2, when the cable is fully energised the other phases impact the electric field. The reduction in the number of PDs is caused by the reduced magnitude of the electric field, leading to fewer free electrons available for PD as a result of (3.18) and the fact that the field is lower than the inception field over a larger phase angle range. A summary of the results is provided in Table 5.6.

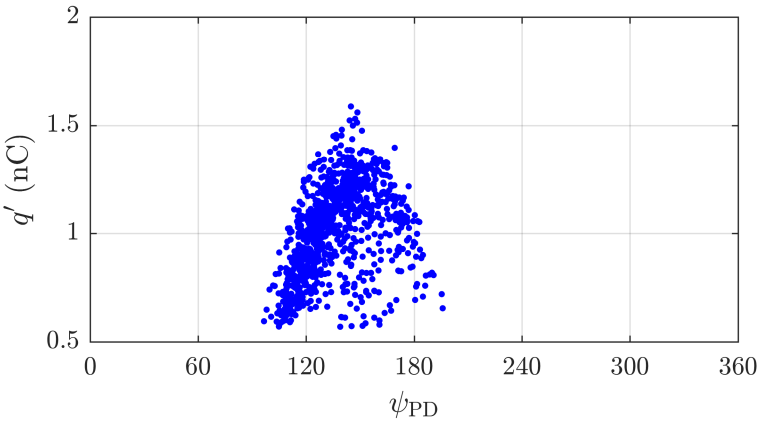

FIGURE 5.9: Figure showing PRPD pattern from the model with only phase 2 energised.

	Phase 2 Energised Only
PDs per cycle	1.1
Maximum q'_{PD} (nC)	1.35
Minimum q'_{PD} (nC)	0.56
Mean q'_{PD} (nC)	0.858
Phase Angle Range (°)	83°

TABLE 5.6: PD Data Phase 2 Energised Only Model Results

5.6.7 Discussion

The level of agreement between experiment and simulation justifies the assumptions and simplifications made in the model. It is an encouraging result that a PD model with relatively few free parameters was able to reproduce data from a three phase cable experiment at rated conditions. The model represents an improvement over an earlier model by the authors of the same experiment that required a larger number of free parameters to fit the data, including extra stochastic terms, and did not consider the defect geometry [88].

The free parameters used to describe the model are physically sensible, and have implications for the PD system. Firstly, the void is relatively large with a radius of 2 mm, suggesting that the presence of the spike has caused significant damage to the Crêpe paper to trap this volume of air close to phase 2. Of course, in reality it is unlikely the void is exactly spherical with this radius, however, it does imply that the defect at the spike tip is in reality likely to be similarly severe. It is also interesting that an empirical fit used for the electron generation rate of a needle-plane system could be successfully applied to a metallic spike under different conditions. It is likely that a better fit to the

experimental data could have been achieved if more parameters were used. However, due to the high level of uncertainty in the experimental data it was decided to obtain a reasonable fit using fewer free parameters and a more general model. An issue with introducing more free parameters is that it increasingly reduces the model to a curve-fitting exercise, which was not the aim of the research. Another interesting result from the study is the dependence of PD on the applied field. Typically in PD modeling a perfectly sinusoidal applied field is assumed. The model results reinforce the validity this assumption, at least for the case considered, with the measured waveform giving similar results to the sinusoidal waveform. There are still detectable differences between the sinusoidal and measured waveform boundary conditions which were identified by comparing a large number simulation runs. The most obvious of these is that measured waveform simulation has a phase angle distribution shifted to the left by an average of 3° compared to the phase angle distribution of the sinusoidal simulation. This was due to the different shape of the waveform, leading the inception field to be reached at lower phase angles. The model also showed significant differences between PRPD patterns for a single energised phase compared to a fully energized cable. The results from the simulation suggest that the applied voltage input should be closely monitored when testing PD activity in high voltage plant, and that PD measurements are taken under rated volts with the same phase energisation as operating conditions.

The experimental results show that PD activity is heavily dependent on temperature, with the results implying that PD testing of PILC cable sections for spike defects should be conducted at higher temperatures as it leads to a dramatic reduction in the background PD from cable terminations. A possible reason for this is that the PD from the cable terminations is caused by numerous gas filled voids formed in the heat shrink materials used to create the termination. As these voids are fixed in size, increasing the temperature will lead to an increase in pressure, subsequently increasing the inception and extinction electric fields, (4.10) and (4.11). This explains the reduction in PD magnitude and frequency from cable terminations.

Despite this success, there are discrepancies between the model and experiment. One of the possible explanations for this is that spike geometry used in the model represents a simplification of the more complex geometry present in the experiment, which has implications on the apparent charge magnitude as it is calculated through an integral whose domain includes the spike surface. An alternative spike geometry would also influence the form of the electric field, which has been already demonstrated to impact PD activity. Another simplification made in the model is that the surface charge distribution is independent of the location on the spike the discharges initiate from. Furthermore, variations in c_e and τ_σ may occur over the AC cycle. There are also uncertainties present in the measuring process, with a high level of background noise, discrimination of spike PD data is non-trivial, even at higher temperatures, and data assumed to originate from the spike may be contaminated with PD from the terminations. These problems are

compounded by cross-talk between phases and attenuation of the PD pulse, leading to a greater uncertainty in the measurement of the apparent charge. This contrasts with more controlled PD experiments between parallel plates, where cross-talk and attenuation is negligible as the void is typically close to the measuring electrode and surrounded by a homogeneous dielectric material.

Finally, it should also be noted that the model presented is only preliminary step in simulating on-site data, before this can be attempted there are several obstacles that must be overcome. An obvious difficulty is that the model required a known defect type, location and size, all of which may be unknowns in PD data taken on-site. There is also only a single known source of PD present in this experiment, whereas in the operational plant there can be many sources which may also be interacting.

5.7 Modelling Partial Discharge Activity from a Spherical Air Void in Paper

The applied electric field inside three phase cable is elliptical with the axes of the ellipse dependent on location within the cable [94]. It was proposed to see how the elliptical nature of the applied could impact PD activity using simulation. The joint geometry is identical to the joint described in Section 5.4 with a spherical air filled void placed in the paper region surrounding phase 1. Three different void locations are considered in this work. Void 1 is located in the middle of the paper layer surrounding the phase 1 conductor in the direction of phase 1 to phase 2. Void 2 is located close to the phase 1 conductor, in the direction of phase 1 to phase 3. Void 3 is located near the outer layer of paper of phase 1, close to centre of the joint. The joint geometry and the positions of all 3 voids is shown in Figure 5.10.

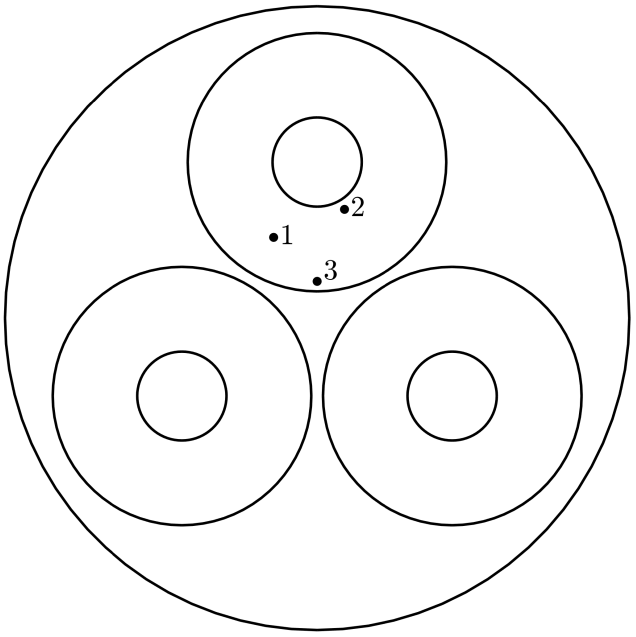

FIGURE 5.10: Cross section of the joint geometry with positions of the voids. The model geometry is fully three dimensional.

5.7.1 Inception Process

It will be assumed that discharges will propagate in the plane of joint, and will pass through the centre of the void. Therefore there is a single inception point located at the centre of the void. Taking a Cartesian coordinate system with origin at the void centre, and positive z axis in the axial direction of the joint,

$$\vec{x}_{\mathrm{inc}\,1} = (0, 0, 0). \tag{5.7}$$

The direction in which the discharges are propagating when they reach the inception point will depend on the direction the electric field is pointing at the inception point. In an axisymmetric parallel plate system the electric field in the centre of the void acts in a single direction. However, due to the elliptical nature of the applied field, the direction of the electric field at the inception point will depend on the phase angle in the AC cycle and the field from previous PDs. Therefore $\vec{e}_{\mathrm{inc}\,1}$ takes the form

$$\vec{e}_{\mathrm{inc}\,1}(t) = \left(\cos\left(\theta_E(\vec{x}_{\mathrm{inc}\,1}, t)\right), \sin\left(\theta_E(\vec{x}_{\mathrm{inc}\,1}, t),\right) 0\right), \tag{5.8}$$

where θ_E is the azimuthal angle of the field, which is explicitly

$$\theta_E(\vec{x}, t) = \arctan\left(E_y(\vec{x}, t)/E_x(\vec{x}, t)\right). \tag{5.9}$$

Due to the complexity of the problem it was assumed that the electron generation processes were also governed by the electric field in the centre of the void. The purpose of this investigation is to use the model to provide some basic insight into the dependency of PD activity with applied field structure, which can still be accomplished with this simplification. Assuming that the void is filled with air, it is possible to relate the inception and extinction field to the pressure p inside the void using (4.10) and (4.11).

5.7.2 Surface Charge Dynamics

It will be assumed that discharges occur along the equator of the void, and the charge spots are centered at antipodal points on the void surface. Discharges will propagate in the direction of the electric field at the inception point, which is in the centre of the void. Therefore in spherical polar coordinates with origin at the void centre the surface charge from the ith PD can be written as

$$\begin{aligned}\sigma_{\mathrm{PD}\,i}(\theta,\phi,\alpha_{\mathrm{PD}\,i};R_{\mathrm{v}},\eta_{\mathrm{PD}},\lambda_{\mathrm{PD}}) &= \\ \underbrace{\frac{\alpha_{\mathrm{PD}\,i}}{1+\exp\left(\eta_{\mathrm{PD}}\left(\Theta(\theta,\phi,\theta_{\mathrm{PD}\,i},\phi_{\mathrm{PD}})R_{\mathrm{v}}-\lambda_{\mathrm{PD}}\right)\right)}}_{\text{Positive Charge Spot}} &- \cdots \\ \underbrace{\frac{\alpha_{\mathrm{PD}\,i}}{1+\exp\left(\eta_{\mathrm{PD}}\left(\Theta(\theta,\phi,\theta_{\mathrm{PD}\,i}+\pi\ (\mathrm{mod}\ 2\pi),\pi-\phi_{\mathrm{PD}})R_{\mathrm{v}}-\lambda_{\mathrm{PD}}\right)\right)}}_{\text{Negative Charge Spot}}&,\end{aligned} \tag{5.10}$$

with $\eta_{\mathrm{PD}}=\frac{100}{\pi R_{\mathrm{v}}}$, $\lambda_{\mathrm{PD}}=\frac{\pi R_{\mathrm{v}}}{4}$, $\theta_{\mathrm{PD}\,i}=\theta_E(\vec{x}_{\mathrm{gen}\,1},t_{\mathrm{PD}\,i})$ and $\phi_{\mathrm{PD}}=\pi/2$. As this model is a hypothetical PD system, which is seeking to investigate the dependence of PD activity on the applied field, decay of charge between PD events will be neglected.

5.7.3 Electron Generation

The electron generation processes are the same as those in the spherical air filled void considered in Chapter 4. They are stated again here for completeness. For the conditions present in the void there are two possible electron generation processes; surface emission from the void boundary of charge from previous PD activity and ionisation of gas in the void through background radiation. Surface emission is the dominant process for the conditions present in this case, but it cannot generate electrons until after the first PD has occurred. As volume ionisation is a random process, it is sufficient for modelling purposes to let the first PD occur at a random point in the first AC cycle when the inception condition is met. After this electron generation is governed by surface emission through (3.13). It will be assumed that the decay of deep traps is negligible between PDs so only two free parameters need to be set, χ_{s} and $\tau_{\mathrm{dt\ s}}$.

5.7.4 Measurable Quantities of PD

To determine the apparent charge from PDs in the model the integral in (3.20) is evaluated over phase conductor 1. The phase angle of PD is evaluated using (3.19).

5.7.5 Parameters

Having defined the model, the final step is to set the parameters to physically sensible values. The parameter values used in the simulations are given in Table 5.7. The temperature is set to 43 °C to match the conditions of a three-phase cable experiment where PD was measured from an artificially created void in a PILC cable joint [76]. From the parameters, Φ, χ_s, $\tau_{d\ s}$ and p were all adjusted so that in the case of applied field that was close to linear, the classic "rabbit ear" PRPD pattern was observed. It should be noted that, due to the background noise and the inherent complexity of the system, voids in three phase cable joints are unlikely in reality to produce this pattern. The reason the model was set as such was that it allows insight into how a distinctive pattern will be influenced by the elliptical applied field, it should not be seen as fully representative of the real world system.

Parameter Group	Parameter	Value
Geometry	R_v	1 mm
Inception	p^*	2 kPa
Surface Charge Dynamics	η_{PD}	$\frac{100}{\pi R_v}$
	λ_{PD}	$\frac{\pi R_v}{4}$
Electron Generation	Φ^*	1.2 eV
	T	43 °C
	${\chi_s}^*$	0.99
	${\tau_{dt\ s}}^*$	2 ms

* Free parameter

TABLE 5.7: Parameter Values for PD Model of Voids in Paper

5.7.6 Results

The model introduced in Chapter 3 was implemented and run at each void location over 500 AC cycles. The applied field components over an AC cycle at the different void locations is shown in Figure 5.11. PD activity was shown to be highly dependent on void location with PDs per cycle, apparent charge magnitude and PRPD patterns, see Figure 5.12, all showing significant variance, see Table 5.8. Void locations 1 and 2 show typical rabbit ear PRPD patterns, with PDs occurring more frequently at location 2,

with higher apparent charges. At void location 3 PDs occur throughout the AC cycle, with "ear" like structures forming at $\sim 170°$ and $\sim 350°$. The maximum apparent charge magnitude at void location 2, close to the phase 1 conductor, were in the 10's of pC, a result which matches that of experiment [76].

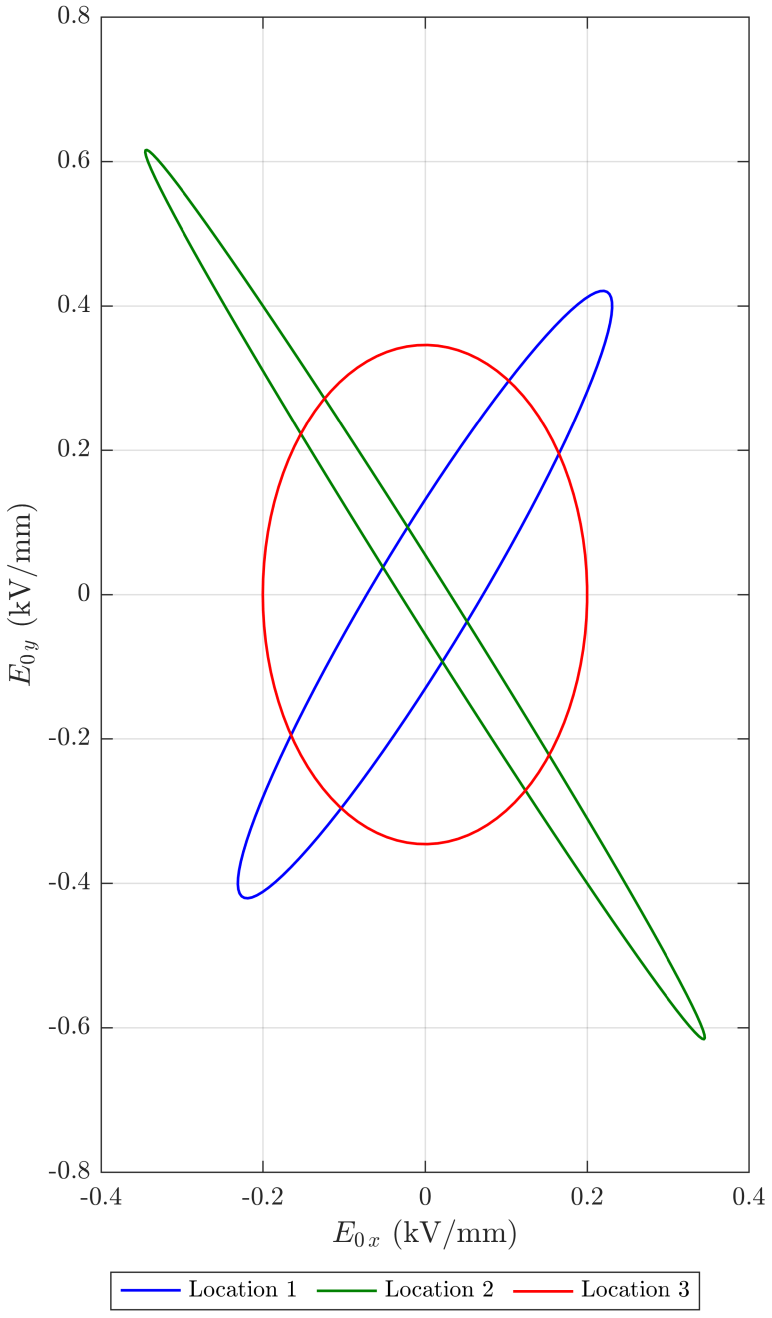

FIGURE 5.11: Components of the applied electric field over a single AC cycle at void locations: (a) 1, (b) 2 and (c) 3.

Quantity	**Location 1**	**Location 2**	**Location 3**
PDs per cycle	3.0	5.4	4.2
Mean $\lvert q'_{\mathrm{PD}} \rvert$	4.1	6.4	1.8
Max $\lvert q'_{\mathrm{PD}} \rvert$	10.3	24.3	5.1
Min $\lvert q'_{\mathrm{PD}} \rvert$	2.6	4.5	0

TABLE 5.8: Results for PD Model of Voids in Three Phase Cable Joint

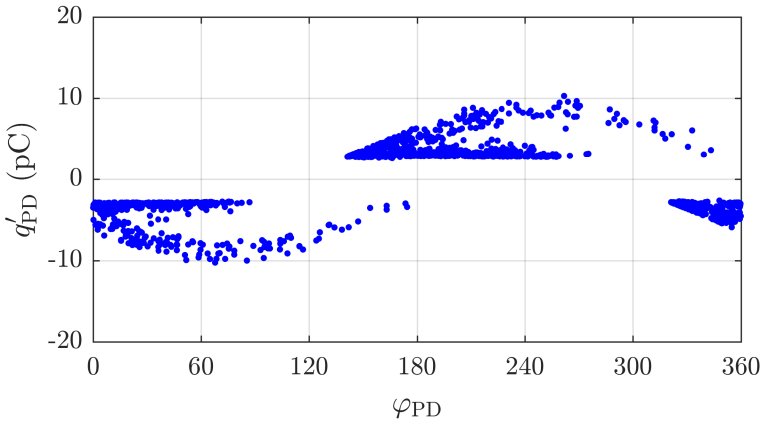

(a)

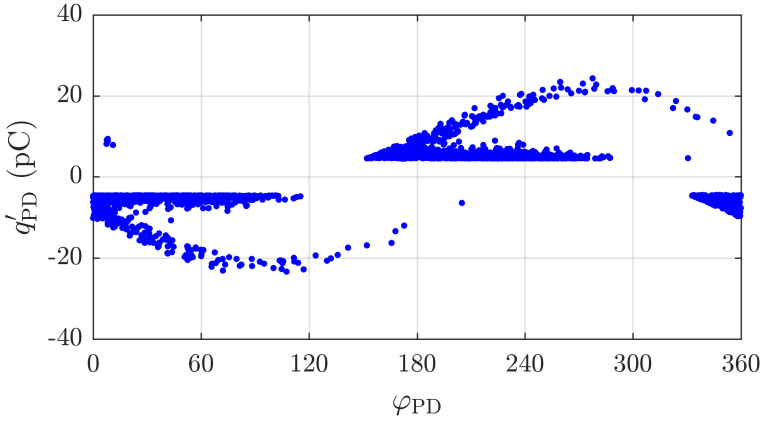

(b)

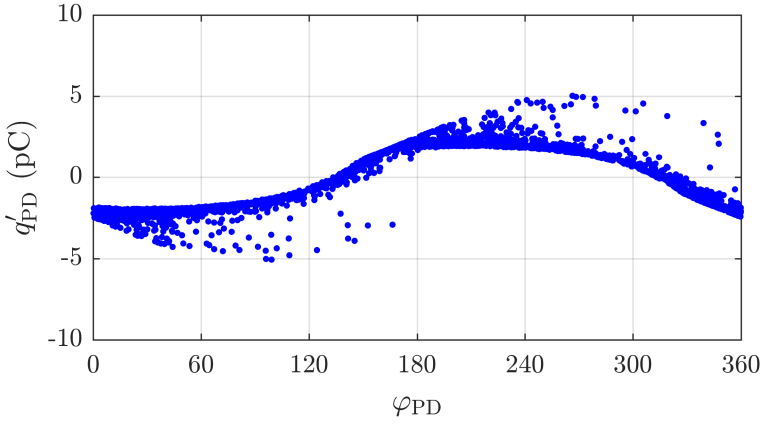

(c)

FIGURE 5.12: PRPD patterns at void locations: (a) 1, (b) 2 and (c) 3.

5.7.7 Discussion

The results from the model suggest that similar defects at different locations within the three-phase cable joint cross section will produce distinct PRPD patterns. This is due to the functional form of the applied field, the dependence of the apparent charge on the direction of the discharge, and the distance from the measuring electrode. However, it does also appear that certain features of PRPD patterns are robust to changes in the applied field, with "ear" structures observed in all PRPD patterns, see Figure 5.12, despite large variations in the applied field, see Figure 5.11.

The choice of parameters in Table 5.7 also allow some tentative conclusions to be made. Firstly, for PD to occur within air filled voids in three-phase cable the pressure must be significantly lower than atmospheric, otherwise the applied electric field never exceeds the inception field. Also, the work function of Crêpe paper at the void boundary is set to 1.2 eV, which is comparable with work functions of other insulators [17].

Following on from these results, there are alternative scenarios that would be worth considering in future work. One of the easiest changes would be to perform the simulation with ellipsoidal voids. This is a physically relevant scenario as voids are likely to become elongated in the direction of discharge activity over time, leading spherical voids to deform to ellipsoids. It would also be worth investigating how apparent charge varies with the measuring electrode as measurements of PD magnitude at all phases simultaneously are possible in three-phase cable experiments. Following on from this, PD activity from multiple voids could be investigated. This would greatly increase computational cost of the simulation, but would provide an insight into how distinct PD sources could interact in the joint.

Although the model displayed interesting results, there are limitations that must be overcome in future work. Firstly, dispersion and attenuation of the PD pulse are neglected, which means that the results are only applicable to short lengths of cable. Surface roughness at the void surface would also impact the electric field, altering the apparent magnitude. Quantifying these effects is non-trivial, and is still an active area of research. However, there are limitations present in the model that can be more easily rectified in future work. This include the assumption that PD activity is governed by the electric field in the centre of the void. In reality PDs can begin anywhere on the void boundary, and will be dependent on the surface charge and field strength at these points. Therefore in future work PDs will be allowed to occur at multiple points on the void surface, which is more physical and will likely lead to a greater level of stochasticity in the PD activity from the simulation.

5.8 Conclusion

In this work a PD model has been introduced that reproduces PD data from a three-phase cable experiment. The model requires only 3 free parameters, and was able to give reasonable agreement with experimental data, with good agreement in PDs per cycle, mean PD magnitude and phase angle range. Following this the impact of the hypothetical scenario of only have a single energised phase was investigated. Based on the model results and the experimental work it can be concluded that PD testing of three-phase cable joints should be performed at higher temperatures with all three-phases energised to be able to accurately identify defects and reproduce field conditions in the joint. The possible influence of the elliptical nature of the applied field on PD activity has also been investigated using the model.

Over the course of this work it became increasingly clear that, despite care being taking to reduce the free parameters, the PD model in its current form can only offer limited insight into PD activity. In particular the model requires great care to be taken when choosing free parameters, otherwise the simulated PD activity is far from physical, a trait shared with other PD models [4, 17, 44]. As an example, the work function of the surface Φ for epoxy resin takes a significantly different value in a PD model in the literature, 1.1 eV [9], compared to the value used in this work of 1.25 eV. This is simply a result of the parameter fitting, it offers no real insight into what the actual work function of the surface might be, in reality it is likely that the work function of an epoxy resin surface, before ageing, should be similar between experiments. This issue is compounded by the fact that in many cases there are numerous combinations of free parameters that could be chosen such that the model matches experiment. It should be noted that this does not completely undo the work presented in this thesis, as the range in which these free parameters can be chosen is often relatively narrow. However, these issues need to be acknowledged when using the present PD activity models in the literature.

In addition to this dependency on free parameters, it is also not entirely clear whether many of the fundamental assumptions used in the model are truly justified, despite being introduced in the literature. As a result of these significant shortcomings, it was decided to instead investigate PD using a drift diffusion plasma model. Due to its computational cost only single discharges can be considered, however, this can still provide insight into how valid the assumptions used in the PD activity models are. Moving on from this, it may then be a guide on how improvements to be made that may remove many of the free parameters and provide the basis for a more physical model of PD activity.

Chapter 6

A Plasma Model of Partial Discharge

From the work conducted so far in this thesis it is evident that PD activity models that use a simplified description of the discharge process can only offer limited physical insight into a PD system. It was therefore decided to implement a drift diffusion plasma model to test the assumptions used in PD models and provide an indication of possible improvements to future models of PD activity. The model used in this chapter is well established in the literature, for more information the reader is referred to a topical review [24]. This model makes use of equations previously introduced in this work, such as the electrostatic equation, (3.1). These are reproduced in full in this chapter, because a fundamentally new model is introduced.

6.1 Introduction

A plasma model that considers a large number of PDs is currently computationally prohibitive, so it is proposed in this work to use a simple drift diffusion model, that considers electrons and "abstract" positive and negative ions, to investigate the physics of the PD. The model considers PD inside an air filled spherical void, which has only recently begun to be investigated using plasma models [15, 61]. Obtained results have been analysed qualitatively against experimental measurements in the literature where appropriate, and their consequences for the understanding of the physical mechanisms of PD activity discussed. The PD system considered is a spherical void inside epoxy resin, because it is an arrangement which has received research attention [4, 8, 9]. Although not part of PD research explicitly, discharges within spherical bubbles in dielectric liquids are physically similar system, i.e. discharges within a gaseous sphere within a homogeneous dielectric material, which have been investigated using simulation [95, 96]. This simulation work has shown that when the physical conditions are similar to that of a PD system, these

discharges consisted of an electron avalanche transitioning into a positive streamer [97], in agreement with the work on dielectric barrier discharges. The plasma dynamics are distinct due to the containment of the discharge within the void limiting the spread of the plasma. In the research of discharges within bubbles, the emphasis has been on the initiation of the discharge and the plasma dynamics. The aim of this chapter is to improve the physical understanding of PD dynamics and to test some of the physical concepts that are employed when modelling PD in air-filled voids.

6.2 Physical Concepts

In this section the concepts that will be investigated in this work are outlined:

1. Plasma Dynamics - In earlier work the plasma dynamics of a PD in air was described as an electron avalanche transitioning into a positive streamer for a dielectric barrier discharge in a 3 mm air gap with an electric field slightly above the breakdown threshold of air [57]. Simulations of discharges within spherical air bubbles in dielectric liquids, which are indicative of PD systems containing spherical voids, has shown that the plasma dynamics consisted of an electron avalanche moving against the applied electric field transitioning into a positive streamer moving with the electric field [95]. Separate studies, at conditions that differ from a standard PD system, observed similar discharge dynamics [58, 98]. The earlier work of Niemeyer assumed that a PD consisted of a positive and negative streamer [17].

2. Inception and Residual Fields - Two widely used values in PD modelling are the inception and residual electric fields. For PD to occur the electric field in the void, typically the centre, must be at some inception value E_{inc}. For PD systems E_{inc} is typically set to

$$E_{\text{inc}} = (E/p)_{\text{cr}} p \left(1 + \frac{B}{(pl)^{1/2}}\right) \tag{6.1}$$

where $(E/p)_{\text{cr}} = 25.2$ V Pa^{-1} m^{-1} is the constant of proportionality between the critical electric field E_{cr} required to sustain the discharge and the gas pressure p, $B = 8.6$ Pa$^{1/2}$ m$^{1/2}$ and l is the length of the void in the direction of the discharge [9]. It should be noted that in practice $(E/p)_{\text{cr}}$ will be dependent on streamer polarity. After the discharge has taken place, it is then assumed that the electric field in the void is reduced to a residual value which is equal to field in the streamer channel, E_{ch}, and is proportional to E_{cr}

$$E_{\text{res}} = E_{\text{ch}} = \gamma E_{\text{cr}} \tag{6.2}$$

where $\gamma = 0.35$, the average of 0.2 and 0.5 for positive and negative streamers respectively [9]. It should be noted that despite their widespread usage in the literature, since they were proposed cited work of Niemeyer [9, 17], these equations

may not necessarily be applicable to PD systems. In the case of the inception equation the experimental data for the ionisation parameters is determined from breakdown in air gaps between metallic electrodes [41], whereas in PD systems the discharge region is frequently bounded by a solid dielectric material. For the residual field equation, it is not clear that the field in the streamer channel will be equivalent to the field after the discharge has ceased. Furthermore, the conclusion that the channel field is proportional to the critical field appears to determined from metallic needle-plane experiments, [99], which have a highly divergent applied field, and do not have solid dielectric regions, which may limit the applicability of the result to certain PD systems.

3. Surface Charge Distributions - It is commonly assumed that when the dielectric surfaces at each side of a discharge channel are symmetric, such as in spherical, cylindrical or ellipsoidal voids, the surface charge distribution at the dielectric surfaces are bipolar [4, 17, 39]. Earlier numerical studies and experimental work investigating PD in cylindrical voids suggest that the distribution is in fact not bipolar, [6, 57], and that the negative surface charge distribution has a greater spread due to the higher mobility of electrons compared to ions. Both of these studies have looked at PD for electric fields that just exceed the breakdown threshold. In previous models of PD activity it has been assumed that the PD surface charge is deposited directly over the surface charge of previous PDs [4]. However, it is likely that field due to the charge of previous PDs will influence the charge deployed by subsequent PDs.

4. Charge Recombination - In Niemeyer's seminal paper, [17], an order of magnitude time decay constant, τ_{rec}, was calculated for the rate of charge recombination in a given void after a discharge as follows

$$\tau_{\text{rec}} \sim \frac{l}{C_\mu (E/p)_{\text{cr}}} \frac{E_0}{E_{\text{inc}}}, \tag{6.3}$$

where l is the length scale of the void, C_μ is the quotient of ion mobility by gas pressure, p is the gas pressure and E_0 is the applied electric field magnitude. For most PD systems of interest τ is in the order of microseconds. As such the influence of the charge "left over" from previous PDs is assumed to be negligible by the time the next discharge occurs as the time delay between discharges is in the order of milliseconds.

6.3 Drift Diffusion Plasma Model

The concepts listed in Section 6.2 will be critically tested by a dynamic plasma model. In this section the governing equations and boundary conditions are provided along with

the model geometry under consideration. The model consists of three drift diffusion equations for three charged species, an electrostatic equation to determine the electric field and three Helmholtz equations to determine the photoionisation rate. The model is implemented in COMSOL Multiphysics, software which has been used throughout this thesis and has been used to model discharges in air previously in the literature [7, 53].

6.3.1 Geometry

Two model geometries are considered in this work. The first is axisymmetric, consisting of a spherical void with a radius, R_{v}, of 0.5 mm surrounded by epoxy resin between parallel plate electrodes. The motivation for this is that quasi-spherical voids often occur in epoxy resins in operating high voltage plant, due to errors in the curing process, which can facilitate PD activity. Furthermore the PD activity observed from this experimental arrangement is not significantly impacted by noise and as such a physical interpretation of discharge behaviour is possible [4]. The second geometry is one dimensional and consists of the symmetry axis of the axisymmetric model geometry. A one dimensional model is considered as it vastly reduces the computational cost and as such allows simulations to be run over longer time periods. For the arrangement present it is supposed that the physics of the one dimensional model is indicative of the physics in the two dimensional model. The justification for this is that the applied electric field close to the symmetry axis in the two dimensional model is approximately uniform and acts in a single direction. This would not be permissible in a arrangement with a more divergent electric field, such as a needle-plane electrode system. The model geometries are shown in Figure 6.1.

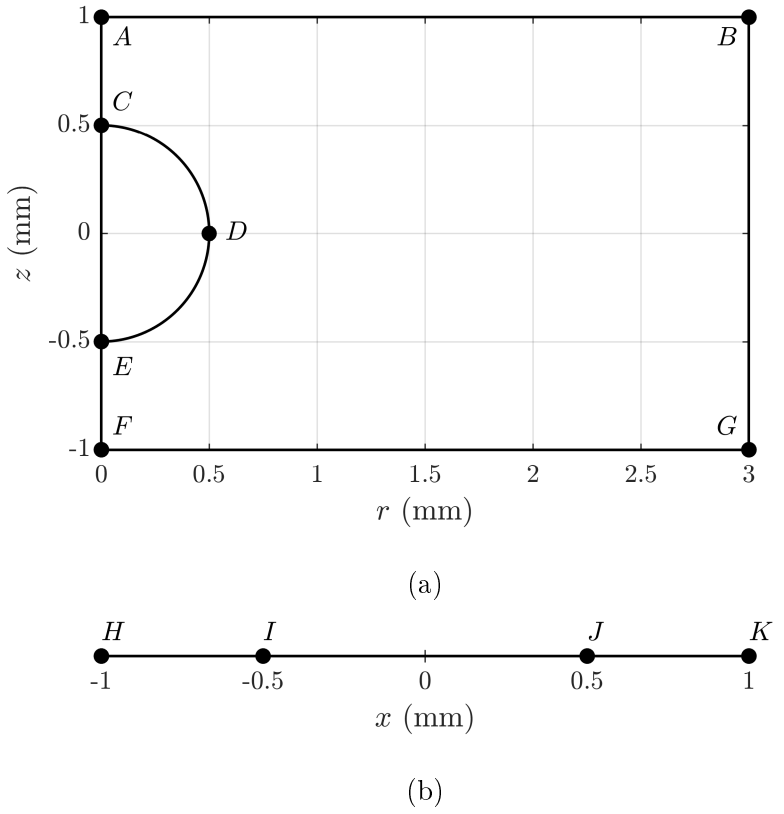

FIGURE 6.1: Model geometries with labelled vertices: (a) two dimensional axisymmetric and (b) one dimensional.

6.3.2 Governing Equations

The model solves drift diffusion equations for the number densities of electrons n_{e}, positive ions n_{p} and neutral ions n_{n}

$$\begin{aligned}
\frac{\partial n_{\mathrm{e}}}{\partial t} &= \alpha n_{\mathrm{e}} \left|\vec{W}_{\mathrm{e}}\right| - \eta n_{\mathrm{e}} \left|\vec{W}_{\mathrm{e}}\right| - \beta n_{\mathrm{e}} n_{\mathrm{p}} \\
&\quad -\vec{\nabla} \cdot \vec{\Gamma}_{\mathrm{e}} + S_{\mathrm{ph}} \qquad (6.4) \\
\frac{\partial n_{\mathrm{p}}}{\partial t} &= \alpha n_{\mathrm{e}} \left|\vec{W}_{\mathrm{e}}\right| - \beta n_{\mathrm{n}} n_{\mathrm{p}} - \beta n_{\mathrm{e}} n_{\mathrm{p}} \\
&\quad -\vec{\nabla} \cdot \vec{\Gamma}_{\mathrm{p}} + S_{\mathrm{ph}} \qquad (6.5) \\
\frac{\partial n_{\mathrm{n}}}{\partial t} &= \eta n_{\mathrm{e}} \left|\vec{W}_{\mathrm{e}}\right| - \beta n_{\mathrm{n}} n_{\mathrm{p}} - \vec{\nabla} \cdot \vec{\Gamma}_{\mathrm{n}}, \qquad (6.6)
\end{aligned}$$

where S_{ph} is the photoionisation rate and the corresponding fluxes, $\vec{\Gamma}_{\mathrm{e}}$, $\vec{\Gamma}_{\mathrm{p}}$ and $\vec{\Gamma}_{\mathrm{n}}$, are

$$\vec{\Gamma}_{\mathrm{e}} = n_{\mathrm{e}}\vec{W}_{\mathrm{e}} - D_{\mathrm{e}}\vec{\nabla}n_{\mathrm{e}} \tag{6.7}$$

$$\vec{\Gamma}_{\mathrm{p}} = n_{\mathrm{p}}\vec{W}_{\mathrm{p}} \tag{6.8}$$

$$\vec{\Gamma}_{\mathrm{n}} = n_{\mathrm{n}}\vec{W}_{\mathrm{n}}. \tag{6.9}$$

In equations (6.4) to (6.9) $\vec{W}_{\mathrm{e}}$, $\vec{W}_{\mathrm{p}}$ and $\vec{W}_{\mathrm{n}}$ are the drift velocities for electrons, positive ions and negative ions respectively; α, η and β are the ionisation, attachment and recombination coefficients respectively; D_{e} is diffusion coefficient for electrons. The swarm parameters introduced by Kang are used in this work [100], with the air pressure at atmospheric conditions, they are explicitly defined in Appendix E. To find the electric field $\vec{E}$ the electrostatic equation is solved

$$\nabla^2 V = -\frac{\rho}{\varepsilon_0\varepsilon_{\mathrm{r}}} \tag{6.10}$$

where V is the electric potential,

$$\vec{E} = -\vec{\nabla}V \tag{6.11}$$

ε_0 is the absolute permittivity, ε_{r} is the relative permittivity of the material and ρ is the volume charge density. The relative permittivity of air is set to 1, and the relative permittivity of epoxy is set to 4.4. ρ is related to the charge carriers as follows

$$\rho = e(n_{\mathrm{p}} - n_{\mathrm{e}} - n_{\mathrm{n}}), \tag{6.12}$$

where e is the electronic charge.

To calculate the photoionisation rate the three-exponential Helmholtz model developed by Bourdon *et al* was used [101]. This approximates the computationally expensive model proposed by Zheleznyak *et al* [102]. The photoionisation rate, S_{ph}, is approximated as

$$S_{\mathrm{ph}} = \sum_{i=1}^{3} S_{\mathrm{ph}i} \tag{6.13}$$

where each $S_{\mathrm{ph}i}$ solves a Helmholtz equation

$$\nabla^2 S_{\mathrm{ph}i} - (\lambda_i p_{\mathrm{O}_2})^2 S_{\mathrm{ph}i} = -A_i p_{\mathrm{O}_2}^2 S, \tag{6.14}$$

with constants λ_i and A_i given in Table 6.1, p_{O_2} is the partial pressure of oxygen (150 Torr at atmospheric pressure) and

$$S = \xi I \tag{6.15}$$

where

$$I = \alpha n_{\mathrm{e}} \left|\vec{W}_{\mathrm{e}}\right| \tag{6.16}$$

and $\xi = 0.00228$ for the physical conditions under consideration [101, 103]. S will be referred to as the photoionisation source and is directly proportional to the collisional ionisation rate, I. [101].

i	A_i ($\mathbf{m^{-2}Torr^{-2}}$)	λ_i ($\mathbf{m^{-1}Torr^{-1}}$)
1	1.98	5.53
2	51	14.6
3	4886	89

TABLE 6.1: Helmholtz Equation Parameters from [101]

6.3.3 Boundary Conditions

Boundary condition for the drift-diffusion equations are required at the boundaries of the void, they are set as follows

$$\vec{n} \cdot \vec{\Gamma}_{\mathrm{e}} = \vec{n} \cdot \left(a_{\mathrm{e}} n_{\mathrm{e}} \vec{W}_{\mathrm{e}} - \gamma n_{\mathrm{p}} \vec{W}_{\mathrm{p}} \right) \tag{6.17}$$

$$\vec{n} \cdot \vec{\Gamma}_{\mathrm{p}} = \vec{n} \cdot a_{\mathrm{p}} n_{\mathrm{p}} \vec{W}_{\mathrm{p}} \tag{6.18}$$

$$\vec{n} \cdot \vec{\Gamma}_{\mathrm{n}} = \vec{n} \cdot a_{\mathrm{n}} n_{\mathrm{n}} \vec{W}_{\mathrm{n}} \tag{6.19}$$

where γ is the ion-impact secondary emission coefficient,

$$a_i = \begin{cases} 1 & \text{if } \mathrm{sgn}(q_i) = \mathrm{sgn}(\vec{n} \cdot \vec{E}) \\ 0 & \text{otherwise,} \end{cases} \tag{6.20}$$

i =e, p and n, sgn is the sign function, q_i is the charge of the ith species and $\vec{n}$ is the outwards facing normal unit vector at the void surface, these boundary conditions have been used to describe dielectric boundaries in earlier work [7]. The secondary ionisation coefficient at the void surface, γ, was set to a token value of 0.001, it should be noted that the secondary ionisation coefficient has yet to be accurately determined for a large number of dielectric materials. (6.17) neglects incoming thermal flux of charged particles which has been considered in other work [56]. However, as the drift velocity is significantly higher than the thermal velocity for the conditions under consideration, this is not thought to impact the findings of this work, assuming that electron temperatures are at most within an order of magnitude of 1 eV [24].

Boundary conditions are also required for V. These are largely trivial with the exception of the void surface, where charge will be deployed due to the discharge. The surface charge density σ at the void surface can be calculated through

$$\sigma = \int_0^t e\vec{n} \cdot (n_{\mathrm{p}} \vec{W}_{\mathrm{p}} - n_{\mathrm{e}} \vec{W}_{\mathrm{e}} - n_{\mathrm{n}} \vec{W}_{\mathrm{n}})\, dt, \tag{6.21}$$

an approach widely used in the literature [7, 55]. The boundary condition for V at the void boundary is

$$\vec{n} \cdot \left(\vec{D}_1 - \vec{D}_2 \right) = \sigma$$

where $\vec{D}$ is the electric displacement field,

$$\vec{D} = \varepsilon_0 \varepsilon_r \vec{E}, \tag{6.22}$$

and the 1, 2 subscripts denote evaluation in regions either side of a surface with normal vector $\vec{n}$ pointing from region 1 to region 2. In the system under consideration a high voltage electrode, at potential V_0, is located at the top boundary of the geometry and a ground electrode is located at the bottom. Combining this with conditions for the axisymmetric and far field boundaries completes the boundary conditions for V.

In the original integral model of photoionisation perfect absorption at boundaries is assumed [102]. In the work of Bourdon *et al* the external boundaries of the system were effectively in the far field region [101]. At these boundaries $S_{\mathrm{ph}\,1}$ was set equal to the the photoionisation rate calculated using the integral model, with $S_{\mathrm{ph}\,2} = S_{\mathrm{ph}\,3} = 0$. This is because $S_{\mathrm{ph}\ 1}$ corresponds to the smallest value of λ_i, Table 6.1, which means that it is the component with the longest photoionisation range so is likely to be the dominant component in the far-field region. For the arrangement considered here the void boundaries cannot be considered as far field; photoionisation sources will be very close to the void surface. This means that the assumption that $S_{\mathrm{ph}\,1}$ dominates at the boundary is not valid, furthermore the fine numerical mesh required at the boundaries means that calculating S_{ph} from the integral model at the void boundary is computationally expensive. In this system, the dominant Helmholtz component at the boundaries is likely to be the component with the largest source term, corresponding to the largest A_j, which is $S_{\mathrm{ph}\,3}$. It was found that employing Dirichlet boundary conditions on $S_{\mathrm{ph}\,1}$ and $S_{\mathrm{ph}\,2}$

$$S_{\mathrm{ph}\,1} = S_{\mathrm{ph}\,2} = 0 \text{ at the void boundary} \tag{6.23}$$

and Neumann boundary conditions on $S_{\mathrm{ph}\ 3}$,

$$\vec{n} \cdot \vec{\nabla} S_{\mathrm{ph}\,3} = 0 \text{ at the void boundary} \tag{6.24}$$

where $\vec{n}$ is a normal vector at the boundary, gave results that were in good agreement with the full integral model of photoionisation. It should be noted that these boundary conditions are based on empirically fitting the Helmholtz model to the full integral model, and are not indicative of the physical process of photoionisation. This was determined by comparing the full integral model against the Helmholtz model. The collisional ionisation rate I is set to a Gaussian distribution centred on the z axis

$$I = I_0 \exp(-(r^2 + (z - z_0^2))/\delta^2), \tag{6.25}$$

where $I_0 = 10^{31}$ $m^{-3}s^{-1}$, z_0 is the z coordinate of the centre of distribution and δ_0 is a spatial parameter governing the spread of the distribution. Two cases are considered, $z_0 = 0$ mm, ionisation taking place in the centre of the void, and $z_0 = 0.5$ mm, ionisation taking place at the void boundary. $\delta = 0.1$ mm in both cases, this is analogous to the approach used in [101]. A comparison of the photoionisation rate along the z axis of the void using the two different models is shown in Figure 6.2. It can be seen that the agreement is fairly good from an order of magnitude perspective with some notable discrepancies.

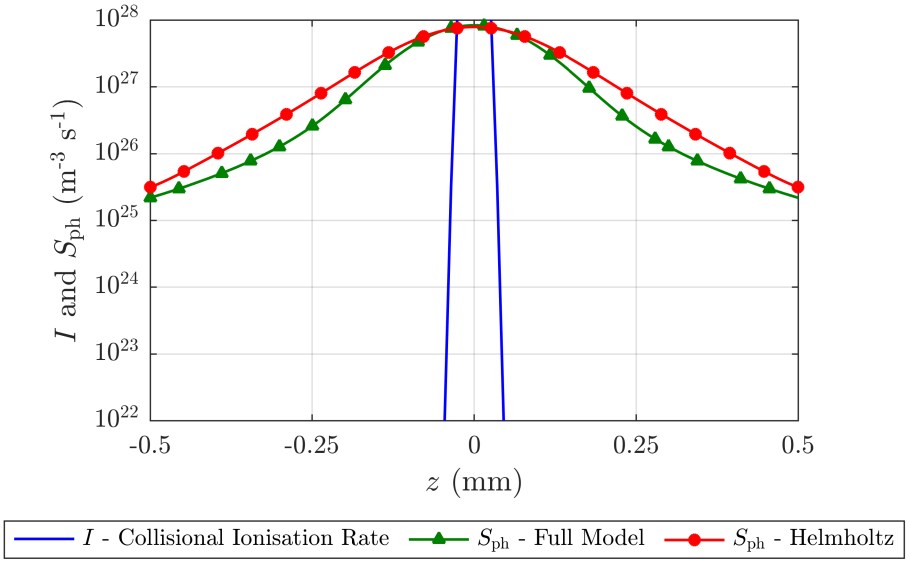

(a)

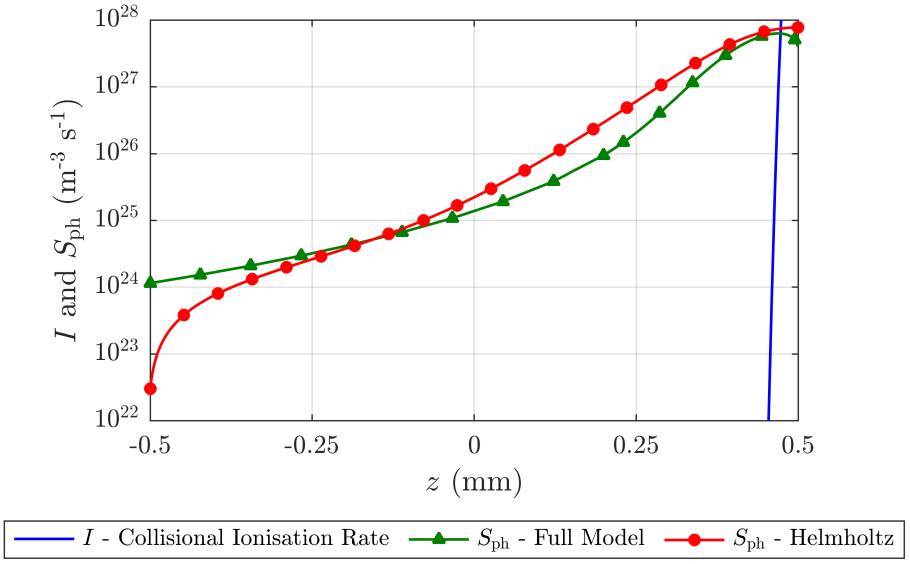

(b)

FIGURE 6.2: Comparison of photoionisation rate calculated using full model of photoionisaton and Helmholtz model with modified boundary conditions. The Gaussian collisional ionisation production rate was centred at: (a) $z_0 = 0$ mm and (b) $z_0 = 0.5$ mm

The absolute error between the full and Helmholtz models is shown in Figure 6.3. The error is highest at the void boundary, $z_0 = 0.5$ mm, with an error of 3.7×10^{27} m^{-3} s^{-1}. It should be noted however that in this region the collisional ionisation, I, is dominant, with a value of 10^{31} m^{-3} s^{-1} at the void boundary and photoionisation is a relatively insignificant process. It is not thought that these discrepancies will significantly impact

the findings presented in this work as they are all roughly within an order of magnitude, which was the case with the original work where this technique was successfully applied [101].

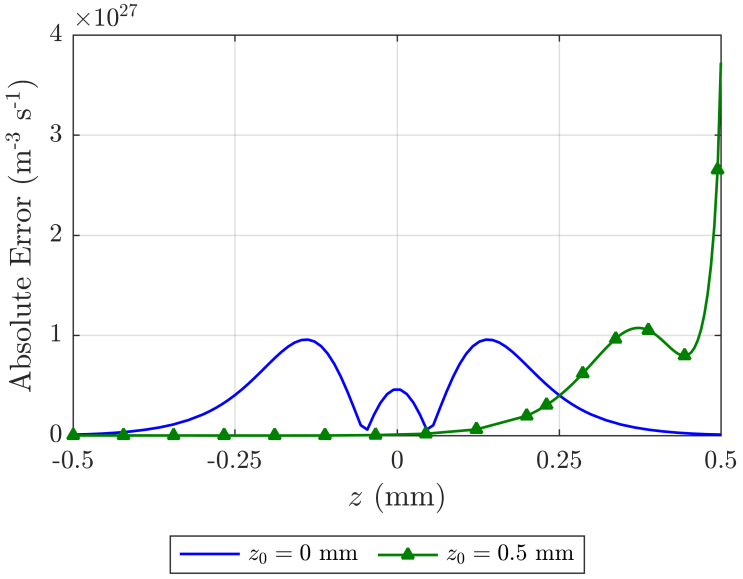

FIGURE 6.3: Absolute error between the photoionisation rate calculated using the full model and Helmholtz model. In the region close to the void boundary where the error is largest the collisional ionisation rate dominates photoionisation.

The boundary conditions used are shown in Tables 6.2 and 6.3 for the two dimensional axisymmetric model and one dimensional model respectively. Boundaries are defined using the vertices in Figure 6.1. It should be noted that the drift diffusion and Helmholtz equations are only solved inside the void region and as such they only require boundary conditions at the void surface.

Boundary	V	$n_{i=\mathrm{e,p,n}}$	$S_{\mathrm{ph}\,1}$	$S_{\mathrm{ph}\,2}$	$S_{\mathrm{ph}\,3}$
AB	V_0	-	-	-	-
CE	$\frac{\partial V}{\partial r} = 0$	$\frac{\partial n_i}{\partial r} = 0$	$\frac{\partial S_{\mathrm{ph}\,1}}{\partial r} = 0$	$\frac{\partial S_{\mathrm{ph}\,2}}{\partial r} = 0$	$\frac{\partial S_{\mathrm{ph}\,3}}{\partial r} = 0$
CD,DE	$\vec{n} \cdot \left(\vec{D}_1 - \vec{D}_2\right) = \sigma$	(6.17)	$S_{\mathrm{ph}\,1} = 0$	$S_{\mathrm{ph}\,2} = 0$	$\vec{n} \cdot \vec{\nabla} S_{\mathrm{ph}\,3} = 0$
AC,EF	$\frac{\partial V}{\partial r} = 0$	-	-	-	-
BG	$\vec{n} \cdot \vec{D} = 0$	-	-	-	-
FG	0	-	-	-	-

TABLE 6.2: Boundary Conditions for the Two Dimensional Axisymmetric Model

Boundary	V	$n_{i=\mathrm{e,p,n}}$	$S_{\mathrm{ph}\,1}$	$S_{\mathrm{ph}\,2}$	$S_{\mathrm{ph}\,3}$
H	0	-	-	-	-
I, J	$\vec{n}\cdot\left(\vec{D}_1-\vec{D}_2\right)=\sigma$	(6.17)	$S_{\mathrm{ph}\,1}=0$	$S_{\mathrm{ph}\,2}=0$	$\vec{n}\cdot\vec{\nabla}S_{\mathrm{ph}\,3}=0$
K	V_0	-	-	-	-

TABLE 6.3: Boundary Conditions for the One Dimensional Model

6.3.4 Initial Conditions

Due to their explicit time dependence initial conditions are required for the drift diffusion equations. The initial conditions for the electron and positive ion number densities were set to be a Gaussian seed charge, with a magnitude insufficient to distort the applied field. This approach has been widely used when modelling breakdown in air using drift diffusion equations [7]. The initial number of negative ions was set to zero. Explicitly the initial conditions for the number densities are

$$n_{\mathrm{e,p}}|_{t=0} = n_0 \exp(-(r^2+(z-z_0^2))/s_0^2), \tag{6.26}$$

$$n_{\mathrm{n}}|_{t=0} = 0 \tag{6.27}$$

where $n_0 = 10^{11}$ m^{-3}, z_0 =0.5 mm and $s_0 = 25$ μm. Order of magnitude variations in the parameters defining the initial distribution, n_0, z_0 and s_0, were only found to impact the time taken for discharges to begin, and did not impact the findings of the work presented in Section 6.4.

6.3.5 Measurable Quantities

For PD activity under AC conditions a PD is typically quantified by its angle of occurrence in the AC cycle, known as phase angle, and the change in charge on a suitable measuring electrode, known as the apparent charge [4]. In this work single discharges are investigated at a range of applied voltages, so the phase angle is not a quantity of interest. For the system under consideration the measuring electrode is assumed to the the ground electrode, the apparent charge, q'_{PD}, of the discharge is

$$q'_{\mathrm{PD}} = \int_S \vec{n}\cdot\left(\vec{D}|_{t=t_{\mathrm{f}}} - \vec{D}|_{t=t_0}\right) dA, \tag{6.28}$$

where t_0 is the time immediately before the discharge takes place, t_{f} is the time the discharge finishes, S is the ground electrode surface and $\vec{n}$ is an outwards facing normal unit vector. Comparing the PD system under investigation with PD measurements in

similar systems it is expected that PD magnitudes will be in the order of 100 pC [4, 9]. The apparent current pulse I' on the measuring electrode can also be calculated

$$I' = \int_S J' \, dA, \tag{6.29}$$

where J' is the apparent current density on the measuring electrode surface defined as

$$J' = \frac{\partial}{\partial t}(\vec{n} \cdot \vec{D}). \tag{6.30}$$

Measurements of the current pulse I', for PD systems similar to the that under investigation, have a timescale in the order of nanoseconds with a sharp rise followed by a relatively long decay [20].

6.3.6 Model Configurations

In order to test the concepts, outlined in Section 6.2, it is necessary to run the model in different configurations as follows:

(A) **Discharges in Virgin Voids** - It is proposed to use the two dimensional model to examine the physics of PD in virgin voids, i.e. $\sigma_{t=0} = 0$, at a range of applied voltages. By gradually increasing the applied voltage until a discharge occurs, the inception field for the void can be determined and compared against the value calculated using (6.1). By considering the field after the discharge the residual field can be determined, which can then be compared to the value calculated using (6.2). The plasma dynamics and the surface charge distributions after PD can also be investigated. The model is set to have a constant applied voltage for the duration of the discharge even though in reality the discharges are occurring in an AC system with a varying applied voltage. This is because the discharges take place over nanoseconds, whereas the applied voltage frequencies of interest are typically 50-60 Hz. Therefore the variation in the applied voltage over the time scale of the discharge is negligible. The results from this arrangement will therefore offer insight into Concepts 1, 2 and 3.

(B) **Post-Discharge Plasma Dynamics** - Due to timescales involved and the corresponding computational cost, the one dimensional simulation will be used to investigate the rate of charge recombination after the discharge. Unlike the other configurations the timescales of recombination are not negligible compared to the period of the AC cycle. It is of interest to see how the variation of the applied field influences charge recombination, if at all. Therefore two cases will be considered, a discharge followed by a rising applied field, that is increasingly opposing the local field from the discharge, or a discharge followed by a falling applied field, which is

decreasingly opposing the local electric field from the discharge. These simulations will provide insight into Concepts 1 and 4.

(C) **Effect of Subsequent Discharges** - The resulting surface charge distribution from a discharge in a virgin void will be used as an initial condition for a second discharge. This will provide insight into the physics of PD in an electric field that is distorted by the surface charge, and also see how the charge deployed by the second PD compares to the first. This will therefore provided insight into Concepts 1 and 3.

6.3.7 Implementation

The model is implemented in COMSOL Multiphysics 5.3 using the in-built physics libraries. Six libraries were used; three transport of diluted species libraries to solve (6.4)-(6.6); an electrostatics library to solve (6.10); a coefficient form PDE library to solve (6.14) and a boundary ODE library to solve (6.21). In the transport of diluted species libraries the consistent stabilisation techniques of streamline and crosswind diffusion were used. This approach was used in a previous the model, from which this model was developed, and is similar to recent work in literature [7, 53]. The variable-order variable step-size backward differentiation formulae (BDF) are used for time-stepping with the non-linear controller activated, in conjunction with the PARDISO direct solver. The libraries were solved for independently in a segregated arrangement as it was found to vastly reduce the computational time and improved the numerical stability of the solution.

The final step in implementing the model is the creation of a numerical mesh. From numerical experiments with the one dimensional model it was found that sharp gradients in the charged species number densities were present at the void boundary, in particular at points close to the applied voltage boundary and the mesh resolution required in the one dimensional model was used as a guide for meshing the two dimensional model geometry. It was found that a numerically stable solution could be achieved with a maximum element size of 1 μm within 0.1 mm of the void boundary, with the maximum element size of the rest of the void set to 5 μm. In order to accurately calculate the apparent charge a reasonably fine mesh is also required in the epoxy resin region, this was achieved by restricting the maximum element size to 20 μm. The full mesh consisted of 272960 triangular elements. The two dimensional model was solved on 16 2.6 GHz Intel Sandybridge processors and had a run time in the order of days. Numerical experiments, using the one dimensional model, of different solvers and time stepping algorithms gave equivalent solutions to the setup used here. The full mesh consisted of 272960 triangular elements and is shown in Figure 6.4. Simulations using a mesh refined by a factor of 2 in all regions resulted in a change within 5 % to the quantities of interest.

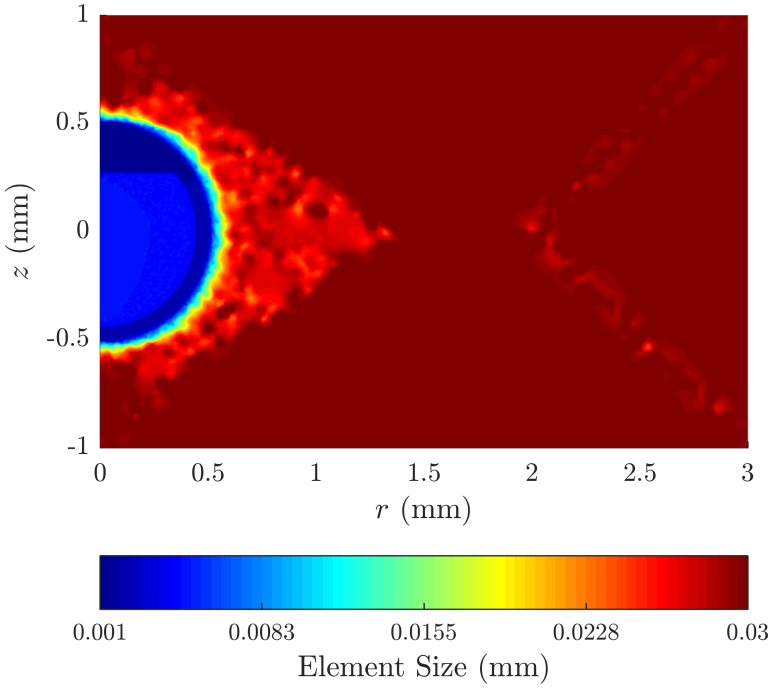

FIGURE 6.4: Element size surface plot of the numerical mesh used for the simulations. Mesh scaling was developed based on the plasma dynamics observed.

6.4 Results and Discussion

Three different model configurations are considered in this work; Discharges in Virgin Voids; Effect of Subsequent Discharges and Post-Discharge Plasma Dynamics. The results for each configuration are presented in this section and their implications discussed.

6.4.1 Discharges in Virgin Voids

The one and two dimensional models were used to investigate discharges in virgin voids. A range of applied voltages, V_0 in Table 6.2, with negative polarity in increments of -0.5 kV, were considered. The applied voltages was set to a negative polarity so that the apparent charge and current was positive. Due to the symmetry of the geometry and governing equations an applied voltage with the same magnitude and positive polarity would simply have resulted in identical to the results at negative polarity after having undergone a reflection in the central plane, $x = 0$ and $z = 0$ for the one and two dimensional models respectively. In other words the dynamics of the discharge will simply be reversed due to a change in voltage polarity, this is because the charged species never interact directly with the metallic electrodes as the entire region in which

the discharge takes place is surrounded by dielectric material. The anti-symmetry of PD activity under changes in voltage polarity in systems of this type, discharges in gaseous voids surrounded by dielectric material, under AC conditions is observed experimentally [4, 9].

The dynamics of the discharges were the same at all applied voltages, therefore for the sake of brevity figures showing the dynamics of the charged species will only be provided for the two dimensional model discharge at 9 kV. The results are similar to dynamics of dielectric barrier discharges described elsewhere in the literature [57, 58]. The dynamics of the discharge can be split into approximately four stages (I-IV) :

(I) - 0 to 5 ns - The discharge begins with the Gaussian seed charge moving to the bottom of the void, see Figure 6.5. The local field is initially insufficient to distort the applied field, see Figure 6.5c.

(II) - 5 to 10 ns - At the bottom of the void the charge multiplies, with the number densities growing to peak values of 10^{19} m^{-3}, see Figure 6.6, at this time negative charge deployed into the bottom of the void leads to a change in surface charge density, see Figure 6.9. The local field due to the charged species is now noticeable, see Figure 6.6c. Significant changes to the location and magnitude of the initial seed charge was only found to influence the length of time of the multiplication phase, no other noticeable impact on the plasma dynamics was observed.

(III) - 10 to 20 ns - The number densities then grow to such an extent that a positive streamer is formed, moving towards the top of the void. The number densities of charged species reach peak values of 10^{21} m^{-3}, and the local fields due to the space charge is significantly higher than the applied field, see Figure 6.7. The positive streamer reaching the top of the void, between 15 and 20 ns, leads to an increase in the positive surface charge density on the top surface of the void, see Figure 6.9. The positive charge spot has a higher peak surface charge density, but is less diffused than the negative charge spot, see Figure 6.9. The surface charge density distributions for 9.5 kV and 10 kV are essentially scaled distributions of those at 9 kV. Similar distributions were also observed in earlier simulation work, [57], and in Pockels cell measurements of surface charge density from discharges in air gaps bounded by a dielectric material below and a metallic electrode above [6].

(IV) - After 20 ns - After the positive streamer has reached the top of the void the local electric field from the volume charge density begins to decrease and the surface charge density deployed by the discharge is sufficient to nearly completely "short" the electric field inside the void except in regions close to the top surface of the void, see Figures 6.8c and 6.11. At the top surface of the void, deployment of positive surface charge continues at a slow rate, due to the low values of positive ion flux, due to low values of the electric field and consequently positive ion velocity.

After hundreds of nanoseconds the deployment of positive surface charge stops, and the electric field is "shorted" in all regions in the void. The discharge now enters the charge relaxation phase, which occurs over much longer timescales and will be investigated in more detail in Section 6.4.2.

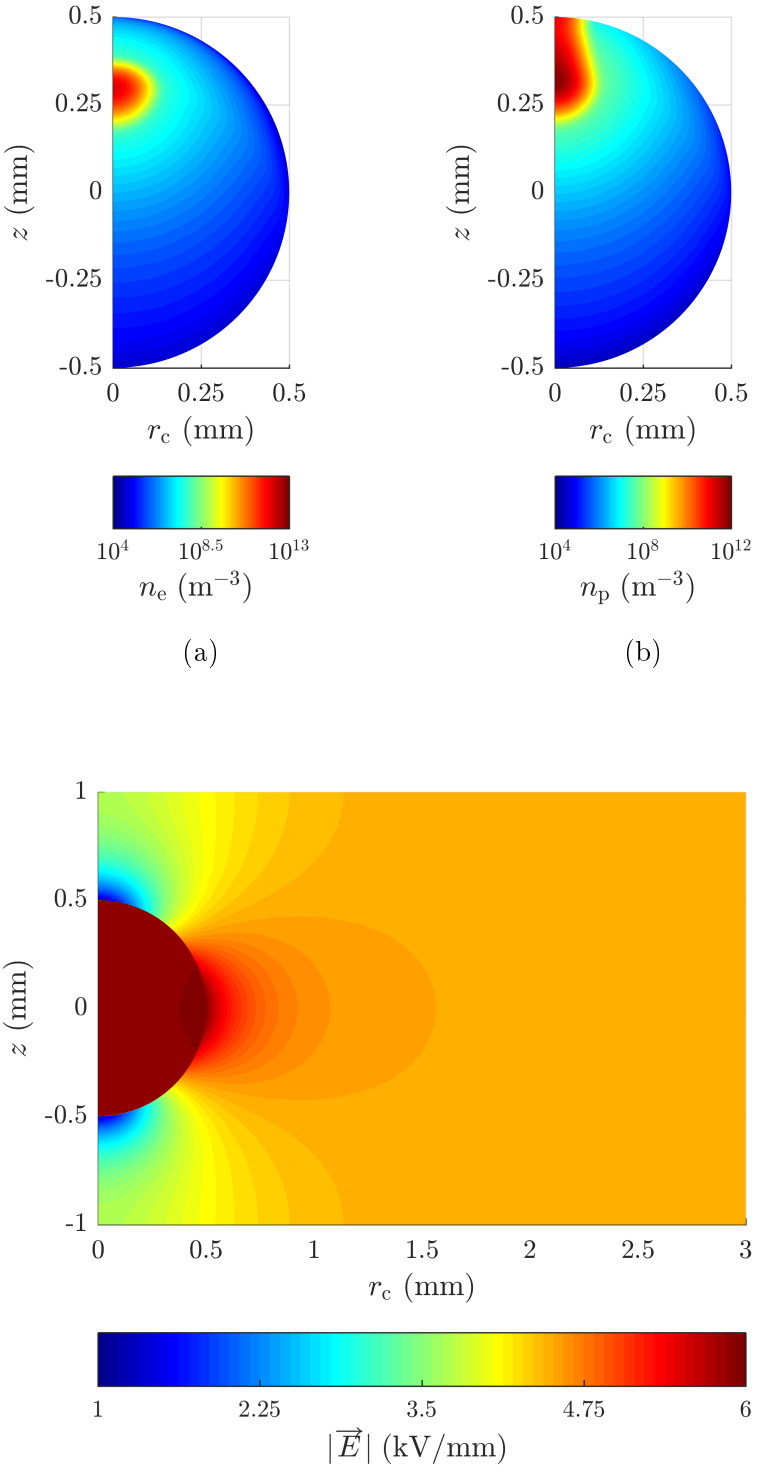

FIGURE 6.5: Discharge dependent variables at 1 ns (I): (a) electron number density, (b) positive ion number density, (c) electric field magnitude.

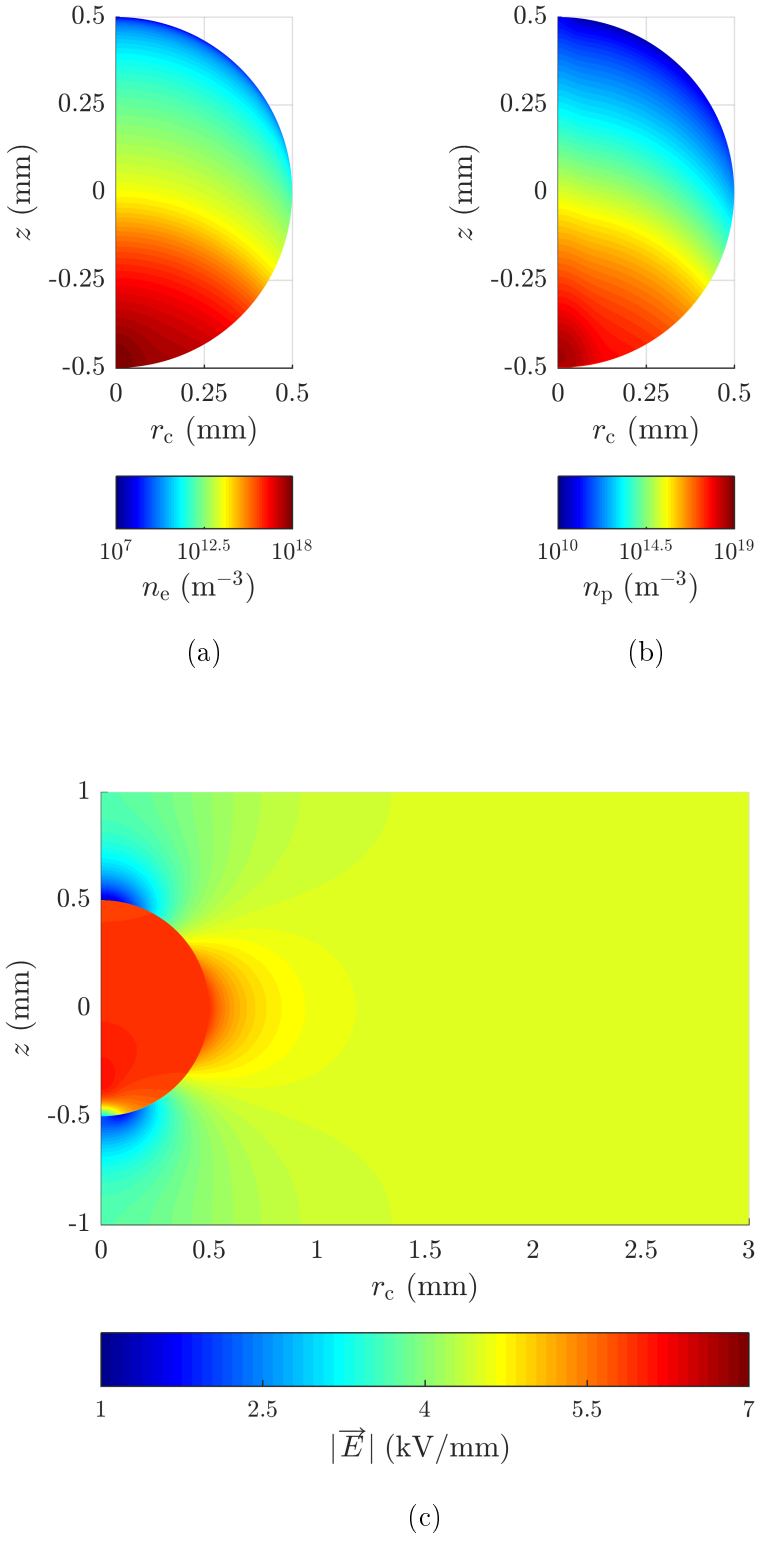

FIGURE 6.6: Discharge dependent variables at 7 ns (II): (a) electron number density, (b) positive ion number density, (c) electric field magnitude.

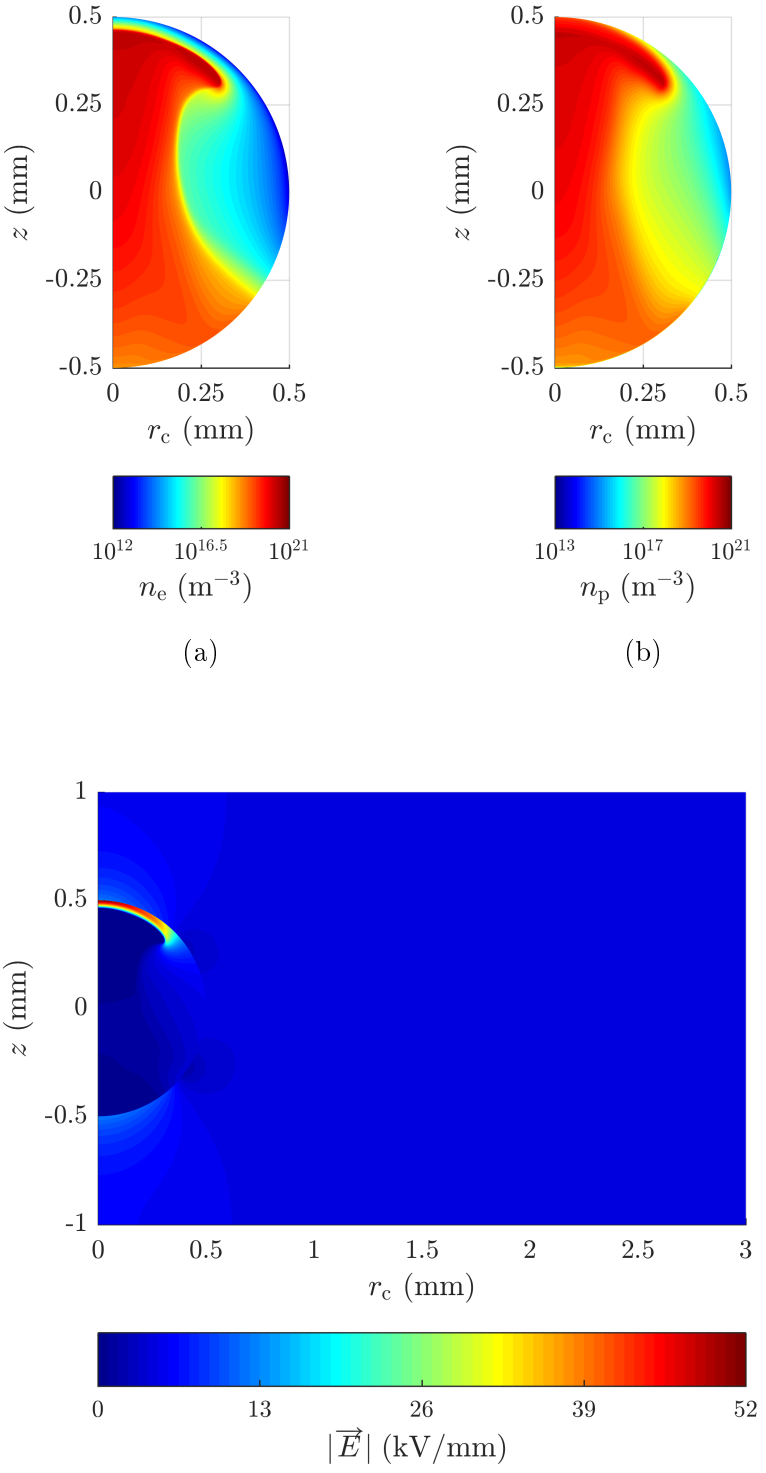

FIGURE 6.7: Discharge dependent variables at 15 ns (III): (a) electron number density, (b) positive ion number density, (c) electric field magnitude.

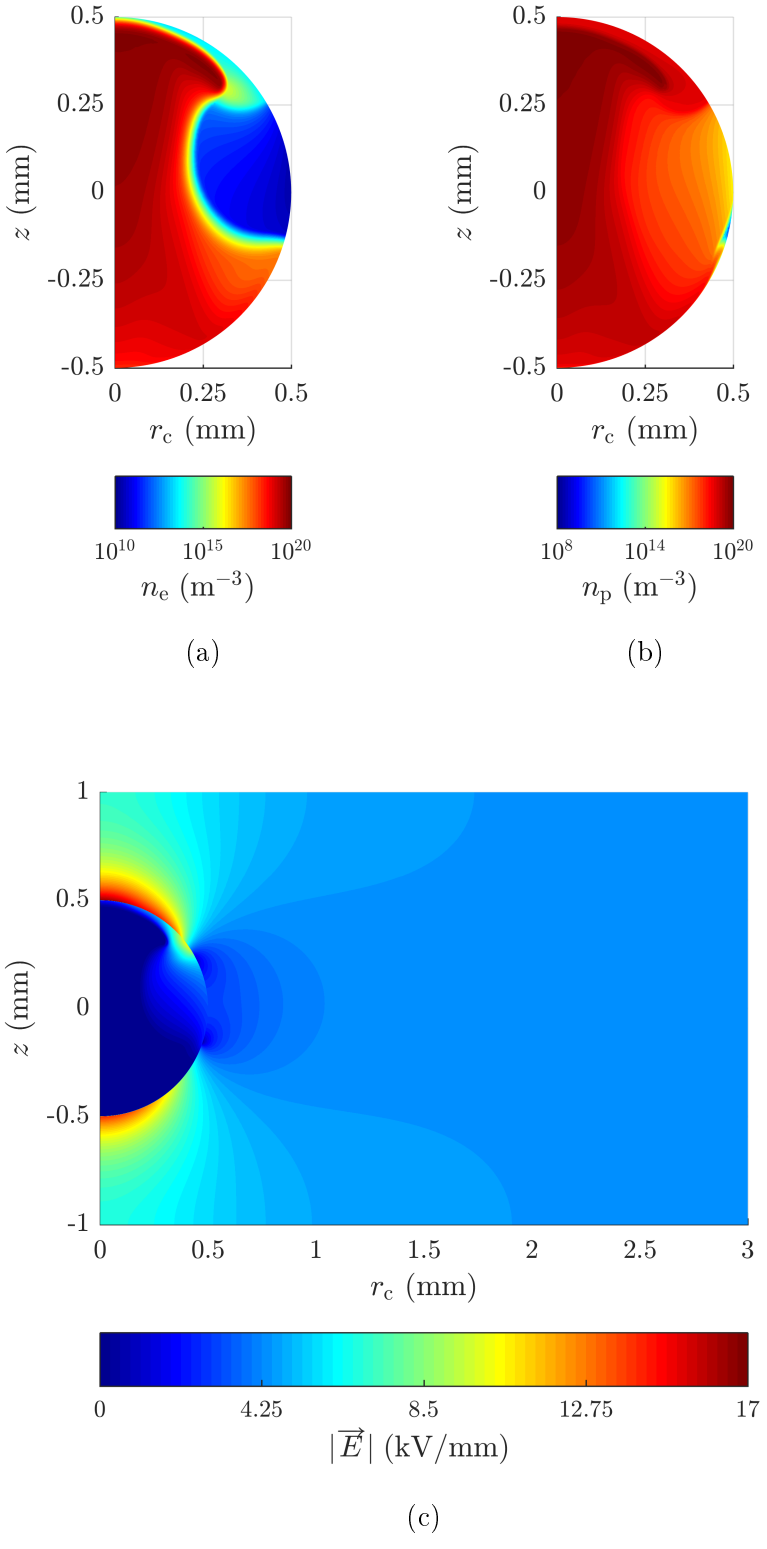

FIGURE 6.8: Discharge dependent variables at 60 ns (IV): (a) electron number density, (b) positive ion number density, (c) electric field magnitude.

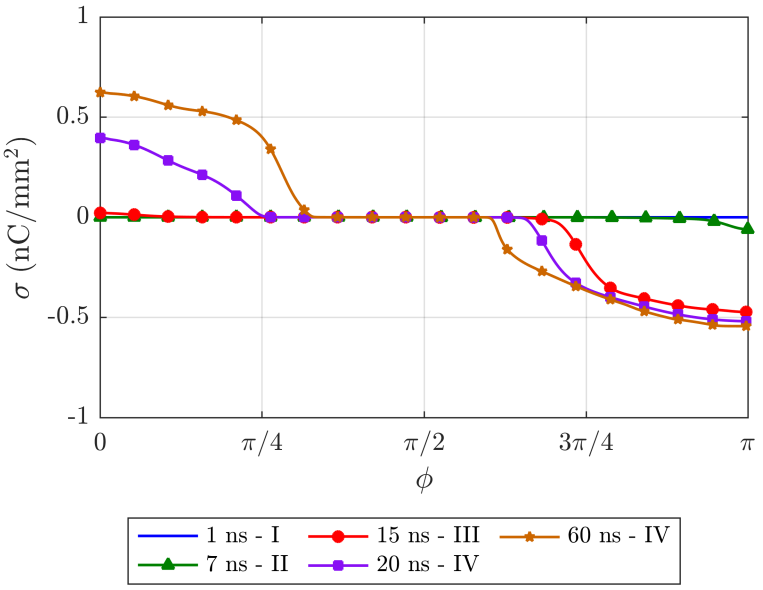

FIGURE 6.9: Surface charge density on the void surface, specified by polar angle ϕ, at different times during the discharge at 9 kV. The stages corresponding to each time are also provided.

It also of interest to compare the standard measurable quantities of the discharges, apparent charge and current, at different applied voltages. The apparent charges are shown in Table 6.4. They display an approximately linear increase with the applied voltage. This is as expected, because the discharge deploys surface charge at the boundaries of the void to oppose the applied field. As the applied voltage increases the local electric field from the discharge will increase to oppose it and there is a linear relationship between charge and its corresponding electric field. The magnitude of the discharges were in the range of 100 pC, which is in good agreement with existing measurements in the literature [4, 9]. An earlier version of the model with a geometry based on an experimental setup in the literature, was in good agreement with the measured apparent charge magnitudes, with a simulated apparent charge magnitude of 546 pC for experimental apparent charge magnitudes in the range of 500-600 pC [15]. The apparent current is shown in Figure 6.10.

Applied Voltage (kV)	**Apparent Charge (pC)**
9	176
9.5	187
10	204

TABLE 6.4: Apparent Charge Magnitudes

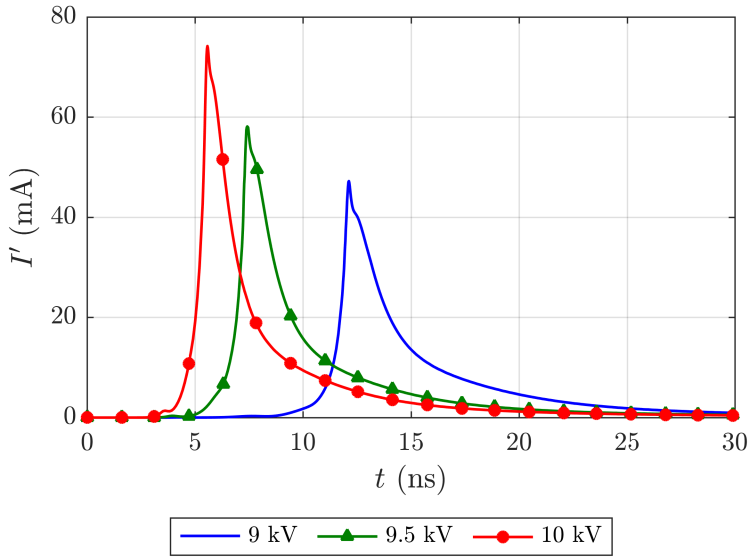

FIGURE 6.10: Figure showing the apparent current on ground electrode at different applied voltages (two dimensional model only).

In concept 1, see Section 6.2, an equation for calculating the inception field, i.e. the minimum electric field at which a PD can occur, was introduced. For the conditions present in the system under consideration, the inception field calculated using (6.1) is 4.7 kV/mm. In the two dimensional model the lowest applied voltage at which a discharge took place was 9 kV, which corresponds to an inception field between 5.6 kV/mm and 5.9 kV/mm as the applied voltage was increased in increments of 0.5 kV. For the one dimensional model the lowest applied voltage at which the discharge took place was 7 kV, which results in an inception field between 5.3 kV/mm and 5.7 kV/mm. There is therefore good agreement between the one and two dimensional models, in terms of inception field prediction, and reasonable agreement with the inception field formula (6.1). A noticeable disagreement with canonical reasoning is that the electric field drops to an residual value after the discharge. For the system under consideration, this residual value is 0.88 kV/mm, calculated using (6.2). Instead of falling to this value, the electric field inside the void is significantly lower immediately after the discharge has taken place, see Figure 6.11, except in regions close to the top of the void, which are shorted out but over longer timescales as will be shown in Section 6.4.2.

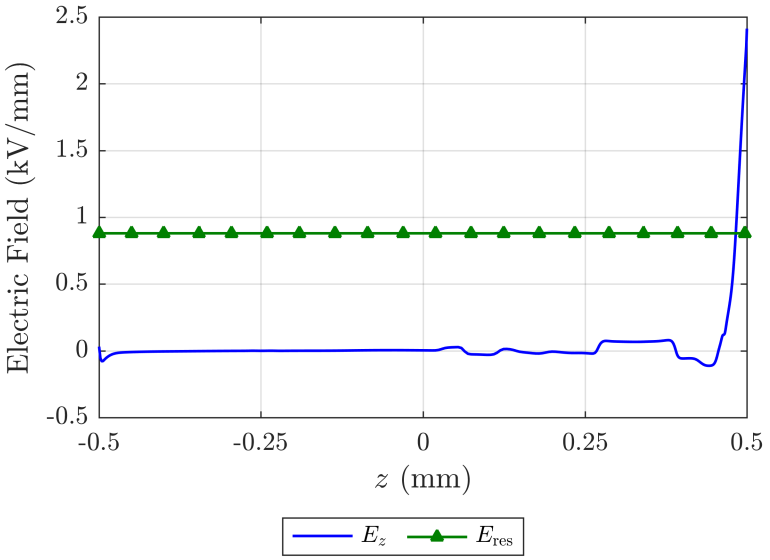

FIGURE 6.11: Figure showing the z component of the electric field magnitude the symmetry axis inside the void at 60 ns for the two dimensional 9 kV discharge simulation and the residual field calculated using (6.1).

In the next section the one dimensional model is used to investigate the dynamics of the plasma after the discharge. This is due to the long time scales involved, and the vastly quicker speed of the one dimensional model compared to the two dimensional model. To justify this approach, it is necessary to verify that the plasma dynamics of the one and two dimensional model are approximately equivalent. Analysis of the one dimensional plasma dynamics, which will not be discussed for brevity, revealed that the discharge can be split into the same four stages identified in the two dimensional case. The magnitude and distribution of charged species are also similar for the one and two dimensional models, see Figure 6.12. It should be noted that, due to the geometry, the same applied voltage will result in an applied electric field approximately 16% higher in the one dimensional model compared to the two dimensional model, which will impact discharge dynamics. By definition, the surface charge is assumed to be uniformly distributed over the top and bottom surfaces in the one dimensional model. It was found that the peak surface charge density value in the two dimensional model is approximately twice as large as the uniform surface charge density in the one dimensional model. The surface charge density on the void surface also has similar dynamics for both one and two dimensional cases, see Figure 6.13.

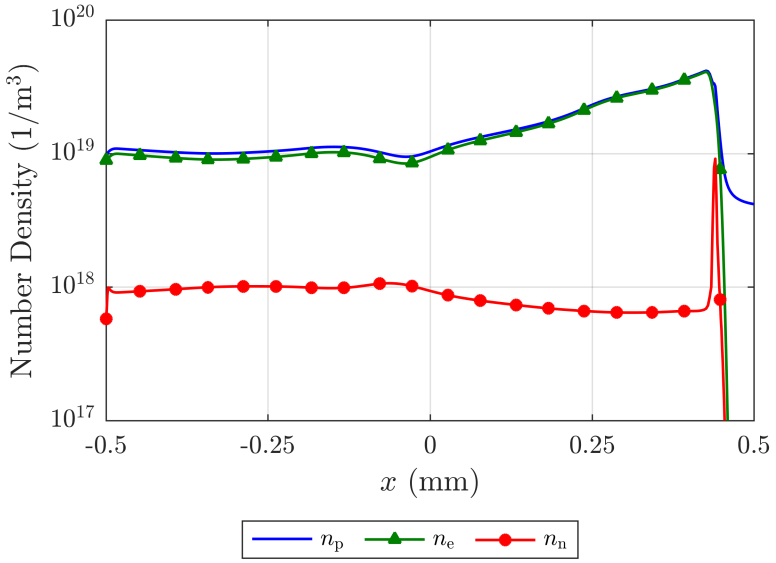

(a)

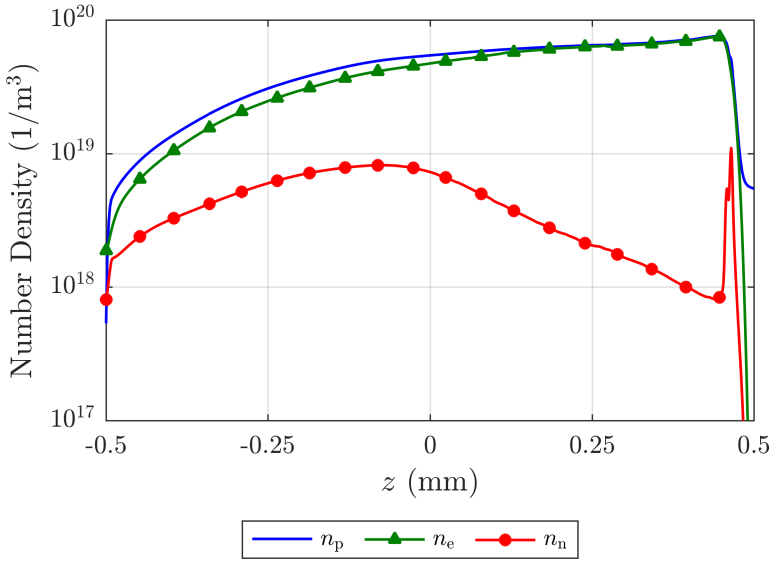

(b)

FIGURE 6.12: Distribution of charged species number density at a time of 60 ns into the 9 kV discharge simulation for: (a) one dimensional case in the void domain and (b) two dimensional case along the symmetry axis inside the void.

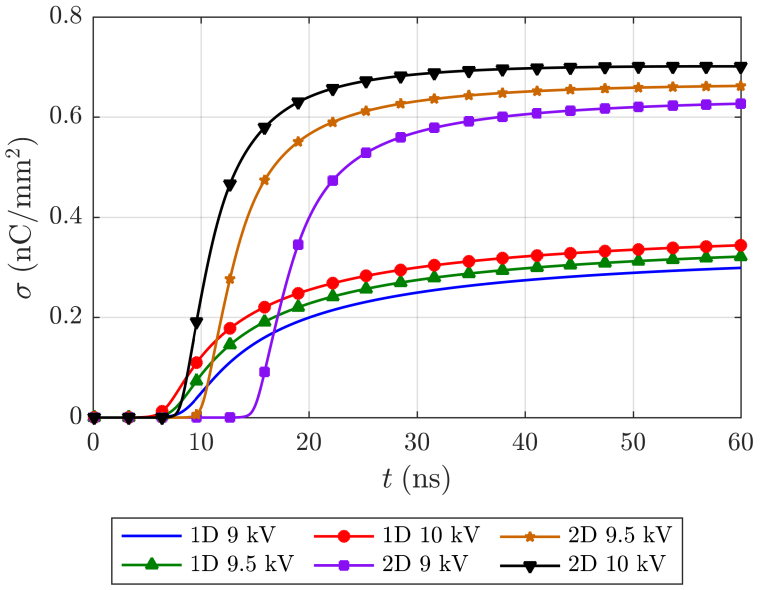

(a)

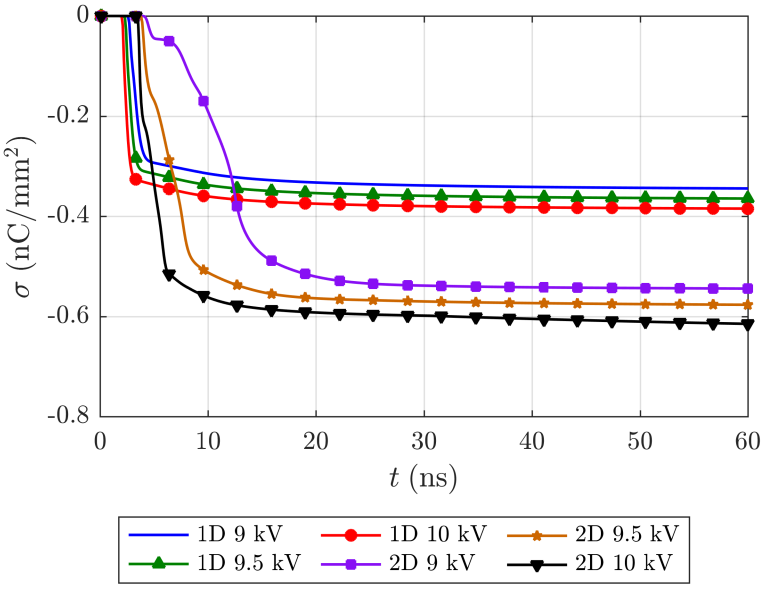

(b)

FIGURE 6.13: Dynamics of surface charge density: (a) at the top of the void and (b) at the bottom of the void.

When comparing the measurable quantities, it must be noted that the apparent current and charge cannot be calculated in the one dimensional case as the results are equivalent to a discharge occurring uniformly across an infinitely large gap, however, the current density can be calculated. Due to the dimensionality of the model, the current density magnitudes are significantly higher in the one dimensional case compared to the two

dimensional case. As such, a comparison of the normalised current density is provided in Figure 6.14.

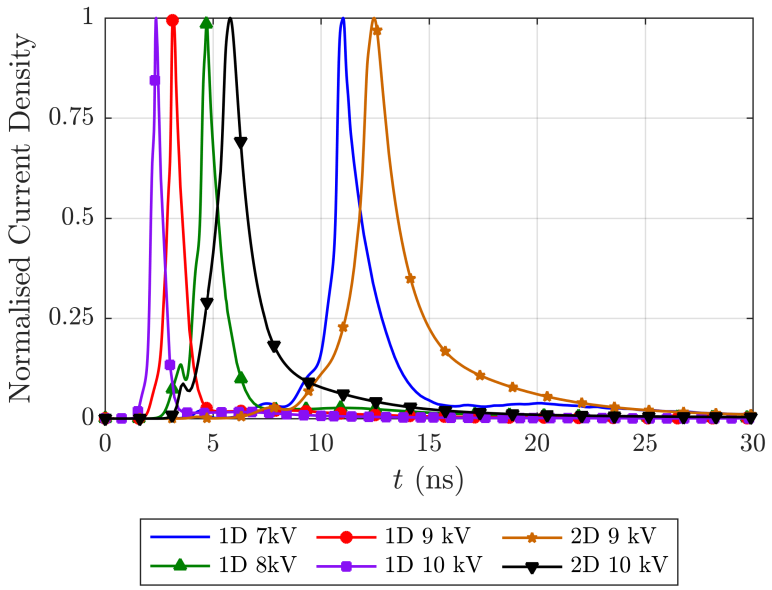

FIGURE 6.14: Normalised apparent current density (1D and 2D model). The apparent current density is evaluated at the ground electrode in the one dimensional case and at the intersection of the ground electrode and the symmetry axis in the two dimensional case. Note that the 1D 8 kV and 2D 10 kV have similar electric field strengths.

It has now been verified that the one dimensional model is an acceptable analog of the two dimensional model. In the next section the dynamics of the plasma in the post-discharge regime will be investigated.

6.4.2 Post-Discharge Plasma Dynamics

The physics of the discharge itself has been already discussed in Section 6.4.1. In this section the time evolution of the plasma cloud that remains after the discharge is investigated using the one dimensional model. The simulation was initialised with a discharge with an applied voltage of 9 kV in an 18 kV 50 Hz AC cycle, see Figure 6.15. Two cases were then considered, a discharge followed by a rising applied field, i.e. a field that is increasingly opposing the local field from the discharge, or a discharge follow by a falling applied field, which is decreasingly opposing the local electric field from the discharge. In both cases the simulation was run until there was no free charge left in the air, it was found that 0.2 ms was sufficient. The total amount of a given charge carrier in the void is calculated as follows

$$N_i = \int_{-R}^{R} n_i \, dx, \tag{6.31}$$

where i = e,p,n and N_i has units of m^{-2}. The variables of interest are N_i and the surface charge at the void boundary.

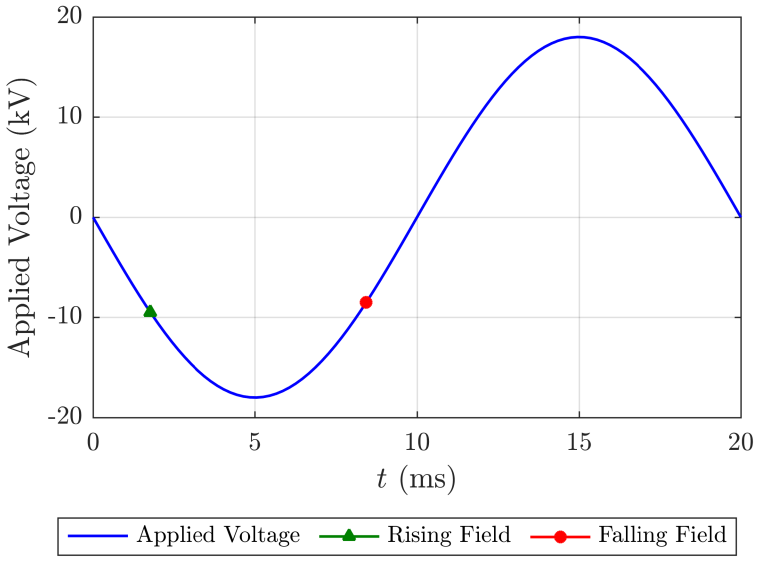

FIGURE 6.15: Figure showing the applied voltages considered to investigate post discharge plasma dynamics.

As was discussed in the previous section after the discharge has stopped the electric field inside the void is significantly reduced, except in regions close to the top of the void where the electric field was significantly higher. It was found that, after 3 μs this high field region was removed, for both rising and falling fields, and the electric field throughout the void was relatively uniform and significantly below the residual value, with an electric field in the order of magnitude of 0.1 kV/mm see Figure (6.16). The removal of this high field region is due to the deployment of positive charge into the top electrode surface, which opposes the high field generated by the volume charge, and the movement of charge in the void to maintain a low electric field.

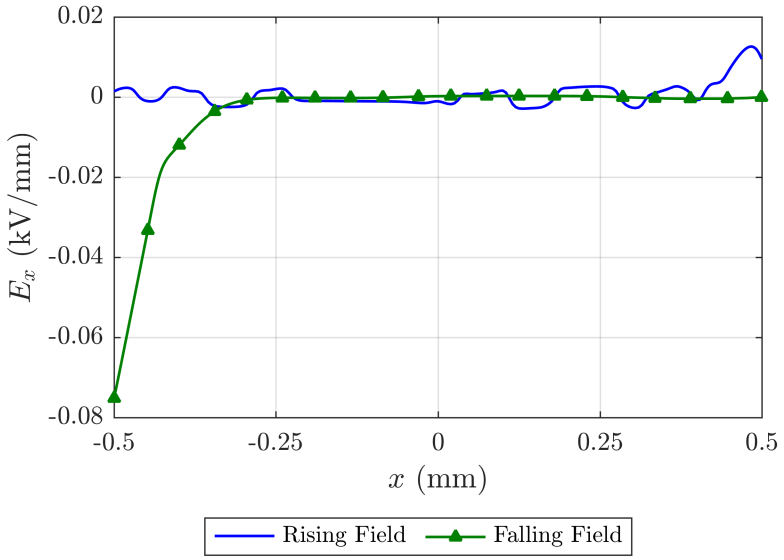

FIGURE 6.16: Figure showing the electric field in the void after 3 μs for the rising and falling field cases and the residual field calculated using (6.1).

Recombination processes scale with the product of the two charged species number densities, (6.4), (6.5) and (6.6). This leads to a higher recombination rate immediately after the discharge, which then decreases significantly once $N_i \sim 10^{14}$ m^{-2}. The main process by which charge is removed from the air is then by movement into the dielectric boundary. This process takes approximately the same time in both the rising and falling case, 0.15 ms, as shown in Figure 6.17.

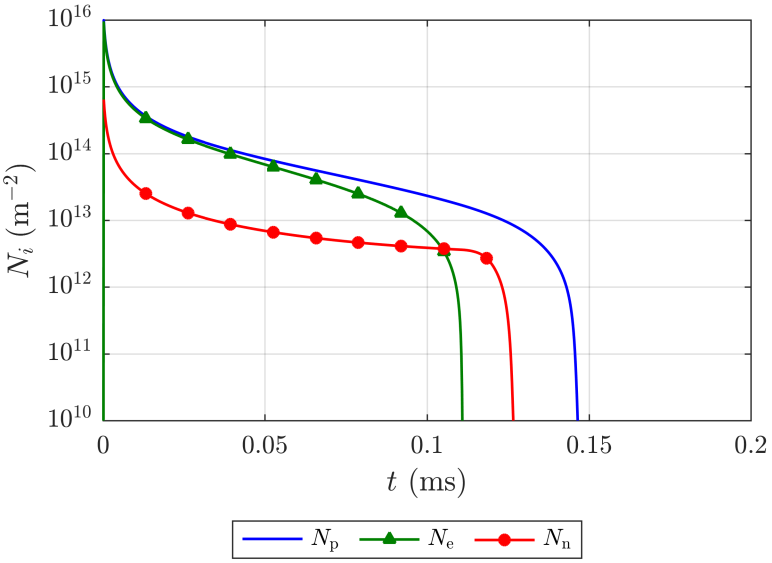

(a)

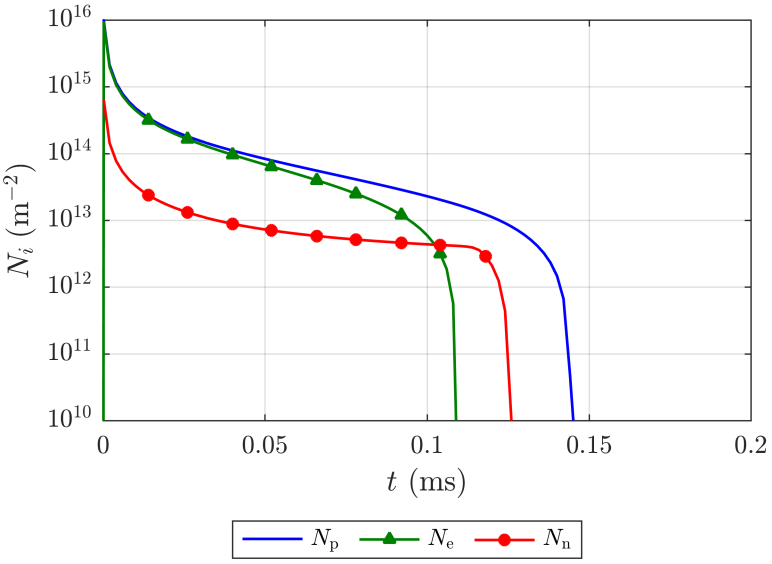

(b)

FIGURE 6.17: Time evolution of charged species in the air gap of the one dimensional model after the discharge at 9 kV: (a) rising field and (b) falling field.

The charge deployed into the dielectric boundary by the plasma cloud enhances the charge already deployed by the discharge in the rising field case, and opposes it in the falling field case. In the rising field this results in a small amount of charge added to the existing surface charge, for the falling field a small amount of the charge added to the

surface is removed. The dynamics of the surface charge at the dielectric boundaries is shown in Figure 6.18.

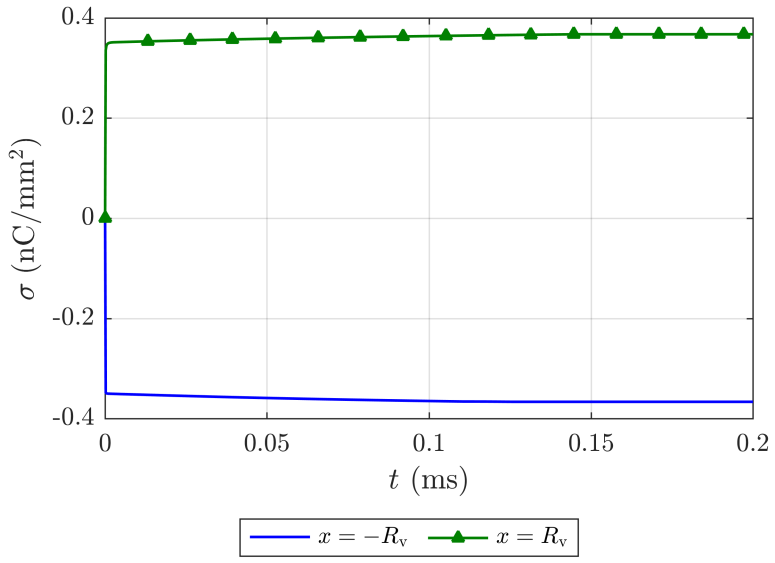

(a)

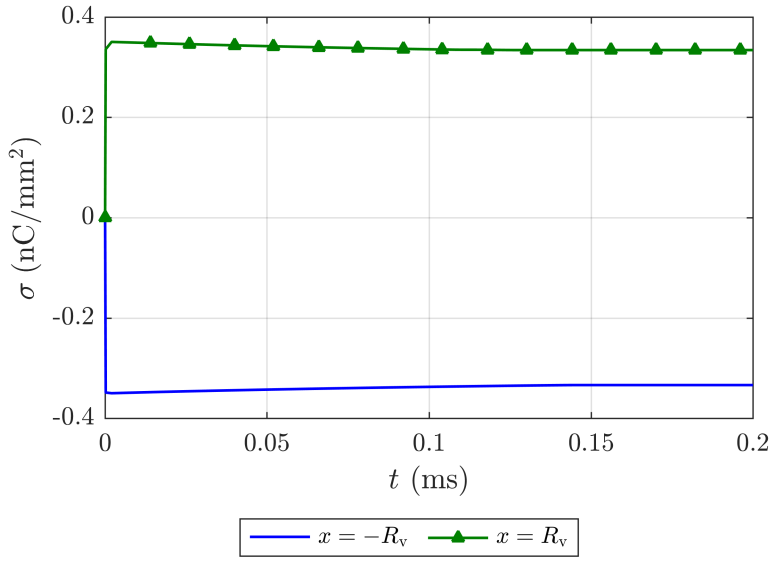

(b)

FIGURE 6.18: Time evolution of surface charge at the void boundaries in the one dimensional model after the discharge at 9 kV: (a) rising field and (b) falling field.

Due to the simplicity of the dynamics in the post discharge regime it is possible to analyse the results analytically subject to certain simplify assumptions. The two assumptions made in this analysis are:

1. The number densities of charged particles are uniformly distributed across the void and are in perfect equilibrium,

$$n_{\mathrm{p}} = n_{\mathrm{e}} + n_{\mathrm{n}}, \tag{6.32}$$

which means that the electric field due to the space charge in the air gap is zero.

2. The applied field, E_0, is perfectly cancelled by the field due to bipolar surface charge distributions at the void boundaries, E_σ, so the electric field inside the void is zero

$$E_0 = -E_\sigma \tag{6.33}$$

Under these assumptions these assumptions the only processes governing charge dynamics is recombination in the air gap and the flux of charged species into the wall. These processes will be considered in isolation for the sake of simplicity. Firstly, if only recombination takes place the drift diffusion equations become

1.

$$\frac{\partial n_{\mathrm{e}}}{\partial t} = -\beta n_{\mathrm{e}} n_{\mathrm{p}} \tag{6.34}$$

$$\frac{\partial n_{\mathrm{p}}}{\partial t} = -\beta n_{\mathrm{n}} n_{\mathrm{p}} - \beta n_{\mathrm{e}} n_{\mathrm{p}} \tag{6.35}$$

$$\frac{\partial n_{\mathrm{n}}}{\partial t} = -\beta n_{\mathrm{n}} n_{\mathrm{p}}. \tag{6.36}$$

This system of equations is analytically solvable,

$$n_{\mathrm{e}}(t) = \frac{n_{\mathrm{e}}(t)}{1 + \beta n_{\mathrm{p}}(0) t} \tag{6.37}$$

$$n_{\mathrm{p}}(t) = \frac{n_{\mathrm{p}}(0)}{1 + \beta n_{\mathrm{p}}(0) t} \tag{6.38}$$

$$n_{\mathrm{n}}(t) = \frac{n_{\mathrm{n}}(0)}{1 + \beta n_{\mathrm{p}}(0) t} \tag{6.39}$$

where $t = 0$ at the start of the post discharge regime. It is of interest to compare this calculation to the simulation results presented in Section 6.4.2. This requires the total number of charged particles across the void to be calculated, which in this case is simply

$$N_i = 2 R_{\mathrm{v}} n_i \tag{6.40}$$

as by assumption the charged species have no spatial dependence. The time decay of N_i are shown in Figure 6.19 with $n_{\mathrm{p}}(0)$, $n_{\mathrm{e}}(0)$ and $n_n(0)$ set to 1×10^{19} m^{-3}, 0.9×10^{19} m^{-3} and 0.1×10^{19} m^{-3} respectively, which are typical values for number densities based on the simulation results. As can be seen, the plasma cloud in the void undergoes a rapid

reduction for the first 0.01 ms followed by a more gradual decay and it is still present after 0.2 ms if recombination is considered in isolation.

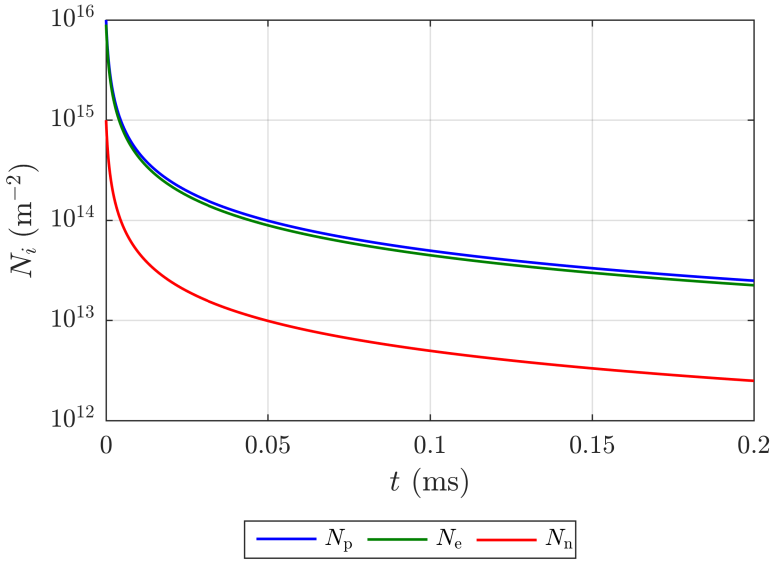

FIGURE 6.19: Figure showing analytical solution of charged species dynamics after a discharge subject only to recombination.

The other process to consider is charge deployment into the dielectric boundary due to the varying applied electric field. As was stated previously for the sake of simplicity recombination processes will now be neglected in this treatment and the impact of charge deployment alone will be considered. Under the assumptions previously introduced, for a one dimensional case with an air gap of size $2R_\mathrm{v}$ centred at the origin between parallel plates with separation L_plate covered by an insulation with relative permittivity $\varepsilon_{r\,\mathrm{i}}$, E_0 and E_σ can be calculated exactly as

$$E_0(t) = \begin{cases} \dfrac{-V_0(t)\varepsilon_{r\,\mathrm{i}}}{L_\mathrm{plate} - 2R_\mathrm{v} + 2R_\mathrm{v}\varepsilon_{r\,\mathrm{i}}} & |x| < R_\mathrm{v} \\ \dfrac{-V_0(t)}{L_\mathrm{plate} - 2R_\mathrm{v} + 2R_\mathrm{v}\varepsilon_{r\,\mathrm{i}}} & |x| > R_\mathrm{v} \end{cases} \tag{6.41}$$

and

$$E_\sigma(t) = \begin{cases} \dfrac{-\sigma_\mathrm{top}(t)(L_\mathrm{plate} - 2R_\mathrm{v})}{\varepsilon_0(L_\mathrm{plate} - 2R_\mathrm{v} + 2R_\mathrm{v}\varepsilon_{r\,\mathrm{i}})} & |x| < R_\mathrm{v} \\ \dfrac{2R_\mathrm{v}\sigma_\mathrm{top}(t)}{\varepsilon_0(L_\mathrm{plate} - 2R_\mathrm{v} + 2R_\mathrm{v}\varepsilon_{r\,\mathrm{i}})} & |x| > R_\mathrm{v} \end{cases} \tag{6.42}$$

where the surface charge density is σ at R_v and $-\sigma$ at $-R_\mathrm{v}$. Setting $E_\sigma = -E_0$, (6.33), inside the void means

$$-\sigma(t)(L_\mathrm{plate} - 2R_\mathrm{v}) = V_0(t)\varepsilon_{r\,\mathrm{i}}\varepsilon_0 \tag{6.43}$$

which can be solved for σ

$$\sigma(t) = \frac{-V_0(t)\varepsilon_{r\,\mathrm{i}}\varepsilon_0}{(L_\mathrm{plate} - 2R_\mathrm{v})}. \tag{6.44}$$

Substituting values for system considered in Section 6.4.2, with the applied voltage set to its value at the discharge, $V_0(t_\mathrm{PD}) = U_0 \sin(\omega t_\mathrm{PD}) = -9$ kV, $\varepsilon_{r\,\mathrm{i}} = 4.4$, $L_\mathrm{plate} = 2$ mm and $R_\mathrm{v} = 0.5$ mm, results in $\sigma(t_\mathrm{PD}) = 0.35$ nC/mm^2 immediately after the discharge. This is in very close agreement with the values calculated in the simulation, see Figure 6.18, which suggests the assumptions made to this point in the analysis are well founded. It must now be considered how the surface charge density changes due to a changing applied field. It will be assumed the the surface charge is altered, by the influx of charged species from the void, such that zero field in the void is maintained. The total amount of negative surface charge, q^-, available to be deployed at the void surface is then

$$q^- = -e(N_\mathrm{e} + N_\mathrm{n}), \tag{6.45}$$

and the total amount of positive surface charge q^+ is

$$q^+ = eN_\mathrm{p} \tag{6.46}$$

Of course, the polarity of the applied electric field gradient will influence whether positive or negative charge is being deployed into the void boundary. A rising field will be considered here which means that the negative surface charge density at $x = -R_\mathrm{v}$ will have an influx of negatively charged particles, and the positive surface charge density at $x = R_\mathrm{v}$ will have an influx of positively charged particles, see Figure 6.18 a. The falling field case could be considered with trivial rearrangement. Returning to the calculations, by assumption the number densities are uniform across the void, which means the rate of change of the surface charge density can be written as

$$\frac{d\sigma}{dt} = -e\left(\frac{dN_\mathrm{e}}{dt} + \frac{dN_\mathrm{n}}{dt}\right) \text{ at } x = -R_\mathrm{v} \tag{6.47}$$

$$\frac{d\sigma}{dt} = e\frac{dN_\mathrm{p}}{dt} \text{ at } x = R_\mathrm{v}. \tag{6.48}$$

As the evolution of the number densities is of interest, (6.47) and (6.48) can be rewritten using (6.44) as

$$\frac{dN_\mathrm{e}}{dt} + \frac{dN_\mathrm{n}}{dt} = \frac{\varepsilon_{r\,\mathrm{i}}\varepsilon_0}{e(L_\mathrm{plate} - 2R_\mathrm{v})}\frac{dV_0}{dt} \tag{6.49}$$

$$\frac{dN_\mathrm{p}}{dt} = \frac{\varepsilon_{r\,\mathrm{i}}\varepsilon_0}{e(L_\mathrm{plate} - 2R_\mathrm{v})}\frac{dV_0}{dt}. \tag{6.50}$$

For a sinusoidal AC cycle

$$\frac{dN_{\mathrm{e}}}{dt} + \frac{dN_{\mathrm{n}}}{dt} = \frac{\varepsilon_{r\,\mathrm{i}}\varepsilon_0 U_0 \omega}{(L_{\mathrm{plate}} - 2R_{\mathrm{v}})e}\cos(\omega(t + t_{\mathrm{PD}})), \tag{6.51}$$

$$\frac{dN_{\mathrm{p}}}{dt} = \frac{\varepsilon_{r\,\mathrm{i}}\varepsilon U_0 \omega}{(L_{\mathrm{plate}} - 2R_{\mathrm{v}})e}\cos(\omega(t + t_{\mathrm{PD}})) \tag{6.52}$$

solving for all N_i yields

$$N_{\mathrm{p}}(t) = N_{\mathrm{p}}(0) + \frac{\varepsilon_{r\,\mathrm{i}}\varepsilon_0 U_0}{(L_{\mathrm{plate}} - 2R_{\mathrm{v}})e}\left(\sin(\omega(t + t_{\mathrm{PD}})) - \sin(\omega t_{\mathrm{PD}})\right) \tag{6.53}$$

$$N_{\mathrm{e}}(t) = N_{\mathrm{e}}(0) + \frac{N_{\mathrm{e}}(0)\varepsilon_{r\,\mathrm{i}}\varepsilon_0 U_0}{N_{\mathrm{p}}(0)(L_{\mathrm{plate}} - 2R_{\mathrm{v}})e}\left(\sin(\omega(t + t_{\mathrm{PD}})) - \sin(\omega t_{\mathrm{PD}})\right) \tag{6.54}$$

$$N_{\mathrm{n}}(t) = N_{\mathrm{n}}(0) + \frac{N_{\mathrm{n}}(0)\varepsilon_{r\,\mathrm{i}}\varepsilon_0 U_0}{N_{\mathrm{p}}(0)(L_{\mathrm{plate}} - 2R_{\mathrm{v}})e}\left(\sin(\omega(t + t_{\mathrm{PD}})) - \sin(\omega t_{\mathrm{PD}})\right) \tag{6.55}$$

where it has been assumed that the negative charged species, electrons and negative ions, will decay at a rate proportional to the ratio of their initial population. If this assumption is not made it is not possible to solve (6.51) for N_{e} and N_{n} individually. Substituting the conditions present in Section 6.4.2 leads to a decrease (note that $U_0 = -9$ kV is negative) of approximately 10^{14} m^{-2} for N_{p} and N_{e} after 0.2 ms. This decay is approximately linear in time, which can be derived by performing a Taylor expansion on (6.53), (6.54) and (6.55), and noting that t is small compared to the period of the AC cycle. If the decrease due to the influx of charged species at the void boundary is combined with the decrease due to recombination, it would lead to no charge present in the void after 0.2 ms, recovering the result of Section 6.4.2. Of course this is considering each of the processes in isolation, in practice recombination depends on the amount of charged species in the void, which would of course be impacted by the influx losses at the dielectric boundary. It should also be noted that once the amount of charge in the void, q^+ and q^- in (6.46) and (6.45), is insufficient to alter the surface charge to completely oppose the change in the applied field, the assumptions used will be inaccurate. The electric field in the void will start to rapidly rise and once the electric field has risen sufficiently charge deployment into the void boundaries will increase and attachment processes will become significant resulting in all remaining charge being rapidly removed. Spatial gradients in the charged species number densities will also become significant, result in an electric field from the volume charge. Due to the complexity and non-linearity of the governing equations the assumptions required to make them analytically tractable, by necessity, introduce significant simplifications. However, this analysis does offer some insight, in this case the relative impacts of recombination and deployment at the dielectric boundary on the charged species number densities in the post discharge regime are made clear by pursuing analytical solutions.

In the previous section it was shown that the one dimensional model is a good analog of the two dimensional model, as such it can be expected that the results presented in this section are indicative of post discharge dynamics for PD in a range of air gaps. A

robust conclusion that can be drawn from these results is that the plasma cloud present in the void after PD can impact the surface charge at the dielectric boundaries, and that it may be present for ms, rather than microseconds, after a discharge event. The decay of negative charge due to PD on a dielectric surface was observed during the falling field section of an AC cycle, [6], and this model does provide a potential mechanism that could explain this. The two dominant mechanisms by which charge was removed from the air was by deployment into the dielectric boundaries and recombination in the air. As charge deployment could only occur, because the applied field was varying, it may be expected that the time for the plasma cloud to decay in a DC system could be significantly longer. Another important point is that the plasma cloud was completely removed by the decay processes. As such, it seems unlikely that the plasma cloud from a PD could become seed charge for subsequent PDs. This supports the canonical reasoning introduced by Niemeyer, which is that seed charge for subsequent PDs is generated by emission of charge deposited by previous PDs from the dielectric surface [17]. The physical mechanisms of charge emission from dielectric surfaces are not fully understood, and it is beyond the scope of this investigation to consider this phenomena. Instead in the following section, the dynamics of a subsequent discharge are considered which is initialised with the surface charge density at the void surface set to be equal to the surface charge distribution of an earlier discharge.

6.4.3 Effect of Subsequent Discharge

In this configuration the model was initialised with the surface charge density distribution on the void surface set equal to the surface charge density distribution at -9 kV. As was discussed in the previous section, the field created by this surface charge leads to an electric field in void close to zero. In order to initiate PD an applied voltage of -18 kV was used, which means the field in the void is roughly equivalent to the electric fields present in the previous section of discharges in virgin voids, with a distortion caused by the surface charge. This neglects the slight increase in surface charge that would occur due to the plasma cloud, see Figure 6.18a, but it is not thought that this would significantly influence the presented results.

The dynamics of the discharge are similar to the earlier results, the seed charge multiplies and develops into a positive streamer directed towards the top of the void. For brevity plots of the discharge variables are not shown for a range of times. A noticeable difference to the earlier results was observed in the distribution of charge in the streamer head due to the electric field caused by the surface charge already present on the void surface. This led to peak number densities and electric fields being away from the symmetry axis in a toroidal distribution. This is caused to the high field region at the void surface due to the gradient in the surface charge density from the previous discharge. The discharge dependent variables during the initial stage of the positive streamer are shown

in Figure 6.20. It should be noted the toroidal distributions may be due to the use of an axisymmetric model instead of a fully three dimensional model. However, the use of an axisymmetric model is sufficient to explore whether surface charge density from previous PDs is deposited on top of previous PDs, and if the dynamics of the discharge are significantly different in subsequent discharges, which is the purpose of this investigation. If a fully three dimensional model was used it is expected that the plasma dynamics would be that of a positive streamer propagating 'off axis.'

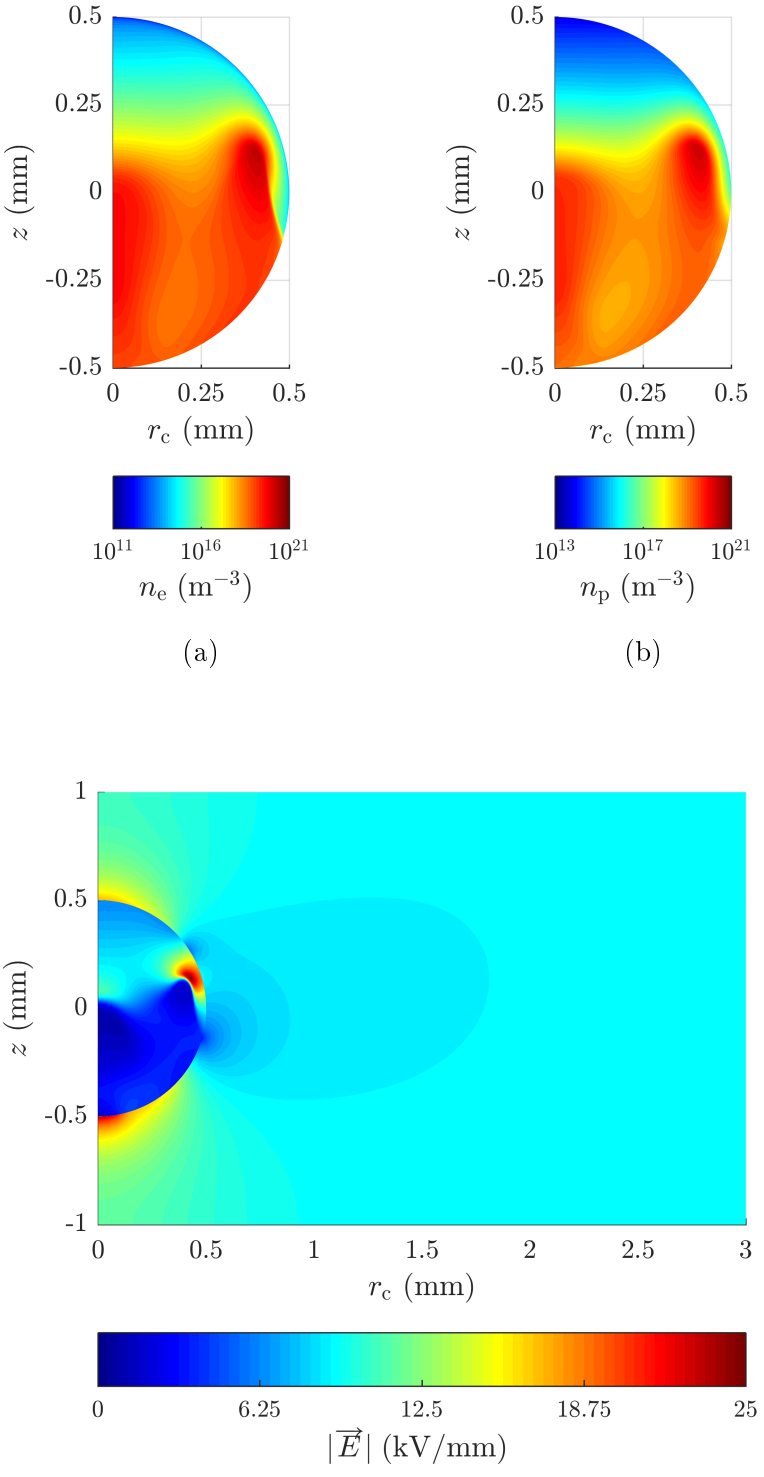

FIGURE 6.20: Discharge dependent variables at 6 ns for the subsequent discharge: (a) electron number density, (b) positive ion number density, (c) electric field magnitude.

The surface charge deployed by the subsequent discharge has a wider distribution, and

it did not sit directly 'on top' of the surface charge already at the void boundary, see Figure 6.21, as is currently assumed in PD activity models [4]. This is because the surface charge from the discharge at -9 kV repelled the charge deposited by the subsequent discharge at -18 kV, which led to a peak surface charge density away from the symmetry axis in the subsequent discharge. The resulting charge distribution was closer to bipolar than the distribution from a single discharge. Measurable quantities for the discharge were similar to the results for virgin voids, with an apparent charge magnitude of 220 pC and an apparent current pulse with a similar shape with a peak current of 100 mA. This is an important result, because although the surface charge density distributions and discharge dynamics were noticeable different, there were not significant differences in the measurable quantities of the discharge.

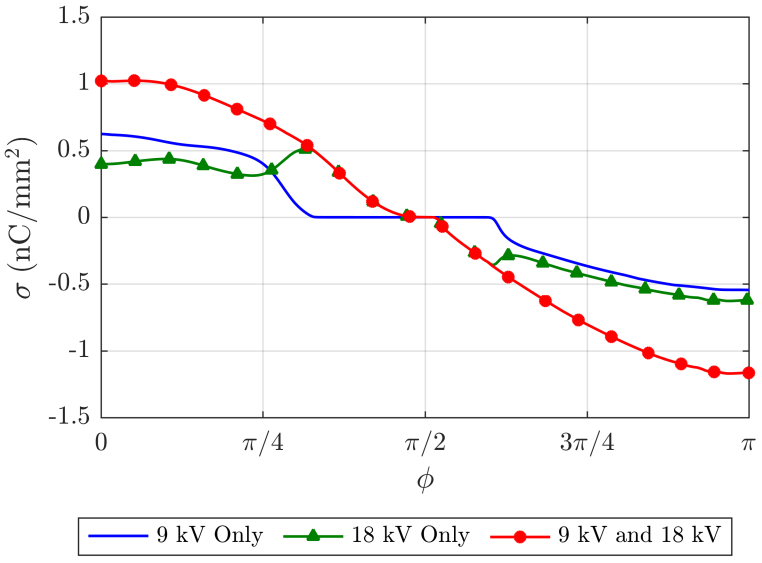

FIGURE 6.21: Surface charge density on the void surface due to the discharge at 9 kV, the subsequent discharge at 18 kV and the resulting distribution.

This final configuration investigated the impact of subsequent discharges. The results were broadly as expected, with the physics of the second discharge comparable to the discharges in virgin voids. However, the charge from the second discharge was not deposited on top of the charge from earlier discharges Instead the charge from the second discharge was more widely distributed due to the electric field from the charge already on the surface opposing its deployment. An interesting point is that although the surface charge density deposited by the second PD was significantly different to the first, the quantities that could be measured experimentally, apparent current and apparent charge, were not significantly different. Previous work in the literature has considered the influence of surface charge density on single PDs, [104], but the surface charge density initially was assumed to have a Gaussian distribution, whereas in this work the surface charge density was set based on the distribution of an earlier discharge.

6.5 Conclusions

A drift diffusion model has been implemented to investigate PDs inside a spherical air filled void. The results from the model display a good agreement to measurements of surface charge density distributions, apparent current pulse shapes and apparent charge magnitudes, and previous numerical simulations [6, 20, 57]. Nevertheless, it should be noted that the model is relatively simplistic compared to a full model containing all plasma chemistry and boundary phenomena, [55, 61, 95, 105], but in spite of this the results provide a test of some of the concepts employed when modelling PD activity. The key contributions of this work as it pertains to PD activity modelling are as follows:

- The surface charge density from PD in spherical voids is not bipolar, a result that has been observed in experimental work [6] and previous simulations for cylindrical voids [57].
- The inception field predicted by the discharge was in reasonable agreement with the formula from the literature. It is advisable that the origins of the inception field equation should be considered when using it to model PD activity.
- After the discharge the electric field in the void is significantly reduced, to around 0.1 kV/mm, which is far lower than the residual field predicted by earlier work [17]. As such the concept that a residual field exists may be erroneous for PD under certain conditions.

The key contributions of this work as it pertains to plasma dynamics are as follows:

- The boundary conditions for the Helmholtz equations, used to calculate the photoionisation rate, can be significantly simplified for the system under consideration to vastly reduce their computational cost.
- A drift diffusion plasma model with swarm parameters was able to reproduce the measurable quantities of PD, namely apparent current and charge.
- The plasma dynamics of PD in spherical air filled voids, at the conditions considered, consist of an electron avalanche transitioning into a positive streamer. This is followed by charge deposition at the void boundary.
- The plasma cloud in the void after PD activity may influence the surface charge distributions from the discharge itself and may persist in the void for milliseconds after the PD event.
- A subsequent discharge was found to have similar dynamics to the discharges in virgin voids, with comparable measurable quantities. However, the peak charged species number densities and electric fields of the discharge were reached 'off axis'

due to the enhancement of the electric field from the surface charge on the void surface from the previous discharge.

There a range of investigations that can be considered using this drift diffusion model. In the next section the results of a preliminary investigation into the discharge dynamics under step applied voltages, which are used in impulse waveforms, are presented. It is worth recognising that current PD activity models, such as that introduced in Chapter 3, cannot adequately consider such a system.

6.6 Further Work on Partial Discharge under Step Applied Voltages

PD activity due to impulse voltage waveforms has recently received increased research attention [106, 107]. This was due to the premature failure of a equipment that used these waveforms, in particular inverter-fed motors [108]. Investigations showed that PDs due to these waveforms have a higher apparent charge than PD under AC conditions, and it is thought that this may accelerating ageing processes leading to earlier failure of high voltage plant [107, 109]. For simplicity and speed a one dimensional case is considered which is designed to approximate the experimental setup in [106]. The waveforms under consideration have fall times of the order µs, but can have rise times of the order ns. For the purposes of modelling the discharge, the rise and fall of the waveform can therefore be treated independently, with the focus here being on rising step. This section is a very brief preliminary investigation and demonstrates the possibilities of using drift diffusion plasma models to investigate PD systems.

The model is designed to approximate the experimental setup in [106]. In this work, discharges take place between two crossed wires, each covered with 50 µm of polyamide-imide enamel. The discharge was assumed to occur in a 0.2 mm air gap. The geometry is shown in Figure 6.22, the central region, where the discharges takes place, is considered to be air, $\varepsilon_r = 1$, and the end regions polyamide-imide enamel, $\varepsilon_r = 3.6$. The high voltage electrode is at $x = 0.15$ mm, and the ground electrode is at $x = -0.15$ mm. The governing equations and boundary conditions are identical to those presented in Section 6.3.

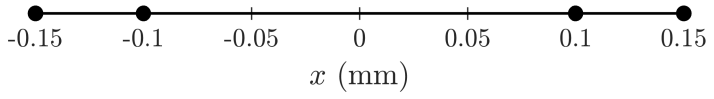

FIGURE 6.22: Model geometry used to investigate discharge dynamics due to step applied voltages.

The voltage waveform in the experiment has a 20 ns rise time with a magnitude of 1 kV. As there will be some field enhancement at the contact point in the experiment, which cannot be captured in a one dimensional model, the voltage waveform in the model has a magnitude of 2 kV. Three cases are considered, in each case at the start of the simulation a Gaussian seed of charge centred at $x = 0.1$ mm is used to initiate the discharge. The cases considered are as follows:

1. DC - The high voltage electrode is set to -2 kV for the whole simulation.
2. 2 kV 20 ns Step from 0 kV starting at 0 ns - The high voltage electrode is initially set to 0 kV, at 0 ns the applied voltage is raised to 2 kV over 20 ns.
3. 2 kV 20 ns Step from 0 kV starting at 10 ns - The high voltage electrode is initially set to 0 kV, at 10 ns the applied voltage is raised to 2 kV over 20 ns.
4. 4 kV 20 ns Step from 2 kV starting at 0 ns - The high voltage electrode is initially set to -2 kV, at 0 ns the applied voltage is raised to 2 kV over 20 ns.
5. 4 kV 20 ns Step from 2 kV starting at 10 ns - The high voltage electrode is initially set to -2 kV, at 10 ns the applied voltage is raised to 2 kV over 20 ns.

Each case is run for a total time of 200 ns, the applied voltages are shown in Figure 6.23.

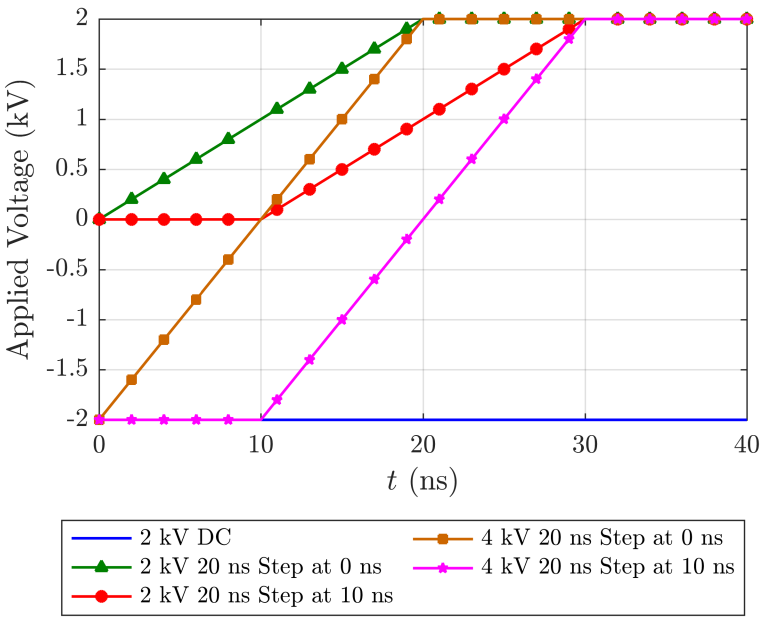

FIGURE 6.23: Figure showing the applied voltages considered.

The main variables of interest for analysing PD activity are the apparent current and the apparent charge. As the model is one dimensional, the apparent currents and charges

of the discharges cannot be calculated explicitly. Instead relative values are given, with the maximum apparent current and charge of the DC discharge set to 1. It should be noted that the apparent current due to the step applied voltage has been removed in the calculation, the current pulses displayed are due to discharge dynamics alone. The relative apparent current and apparent charge for each case are shown in Figure 6.24 and Table 6.5 respectively.

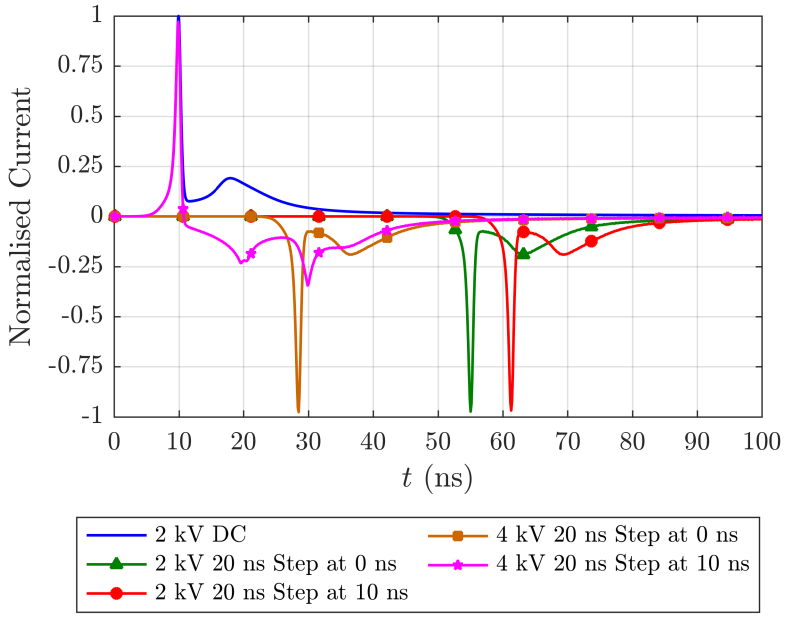

FIGURE 6.24: Figure showing relative apparent current for discharges under step voltages.

Case	Relative Apparent Charge
DC discharge	1
2 kV 20 ns Step at 0 ns	-1
2 kV 20 ns Step at 10 ns	-1
4 kV 20 ns Step at 0 ns	-1
4 kV 20 ns Step at 10 ns	-1

TABLE 6.5: Relative Apparent Charge for Discharges under Step Voltages

The DC discharge exhibited the expected physical phenomena with an electron avalanche transitioning into a positive streamer. For cases 2-4 the same dynamics were observed after a significant time delay. This is because that for this arrangement 2 kV is just above the inception voltage of the air gap. Below this voltage the initial Gaussian seed of discharge undergoes recombination in the air. Therefore for these step voltages once the inception voltage is reached there is very little free charge left in the air, and it takes

time until the charge magnitude has increased significantly to initiate the discharge. When the discharge was initiated the applied voltage was constant and as such the dynamics are equivalent to the DC case. Novel dynamics were observed in case 5, a 4 kV 20 ns step from 2 kV starting at 10 ns. This is because the positive streamer had already developed when the voltage step was reached, leading to a reversal in the direction of the positive streamer. This led to two negative current pulses, see Figure 6.24, due to the interaction of the streamer with the surface charge.

For the cases considered so far the magnitudes of PD are unaffected by the step voltage. Simply put, the discharge deposits charge such that the applied field is shorted out, variation in the applied field during the discharge, such as the step voltages considered in this work, do not impact the overall magnitude of the discharge. The reason for the higher magnitudes observed in experiments may be that in the experiment applied field is significantly higher than the inception field, and therefore during the voltage rise multiple discharges can take place in quick succession. It might also be the case that the experimental measurements are being erroneously influenced by the current produced by the step voltage itself, which could lead to higher magnitudes at shorter rise times. Furthermore, discharges during the impulse may produce currents with opposing polarities, which may impact measurements. The results presented here are likely to be heavily dependent on the air gap size, air pressure and voltage waveform profiles. Quantifying the influence of these parameters will require further investigation.

Chapter 7

Overview, Conclusions and Future Work

This chapter concludes the thesis. A discussion of the work undertaken is provided, with a summary of important conclusions. Possible directions of further research are also discussed.

7.1 Overview

The aim of this thesis was to improve the state of the art in modelling PD activity in gaseous voids. From a detailed literature survey it became apparent that there are limitations with current PD models, and a new model was developed with the aim of trying to fix some of the shortcomings in earlier work.

The new model considers the inception of a discharge and the electron generation processes at a range of locations in the PD system. Previous models assumed that these processes were governed by the electric field at a single point in the system. This is thought to be more physical description of the system. In order for the PD model to reproduce the 'rabbit ear' PRPD patterns it is necessary to develop improve the model of electron detrapping. Based on measurements and modelling of charge detrapping in the literature, [83], it was decided to split the detrappable electron population between two trap depths. This is different to other approaches in the PD modelling literature, where it was concluded that either charge detrapping was dependent on the polarity of the surface charge [4, 17], or that the effective work function of the surface is altered due to discharge events [45]. However, neither of these approaches are based on experimental evidence, whereas the existence two electron trap depths, while not investigated in PD systems, has been shown as an effective method of modelling charge detrapping [83, 84]. Surface charge density distributions due to discharge activity in an earlier Poisson PD

model were considered to be discrete, [4], which leads to discontinuities in the electric field at the surface. In this work the distributions were continuous, using logistic functions, which avoids discontinuities and is in approximate agreement with measurements of surface charge density from discharge activity in the literature [5, 6, 7]. The technique of splitting the electric field into local and applied components was also introduced to dramatically reduce the computational cost of the model. While this is not a contribution as such, it appears that other FEA models of PD activity have solved for the electric at all time steps, which is in general unnecessary if this approach is used.

The model was then validated against experimental work in the literature by simulating PD activity in a spherical air void surrounded by epoxy resin. The potential influence of void deformation on PD activity was then investigated using the model [11]. Measurements taken during sustained discharge activity for a spherical void in silicone rubber were also considered [12].

Following this it was decided to see if the model could provide insight into more complex three-phase cable experiments. It was found that PD activity from an artificial spike defect on a ferrule in a three phase cable joint could be investigated, [13], but in many of the other experiments the PD activity was so complex that a large number of assumptions would be required a priori, which would significantly limit the models insight. The potential impact of the elliptical applied field in three phase cables on PD activity was also investigated using the model [14].

It became increasingly clear over the course of the project that the current implementation of PD activity models are insufficient to make detailed physical insight on the physics of discharges. A particular problem is that a number of the fundamental assumptions have limited justification, combined with the fact that the models require numerous free parameters, even after attempts have been made to minimise their number. As a result, it was decided to implement a simple drift diffusion plasma model to investigate single discharges in a spherical air void to investigated some of the key assumptions and concepts used in PD modelling. The results demonstrated that many of the assumptions made in PD activity models may be spurious.

7.2 Conclusions

The findings of this thesis can be split between the results obtained using the PD activity model, developed in Chapter 3, and those obtained using the drift diffusion model, introduced in Chapter 6.

7.2.1 Partial Discharge Activity Model

The PD activity model was validated by reproducing a 'rabbit' ear PRPD pattern. This was achieved using 4 free parameters to fit the model to the experiment, whereas in earlier work 8 were employed [4]. This demonstrates that the number of free parameters that are used when modelling PD activity may be unnecessarily high, and highlights the need to minimise the number free parameters where possible. The hypothetical impact of void deformation on PD activity was then investigated [11]. It was shown that even relatively minor changes to the void geometry, with all other physical conditions kept constant, could significantly influence PD activity. For the type deformation considered, the number of PDs per AC cycle increased with the severity of the deformation, in addition to significant changes in PRPD patterns.

PD measurements taken at intervals over a period of sustained discharge activity were also investigated using the PD model [12]. The complexity of the data sets meant that only an approximate fit could be achieved. This discrepancy is thought to be due to the physical processes taking place in the void resulting in a system which violates some of the assumptions which are necessary to preserve model simplicity. The tentative conclusions that can be made are that sustained discharge activity will alter the gaseous composition of the void and lower the inception electric field. It also appears that the by-products on the surface of the void can impact charge detrapping processes, with significant changes to the rate of decay of the detrappable charge population. It also appears that the decay of charge on the void surface plays a more significant role as the void surface is damaged.

The model was then employed to investigate more complex PD experiments in three-phase PILC cable joints [76]. Two experiments were considered, in the first a spike was placed on the ferrule of phase two during joint construction. For the second experiment, a large air void was created in the joint by not completely filling the lead capsule with bitumen. The second experiment was not found to be permissible to modelling due to the large number of unknowns, such as the number of possible discharge channels and the dimensions of the void, which would have to be assumed in a PD model. This is an important point, as it demonstrates that without additional information for many PD systems it is not possible to model discharge activity.

The spike on ferrule experiment was found to be permissible to modelling [13]. A simplified model geometry was developed from the experimental arrangement, and PD activity was assumed to be due to air trapped in a spherical void in the vicinity of the spike tip. The radius of the spherical void that was found to fit the experimental data was 2 mm, indicating that the presence of the spike has caused significant damage to the Crêpe paper to trap this volume of air close to phase two. It is also interesting that an empirical fit used for the electron generation rate of a needle-plane system, [79], could be successfully applied to a metallic spike under different conditions. The model was also sensitive to changes in phase energisation and the applied voltage waveform. The results suggest that

the applied voltage input should be closely monitored during PD experiments and that measurements are taken under rated volts with the same phase energisation as operating conditions.

7.2.2 Drift Diffusion Model

The drift diffusion model was capable of reproducing the measurable quantities of PD without requiring any assumptions a priori. The apparent current is in good agreement with experimental measurements, with a rapid rise followed by a slower decay with a pulse in the time scale of nanoseconds [20]. The apparent charge is in line with experimental measurements [4]. Furthermore, the surface charge density distributions agree with Pockels cell measurements [6]. This suggests that the model is representative of reality.

The inception field equation, (4.10), is in reasonable agreement with the model, with the model predicting a PD inception field approximately 1 kV/mm higher. It should be realised that the inception field equation is developed from experimental data for large air gaps between metallic electrodes, [41], and as such might not be appropriate for a large number of PD systems. A notable discrepancy with the established reasoning was found with respect to the residual electric field. Instead of dropping to a residual value after a discharge the electric field is nearly completely 'shorted out' in the systems considered.

The surface charge density distributions can be considered as positive and negative charge spots, although the distribution is not bipolar, a result that has been observed in experimental work [6] and previous simulations in cylindrical voids [57]. Furthermore the distribution of surface charge from a discharge is dependent on the surface charge distributions already present on the surface. This means that surface charge density dynamics due to discharge activity are significantly more complicated than that assumed in PD activity models.

The decay of charge in air is not exponential, as was proposed in Niemeyer's work [17]. For the conditions considered plasma remained in the air for approximately 0.2 ms after the discharge. The processes leading to the decay of charged particles were a combination of recombination in the air and deployment as surface charge at the dielectric boundary due to the varying applied voltage.

The plasma dynamics of PD in spherical air filled voids, at the conditions considered, consist of an electron avalanche transitioning into a positive streamer. A subsequent discharge was found to have similar dynamics to the discharges in virgin voids, with comparable measurable quantities. However, the peak charged species number densities and electric fields of the discharge were reached 'off axis' due to the enhancement of the electric field from the surface charge on the void surface from the previous discharge.

7.2.3 Summary

Moving forward it may be possible to build on the findings from the drift diffusion model to develop an improved PD activity model. In particular, a drift diffusion model allows surface charge density distributions from PDs can be calculated explicitly instead of the assumed distributions currently used. However, an important part of discharge activity which the drift diffusion model offers no insight into is the initial generation of first free electron. Although this may be a fundamentally stochastic process, the probability of generation is likely to be dependent on conditions such as trap depth, electric field and temperature, which is only crudely considered when using (3.13). There is not presently a comprehensive understanding of these processes in PD systems, and further investigation is required.

Despite the improved PD activity models that may be possible in the future, it may well be the case that modelling PD activity accurately will remain unfeasible for a range of systems. As mentioned previously, an obvious example would be the complex and noisy PD activity measured in three-phase cable experiments and field based measurements, [76]. However, even in simpler systems, simulating PD activity accurately can be exceptionally difficult. For example, consider the measured PD activity from a spherical void in silicone rubber, shown in Figure 7.1. The discharge activity shows a range of PD magnitudes for the first 320 s, followed by a rapid reduction in PD activity. It is at present not possible to accurately predict when, or why these sudden changes in PD activity will occur and it is likely that simulating these changes in discharge activity will remain beyond the scope of PD activity models.

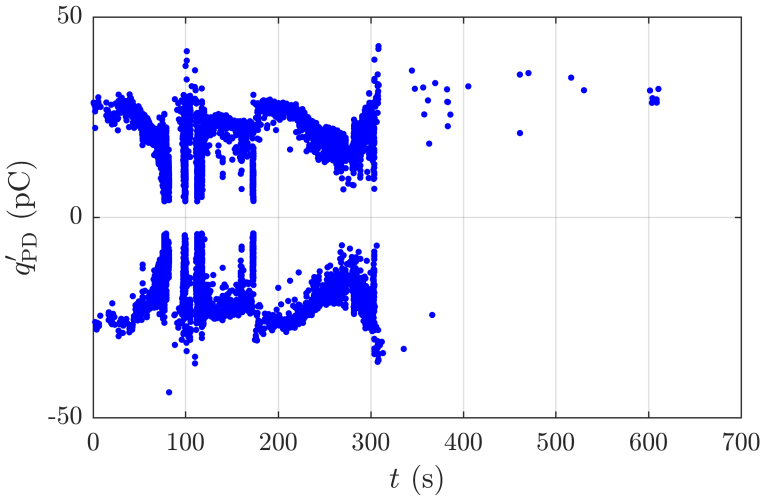

FIGURE 7.1: PD activity from a spherical air void in silicone rubber between parallel plate electrodes. Used with permission from the experimental work conducted for [12].

In conclusion, the work conducted in this thesis has shown that PD activity models can offer some limited insight into PD systems. However, there are a number issues with the assumptions and simplifications used in these models. This was shown using a drift diffusion plasma model to investigated discharge physics in greater detail. Moving forward, it may be preferable to use drift diffusion plasma models to investigate PD, and there a range of interesting cases to consider in future research.

7.3 Future Work

Plasma models can simulate discharges will high accuracy, and in the future may be able to predict damage by calculating the electron energy and by considering chemical reactions in the air and at the dielectric surface. From an engineering standpoint, it may be that it is of more interest to develop more complex but physically accurate models of single discharges instead of simplistic models of many discharges, which can offer limited physical insight into a system as previously discussed. This is because plasma models have the ability, in theory, to predict the paths that discharges might take, where they can occur in a system, and the potential damage they might do to a dielectric material [59].

Building directly on this work, it would be interesting to see how the surface charge distribution varies due to numerous PDs across a number of AC cycles. To fully investigate this it may be required to develop a fully three dimensional model, which will significantly increase the computational cost. It would also be of interest to extend the work in Section 6.6 and see how impulse or high frequency applied voltage wave forms impact the discharge physics in two dimensional axisymmetric geometries. Another interesting investigation would be to see if different discharge mechanisms become prevalent if the physical parameters of the void are altered. It has been observed that the discharge mechanisms for discharges in cylindrical air filled voids in LDPE changed due to sustained discharge activity [20, 25]. It is clear that plasma models of PD can make a contribution to numerous investigations that may be considered in the future.

Appendix A

Notation

In the interests of clarity the author has developed a notation style, used in Chapters 2 to 5, to denote differences between physical constants, variables and parameters. The explicit dependency of variables on other variables and parameters is shown by separating variable and parameter arguments with a semi-colon. The subscript "PD" is used to refers to parameters or variables that only have meaning during discharge events.

As an example consider the surface charge density from the ith PD, $\sigma_{\mathrm{PD}\,i}$

$$\begin{aligned}\sigma_{\mathrm{PD}\,i}(\vec{x}_{\partial G_\mathrm{v}}, \vec{x}^{+}_{\partial G_\mathrm{v}\,\mathrm{PD}\,i}, \vec{x}^{-}_{\partial G_\mathrm{v}\,\mathrm{PD}\,i}, \alpha_{\mathrm{PD}\,i}; \lambda_{\mathrm{PD}}, \eta_{\mathrm{PD}}) \quad &= \quad \ldots \\ \underbrace{\frac{\alpha_{\mathrm{PD}\,i}}{1+\exp\left(\eta_{\mathrm{PD}}\left[d_\mathrm{v}\left(\vec{x}_{\partial G_\mathrm{v}}, \vec{x}^{+}_{\partial G_\mathrm{v}\,\mathrm{PD}\,i}\right) - \lambda_{\mathrm{PD}}\right]\right)}}_{\text{Positive Charge Spot}} - \quad &\ldots \\ \underbrace{\frac{\alpha_{\mathrm{PD}\,i}}{1+\exp\left(\eta_{\mathrm{PD}}\left[d_\mathrm{v}\left(\vec{x}_{\partial G_\mathrm{v}}, \vec{x}^{-}_{\partial G_\mathrm{v}\,\mathrm{PD}\,i}\right) - \lambda_{\mathrm{PD}}\right]\right)}}_{\text{Negative Charge Spot}}, &\end{aligned} \tag{A.1}$$

The PD subscript means that σ_{PD} is only relevant during discharges, because it is the charge distribution from a single PD. Taking each argument of $\sigma_{\mathrm{PD}\,i}$ in order:

1. $\vec{x}_{\partial G_\mathrm{v}}$ are spatial coordinates on the void surface, a variable.
2. $\vec{x}^{\pm}_{\partial G_\mathrm{v}\,\mathrm{PD}\,i}$ are spatial coordinates at the points on the void surface where the positive and negative charge spots of the ith PD are centred. It is therefore a variable, that can only be applied during PD events, hence the PD subscript.
3. $\alpha_{\mathrm{PD}\,i}$ is the magnitude of the surface charge density of the charge spots, it will varying between discharges. It is therefore a variable, that can only be applied during PD events, hence the PD subscript.

4. $\lambda_{\mathrm{PD}}, \eta_{\mathrm{PD}}$ specify the distribution of surface charge density, they do not change through the simulation. They are therefore parameters and can only be applied during PD events, hence the PD subscript.

5. d_{v} is the distance between two points on the void surface, its arguments, $\vec{x}_{\partial G_{\mathrm{v}}}, \vec{x}^{\pm}_{\partial G_{\mathrm{v}}\,\mathrm{PD}\,i}$, are also shown for clarity.

Appendix B

Distributing Points Evenly on a Surface

When implementing the PD model it is often required to distribute points evenly across a given surface. This is not a completely trivial problem and in this appendix the relevant calculations are provided for the different cases considered in this work.

B.1 Distribution of Points on a Spherical Surface in an Axisymmetric System

In an axisymmetric system each point on the surface of the void represents a circle in three dimensional space. The aim is to distribute these circles such that an equal area $A/2N$ can be associated with each circle, where N is the number of circles. The approach taken here is to distribute the circles such that two regions, each of size $A/2N$ could be associated with each circle with one above it and one below it. This is shown in the schematic in Figure B.1.

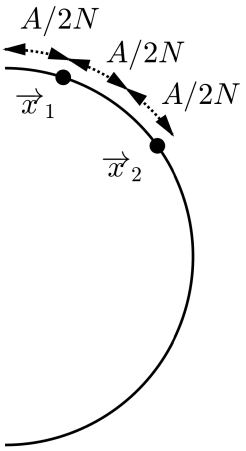

FIGURE B.1: Schematic of evenly distributed points on a sphere in an axisymmetric system.

The first circle will therefore have a polar angle of ϕ_1 where

$$A/2N = \int_0^{\phi_1} 2\pi R_{\mathrm{v}}^2 \sin(\phi)\, d\phi. \tag{B.1}$$

$A = 4\pi R_{\mathrm{v}}^2$, where R_{v} is the radius of the sphere, so B.1 can be solved for ϕ_1

$$\phi_1 = \arccos\left(1 - \frac{1}{N}\right). \tag{B.2}$$

The remaining points can then be calculated in an iterative fashion as

$$\phi_i = \arccos\left(\cos(\phi_{i-1}) - \frac{2}{N}\right). \tag{B.3}$$

B.2 Distribution of Points on an Axisymmetric Surface in an Axisymmetric System

For an arbitrary axisymmetric surface it is not in general possible to perform the necessary calculations analytically. Instead, the relevant integrals are implemented and solved numerically in MATLAB. It will be assumed that the axisymmetric surface can be parameterised by the polar angle ϕ as

$$r_{\mathrm{c}} = R(\phi)\sin(\phi) \tag{B.4}$$

$$z = R(\phi)\cos(\phi). \tag{B.5}$$

The surface area of the surface A, is then calculated numerically through

$$A = \int_0^{\pi} 2\pi R \sin(\phi) \sqrt{R^2 + \left(\frac{dR}{d\phi}\right)^2}\, d\phi.$$

By calculating how the surface area varies as a function of polar angle, it is possible to calculate the appropriate polar angles for the evenly spaced points such that an area of A/N can be associated with each point. This was the approach used to determine the generation points for the deformed void in Section 4.9.

B.3 Distribution of Points on a Spherical Surface in a Three Dimensional System

This cannot be achieved analytically except for very specific cases with a relatively small number of points, but there are numerous methods that give distributions which are a good approximation. The approach applied here is a Fibonacci grid algorithm. Using this method, the Cartesian coordinates of N approximately evenly spaced points on a unit sphere centred at the origin is

$$\vec{x}_i = \begin{pmatrix} x_i \\ y_i \\ z_i \end{pmatrix} = \begin{pmatrix} \frac{2i}{N} - 1 \\ \sqrt{1 - x_i^2}\sin\left((i+1)f_1\right) \\ \sqrt{1 - x_i^2}\cos\left((i+1)f_1\right) \end{pmatrix} \tag{B.6}$$

where $i = 1, 2, ..., N$ and $f_1 = \pi(3 - \sqrt{5})$. A plot of $\vec{x}_i$ is shown for $N = 1001$ in Figure B.2.

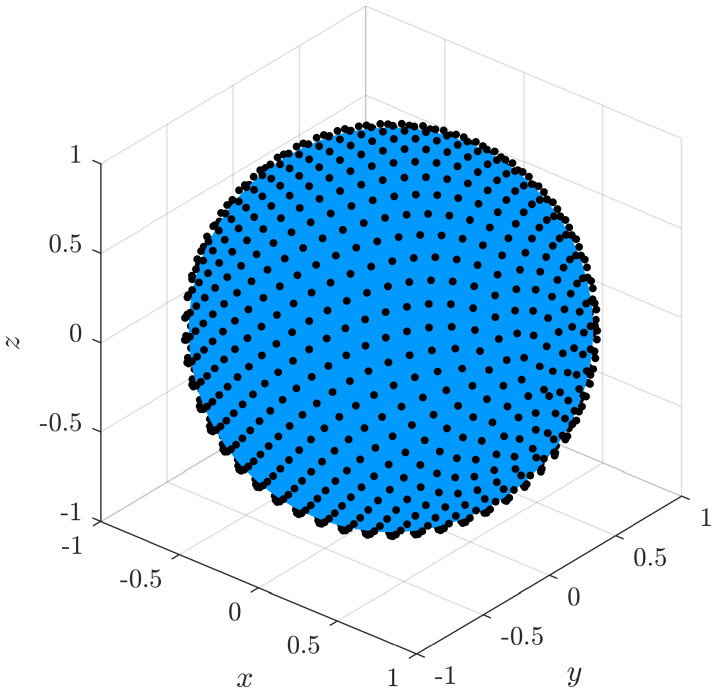

FIGURE B.2: Figure showing 1001 points on a unit sphere, distributed using a Fibonacci grid algorithm.

Appendix C

Verifying Plasma Model Implementation by Omitting Secondary Processes

In order for positive streamers to propagate through air, it is required that seed electrons are available ahead of the ionising wave [24]. Based on the configuration of charged particles in a positive streamer the only mechanisms by which seed electrons can be generated ahead of the ionising wave are photoionisation, or secondary emission from the boundaries with the dominant process for the system under consideration here being photoionisation. Therefore if secondary processes are omitted a positive streamer should not form, because there is no mechanism to propagate the ionising wave. This can be used as a check of the model implementation, because the stabilisation techniques used by COMSOL introduce artificial numerical diffusion to 'smooth' sharp spatial gradients. If this artificial diffusion is sufficiently large there would be seed electrons ahead of the ionising wave in the simulation as a numerical error. Therefore it is proposed to run the same model introduced in Chapter 6, with the ion impact emission and photoionisation processes omitted. Both the one and two dimensional models introduced in Chapter 6 were used in this work. It should be realised that the results presented in this chapter are a check of the model implementation. They are not representative of reality as physical processes are deliberately omitted.

C.1 Two Dimensional Model

The two dimensional model was run for 30 ns with applied voltages of -9 kV and -9.5 kV with secondary processes omitted. By constrast when secondary processes were included at these applied voltages, positive streamers were formed within 15 ns, see Chapter 6. However, when the secondary processes were omitted the plasma dynamics

were significantly different. The results are shown for −9 kV applied voltage, for brevity, the dynamics observed with the applied voltage at −9.5 kV were equivalent.

The initial stage of the discharge began with an electron avalanche, with the Gaussian seed charge undergoing multiplication and falling to the bottom of the void within the first 5 ns, see Figure C.1. The space charge was sufficient to alter the electric field, but not significantly, see Figure C.1 c. This is very similar to the plasma dynamics observed when the secondary processes were included and is as expected, because the avalanche is driven by the primary process of collisional ionisation. However, it should be noted that there are regions of the void where the number density is very low, such that it cannot really be regarded as a physical number density, because there is no photoionisation which acts 'at a distance' to generate electrons and positive ions. The stage following the electron avalanche was significantly different to the dynamics observed with secondary processes included. A transition from an avalanche to a positive streamer did not occur and charge deployment into the dielectric boundaries began with a reduction in the space charge in the void between 10 ns and the end of the simulation at 30 ns. The electron number densities were found to undergo the quickest reduction due to the fact they have a higher drift velocity compared to ions. This led to a complete removal of electrons from the void by 30 ns, see Figure C.2 a. As a result of their lower drift velocity a significant number of positive and negative ions were still left in the void at 30 ns, with the number densities undergoing a more gradual decay. This agrees with previous investigations of the post discharge stage, where the removal of electrons from the void is faster than ions at high electric fields, see Figure 6.17.

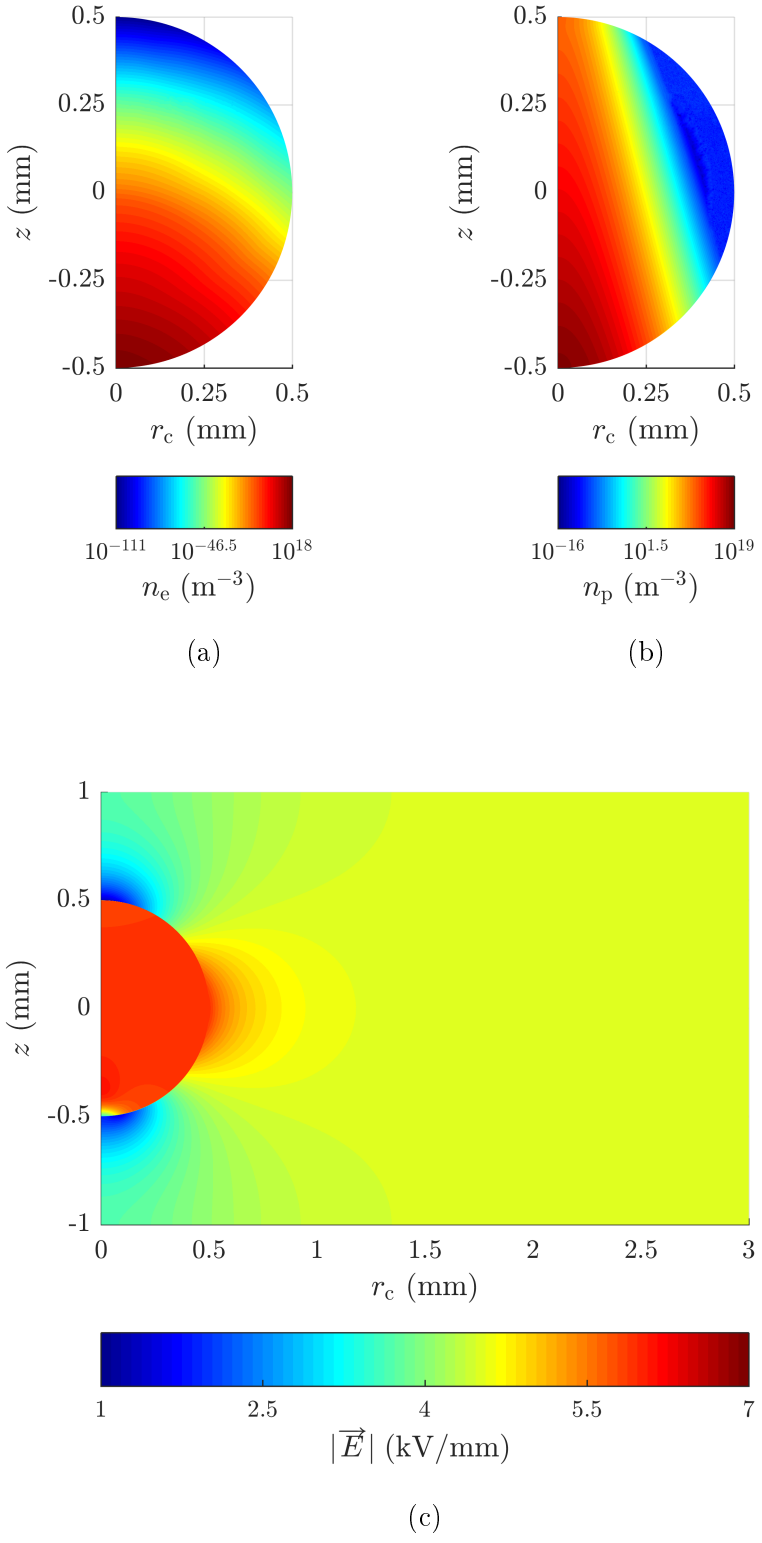

FIGURE C.1: Discharge dependent variables at 5 ns with secondary processes neglected: (a) electron number density, (b) positive ion number density, (c) electric field magnitude.

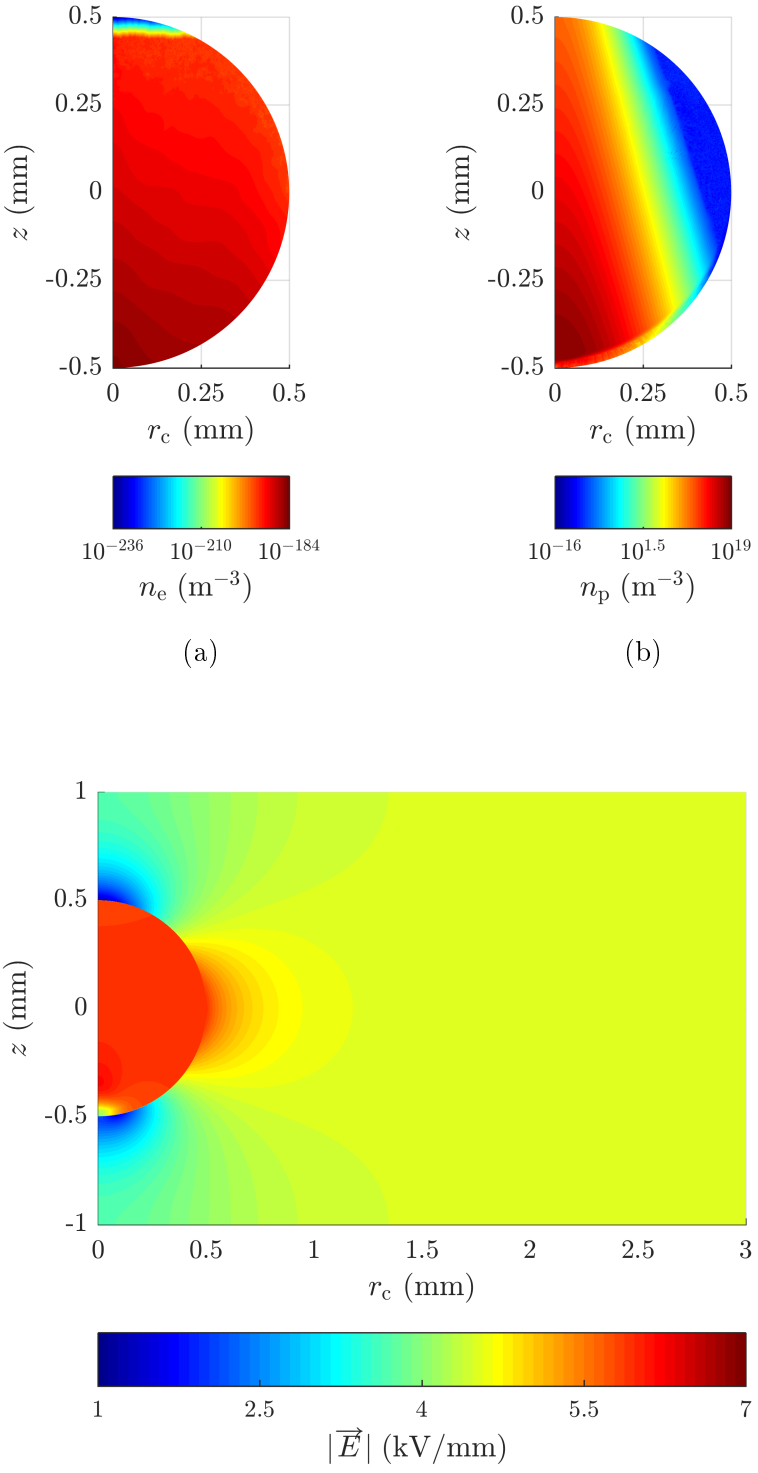

FIGURE C.2: Discharge dependent variables at 30 ns with secondary processes neglected: (a) electron number density, (b) positive ion number density, (c) electric field magnitude.

At 30 ns when the simulation was completed the surface charge density consisted of

a negative charge spot, due to the influx of electrons, at the bottom of the void, see Figure C.3. It is expected that if longer timescales were considered the surface charge density distribution would become approximately bipolar, with a peak surface charge density in the order of 0.1 nC mm^{-2} which is an order of magnitude lower than the surface charge density distribution observed with secondary processes included, see Figure 6.9.

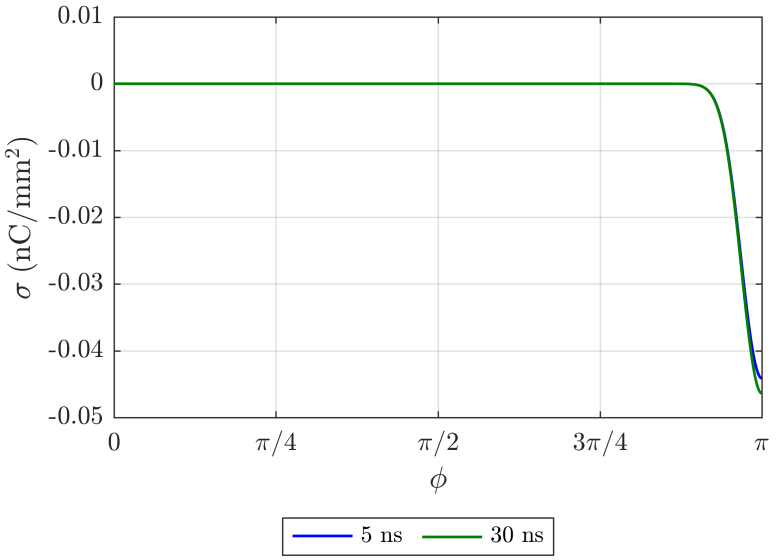

FIGURE C.3: Surface charge density distribution at the void boundary with secondary processes neglected at different times.

C.2 One Dimensional Model

Due to its low computational cost the one dimensional model allows longer timescales and alternative scenarios to be considered. The one dimensional model was run with an applied voltage of -9 kV, which is significantly above the PD inception voltage of -7 kV. In order to assess the significance of photoionisation in plasma dynamics the model was run with photoionisation included, but scaled by an order of magnitude factor. The surface charge density at the void boundaries for the factors of 0.1, 1 (the correct value of photoionisation) and 10 are shown in Figure C.4. The discharge shows similar dynamics, with the surface charge density moving as a scaled curve due to the order of magnitude changes. In all cases the dynamics consisted of an electron avalanche transitioning into a positive streamer. This agrees with existing work in the literature where it was concluded that some inaccuracy in the calculation of photoionisation will impact the initial stages of the discharge, but will not significantly influence the propagation of the streamer [101].

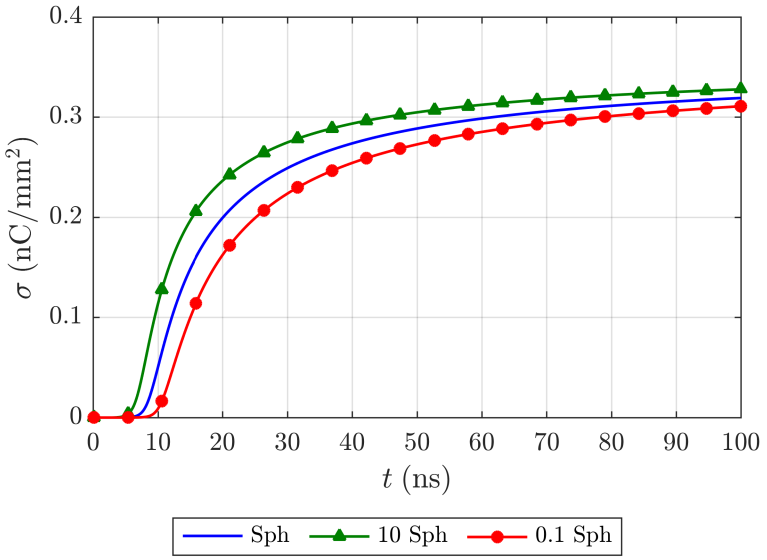

(a)

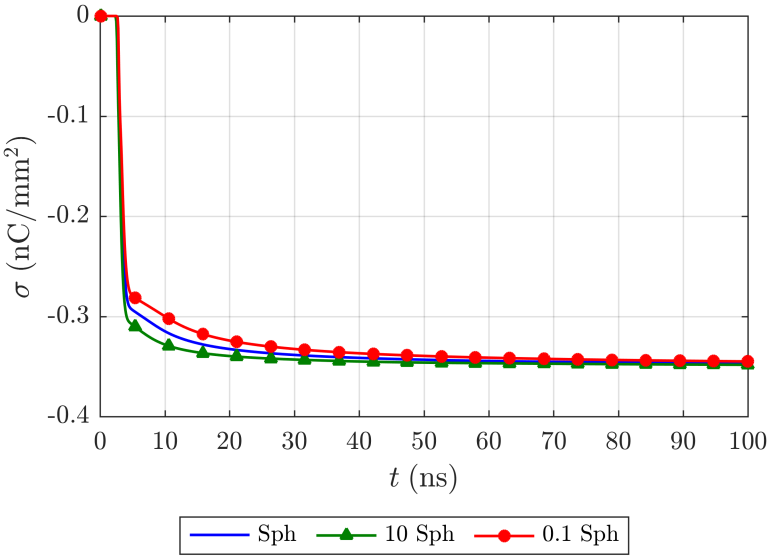

(b)

FIGURE C.4: Surface charge density dynamics in the one dimensional model with photoionisation scaled over two orders of magnitude: (a) at the top of the void and (b) at the bottom of void.

When photoionisation and secondary emission were omitted a positive streamer was found to form in the one dimensional case. This was because the streamer formed so rapidly, in approximately 3 ns, that the tail of the electron avalanche which formed when the initial seed charge moved through the void, was ahead of the ionising front. However, the ionising front was only found to propagate to the end of the electron avalanche tail,

approximately halfway across the air gap, see Figure C.5. The model was run for 1000 ns, and the peak number density locations were not found to change appreciably from this configuration. Due to the formation of the streamer the peak number densities were still comparable to those observed when secondary effects were included with similar surface charge density distributions. These observations were found to persist when the mesh element size was reduced by an order of magnitude. This suggests that it is not driven by numerical diffusion and it seems plausible that the tail of the electron avalanche could provide seed electrons to propagate a positive streamer a certain distance, if the streamer formation occurs over a very short timescale.

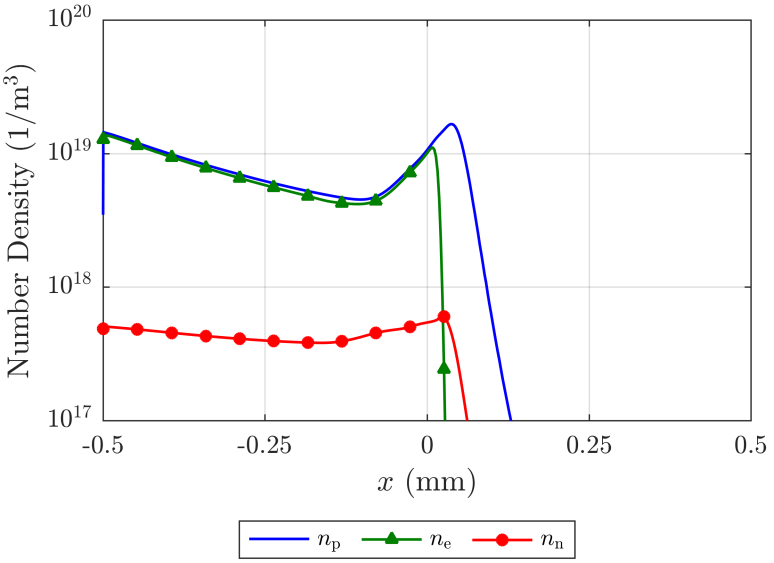

(a)

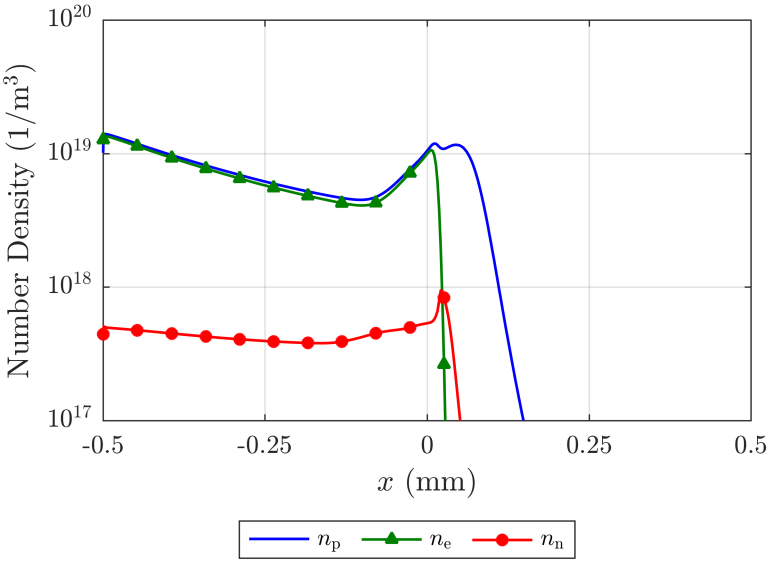

(b)

FIGURE C.5: Charged species number densities in the one dimensional model with secondary processes neglected at: (a) 4 ns and (b) 10 ns. This shows how the positive streamer propagates halfway across the void before stopping due to a lack of seed electrons ahead of the ionising front.

C.3 Conclusion

In the two dimensional model positive streamers were not formed in the cases where the breakdown voltage was slightly exceeded. The discharge consisted of an electron

avalanche, which is driven by collisional ionisation, followed by charge deployment at the dielectric barriers. In the one dimensional model positive streamers were found to occur in the simulation when the PD inception voltage was exceeded by 2 kV, but they were not found to propagate beyond the tail of the electron avalanche due to the lack of seed electrons when secondary processes are removed. This suggests that photoionisation is the mechanism by which positive streamer propagate across the voids in the simulation work conducted in this thesis, which is in agreement with the standard physical explanation in the literature [24].

Appendix D

Physical Constants

In this appendix a list of physical constants used in work is given. SI units are used throughout this report.

- $k_{\mathrm{B}} = 1.381... \times 10^{-23}$ J K^{-1} - Boltzmann constant
- $e = 1.602... \times 10^{-19}$ C - electron charge
- $m_{\mathrm{e}} = 9.109... \times 10^{-31}$ kg - electron mass
- $\nu_0 \approx 5 \times 10^{13}$ s^{-1} - fundamental phonon frequency
- $\varepsilon_0 = 8.854... \times 10^{-12}$ F m^{-1} - permittivity of free space

Appendix E

Transport Properties of Air

In this work the swarm parameters of air are set using the work of Kang [100]. They are as follows:

$$\alpha = 3.5 \times 10^5 \exp\left(\frac{-1.65 \times 10^5}{E}\right) \text{ m}^{-1} \tag{E.1}$$

$$\eta = 1500 \exp\left(\frac{-2.5 \times 10^4}{E}\right) \text{ m}^{-1} \tag{E.2}$$

$$\beta = 2 \times 10^{-13} \text{ m}^3 \text{ s}^{-1} \tag{E.3}$$

$$W_\text{e} = 60.6E^{0.75} \text{ m s}^{-1} \tag{E.4}$$

$$W_\text{p} = 0.027E \text{ m s}^{-1} \tag{E.5}$$

$$W_\text{n} = 0.0243E \text{ m s}^{-1} \tag{E.6}$$

$$D_\text{e} = 0.18 \text{ m}^2 \text{ s}^{-1} \tag{E.7}$$

where E is a dimensionless number corresponding to the magnitude of the electric field in units of V/cm, i.e.

$$E = \left|\vec{E}\right| \times 1 \text{ cm/V}.$$

Appendix F

Publications

The work conducted in this thesis led to the following publications:

1. G. Callender, J.A. Hunter, P. Rapisarda, and P.L. Lewin. Physical models for field based partial discharge measurements. In Electrical Insulation Conference, 2015. EIC 2015. IEEE, June 2015.

2. G. Callender, P. Rapisarda, and P.L. Lewin. Investigating the dependence of partial discharge activity on applied field structure. In Electrical Insulation Conference, 2016. EIC 2016. IEEE, June 2016.

3. G. Callender, P. Rapisarda, and P.L. Lewin. Investigation of void erosion on partial discharge activity using simulation. In International Conference on Dielectrics, 2016. ICD 2016. IEEE, July 2016.

4. G. Callender, P.L. Lewin, J.A. Hunter, and P. Rapisarda. Modeling partial discharge in a three-phase cable joint experiment with minimal adjustable parameters. IEEE Transactions on Dielectrics and Electrical Insulation, 24(1):279-287, 2017.

5. R.D. Nimmo, G. Callender, and P.L. Lewin. Methods for wavelet-based autonomous discrimination of multiple partial discharge sources. IEEE Transactions on Dielectrics and Electrical Insulation, 24(2):1131-1140, 2017

6. G. Callender, P. Rapisarda, and P.L. Lewin. Improving Models of Partial Discharge Activity using Simulation. In Electrical Insulation Conference, 2017. EIC 2017. IEEE, June 2017.

7. T. Tanmaneeprasert, P.L. Lewin and G. Callender. Analysis of Degradation Mechanisms of Silicone Insulation Containing a Spherical Cavity Using Partial Discharge Detection. In Electrical Insulation Conference, 2017. EIC 2017. IEEE, June 2017.

8. G. Callender, I.O. Golosnoy, P. Rapisarda, and P.L. Lewin. Critical analysis of partial discharge dynamics in air filled spherical voids. Journal of Physics D: Applied Physics, 51(12):125601, 2018.

References

[1] T.P. Hughes. *Networks of power: Electrification in Western Society, 1880-1930*. JHU Press, 1993.

[2] R.J. Van Brunt. Physics and chemistry of partial discharge and corona. recent advances and future challenges. *IEEE Transactions on Dielectrics and Electrical Insulation*, 1(5):761–784, 1994.

[3] L.A. Petrov, P.L. Lewin, and T. Czaszejko. On the applicability of nonlinear time series methods for partial discharge analysis. *IEEE Transactions on Dielectrics and Electrical Insulation*, 21(1):284–293, 2014.

[4] H.A. Illias, G. Chen, and P.L. Lewin. The influence of spherical cavity surface charge distribution on the sequence of partial discharge events. *Journal of Physics D: Applied Physics*, 44(24):245202, 2011.

[5] S. Kumara, Y.V. Serdyuk, and S.M. Gubanski. Surface charge decay on polymeric materials under different neutralization modes in air. *IEEE Transactions on Dielectrics and Electrical Insulation*, 18(5):1779–1788, 2011.

[6] K. Wu, C. Pan, Y. Meng, and Y. Cheng. Dynamic behavior of surface charge distribution during partial discharge sequences. *IEEE Transactions on Dielectrics and Electrical Insulation*, 20(2):612–619, 2013.

[7] T.N. Tran, I.O. Golosnoy, P.L. Lewin, and G.E. Georghiou. Numerical modelling of negative discharges in air with experimental validation. *Journal of Physics D: Applied Physics*, 44(1):015203, 2011.

[8] H.A. Illias, G. Chen, and P.L. Lewin. Partial discharge behavior within a spherical cavity in a solid dielectric material as a function of frequency and amplitude of the applied voltage. *IEEE Transactions on Dielectrics and Electrical Insulation*, 18(2): 432–443, 2011.

[9] F. Gutfleisch and L. Niemeyer. Measurement and simulation of PD in epoxy voids. *IEEE Transactions on Dielectrics and Electrical Insulation*, 2(5):729–743, 1995.

[10] L. Niemeyer, B. Fruth, and F. Gutfleisch. Simulation of partial discharges in insulation systems. In *High Voltage Engineering, 1991. 7th International Symposium on*, pages 25–28, 1991.

[11] G. Callender, P. Rapisarda, and P.L. Lewin. Investigation of void erosion on partial discharge activity using simulation. In *International Conference on Dielectrics, 2016. ICD 2016. IEEE*, July 2016.

[12] T. Tanmaneeprasert, P.L. Lewin, and G. Callender. Analysis of degradation mechanisms of silicone insulation containing a spherical cavity using partial discharge detection. In *Electrical Insulation Conference, 2017. EIC 2017. IEEE*, June 2015.

[13] G. Callender, P.L. Lewin, J.A. Hunter, and P. Rapisarda. Modeling partial discharge in a three-phase cable joint experiment with minimal adjustable parameters. *IEEE Transactions on Dielectrics and Electrical Insulation*, 24(1):279–287, 2017.

[14] G. Callender, J.A. Hunter, P. Rapisarda, and P.L. Lewin. Investigating the dependence of partial discharge activity on applied field structure. In *Electrical Insulation Conference, 2016. EIC 2016. IEEE*, June 2016.

[15] G. Callender, P. Rapisarda, and P.L. Lewin. Improving models of partial discharge activity using simulation. In *Electrical Insulation Conference, 2017. EIC 2017. IEEE*, June 2017.

[16] G. Callender, I.O. Golosnoy, P. Rapisarda, and P.L. Lewin. Critical analysis of partial discharge dynamics in air filled spherical voids. *Journal of Physics D: Applied Physics*, 51(12):125601, 2018.

[17] L. Niemeyer. A generalized approach to partial discharge modeling. *IEEE Transactions on Dielectrics and Electrical Insulation*, 2(4):510–528, 1995.

[18] M. Černák and T. Hosokawa. Initial stages of negative point-to-plane breakdown in helium. *Japanese Journal of Applied Physics*, 26(10):1721–1723, 1987.

[19] S.A. Boggs. Partial discharge iii: Cavity-induced pd in solid dielectrics. *IEEE Electrical Insulation Magazine*, 6(6):11–16, 1990.

[20] P.H.F Morshuis. *Partial discharge mechanisms.* PhD thesis, Delft University of Technology, 1993.

[21] R. Bartnikas. Partial discharges their mechanism, detection and measurement. *IEEE Transactions on Dielectrics and Electrical Insulation*, 9(5):763–808, 2002.

[22] L. Hao. *Partial Discharge Discrimination.* PhD thesis, University of Southampton, 2008.

[23] E. Kuffel, W.S. Zaengl, and J. Kuffel. *High Voltage Engineering: Fundamentals.* Butterworth-Heinemann, 2000.

[24] G.E. Georghiou, A.P. Papadakis, R. Morrow, and A.C. Metaxas. Numerical modelling of atmospheric pressure gas discharges leading to plasma production. *Journal of Physics D: Applied Physics*, 38(20):303, 2005.

[25] P.H.F. Morshuis. Partial discharge mechanisms in voids related to dielectric degradation. *Science, Measurement and Technology, IEE Proceedings*, 142(1):62–68, 1995.

[26] T. Ficker. Fractal multiplication of electron avalanches and streamers: new mechanism of electrical breakdown? *Journal of Physics D: Applied Physics*, 40(24): 7720–7733, 2007.

[27] S.A. Boggs. Partial discharge. ii. detection sensitivity. *IEEE Electrical Insulation Magazine*, 6(5):35–42, 1990.

[28] N. Oussalah, Y. Zebboudj, and S.A. Boggs. Analytic solutions for pulse propagation in shielded power cable for symmetric and asymmetric pd pulses. *IEEE Transactions on Dielectrics and Electrical Insulation*, 14(5):1264–1270, 2007.

[29] C.F. Jensen, U.S. Gudmundsdottir, C.L. Bak, and A. Abur. Field test and theoretical analysis of electromagnetic pulse propagation velocity on crossbonded cable systems. *Power Delivery, IEEE Transactions on*, 29(3):1028–1035, 2014.

[30] D. Evagorou, A. Kyprianou, P.L. Lewin, A. Stavrou, V. Efthymiou, and G.E. Georghiou. Classification of partial discharge signals using probabilistic neural network. In *Solid Dielectrics, 2007. IEEE International Conference on*, pages 609–615, July 2007.

[31] D. Nattrass. Partial discharge XVII: The early history of partial discharge research. *Electrical Insulation Magazine, IEEE*, 9(4):27–31, 1993.

[32] P.H.F. Morshuis and F.H. Kreuger. Transition from streamer to townsend mechanisms in dielectric voids. *Journal of Physics D: Applied Physics*, 23(12):1562, 1990.

[33] S. Whitehead. *Dieletric Breakdown of Solids*. Clarendon Press, Oxford, 1953.

[34] A. Alsheikhly and H.G. Kranz. A new approach for a basic understanding of pd phenomena. In *High Voltage Engineering, 1991. 7th International Symposium on*, pages 25–28, 1991.

[35] A. Alsheikhly, H. Guzman, and H.G. Kranz. A new diagnostic tool through computer simulation calculation using expanded partial discharge equivalent circuit. In *Conduction and Breakdown in Solid Dielectrics, 1992., Proceedings of the 4th International Conference on*, pages 176–180, June 1992.

[36] D.P. Agoris and N.D. Hatziargyriou. Approach to partial discharge development in closely coupled cavities embedded in solid dielectrics by the lumped capacitance model. *IEE Proceedings A - Science, Measurement and Technology*, 140(2):131–134, March 1993.

[37] I.W. McAllister. Electric field theory and the fallacy of void capacitance. *IEEE Transactions on Electrical Insulation*, 26(3):458–459, 1991.

[38] E. Lemke. A critical review of partial-discharge models. *IEEE Electrical Insulation Magazine*, 28(6):11–16, 2012.

[39] G.C. Crichton, P.W. Karlsson, and A. Pedersen. Partial discharges in ellipsoidal and spheroidal voids. *IEEE Transactions on Electrical Insulation*, 24(2):335–342, 1989.

[40] I.W. McAllister and A. Pedersen. Corona-onset field-strength calculations and the equivalent radius concept. *Archiv für Elektrotechnik*, 64(1):43–48, 1981.

[41] H.A. Boyd, F.M. Bruce, and D.J. Tedford. Sparkover in long uniform-field gaps. *Nature*, 210:719–720, 1966.

[42] I. Gallimberti. The mechanism of the long spark formation. *Journal de Physique Colloques*, 40(7):193–250, 1979.

[43] D.B. Hibbert and A.J.B. Robertson. The emission of electrons from glass induced by a strong electric field and the mechanism of the silent electric discharge. *Proceedings of the Royal Society of London A: Mathematical, Physical and Engineering Sciences*, 349(1656):63–79, 1976.

[44] C. Forssen and H. Edin. Partial discharges in a cavity at variable applied frequency part 2: measurements and modeling. *IEEE Transactions on Dielectrics and Electrical Insulation*, 15(6):1610–1616, 2008.

[45] A. Cavallini and G.C. Montanari. Effect of supply voltage frequency on testing of insulation system. *IEEE Transactions on Dielectrics and Electrical Insulation*, 13 (1):111–121, 2006.

[46] A. Cavallini, R. Ciani, M. Conti, P.H.F. Morshuis, and G.C. Montanari. Modeling memory phenomena for partial discharge processes in insulation cavities. In *Electrical Insulation and Dielectric Phenomena, 2003. Annual Report. Conference on*, pages 723–727, Oct 2003.

[47] H.A. Illias, M.A. Tunio, H. Mokhlis, G. Chen, and A.H.A. Bakar. Experiment and modeling of void discharges within dielectric insulation material under impulse voltage. *IEEE Transactions on Dielectrics and Electrical Insulation*, 22(4):2252–2260, 2015.

[48] H.A. Illias, M.A. Tunio, A.H.A. Bakar, H. Mokhlis, and G. Chen. Partial discharge phenomena within an artificial void in cable insulation geometry: experimental validation and simulation. *IEEE Transactions on Dielectrics and Electrical Insulation*, 23(1):451–459, 2016.

[49] *Partial discharge measurements.* IEC 60270, 1998.

[50] J. Kindersberger and C. Lederle. Surface charge decay on insulators in air and sulfurhexafluorid - part i: simulation. *IEEE Transactions on Dielectrics and Electrical Insulation*, 15(4):941–948, 2008.

[51] I.W. McAllister. Surface current density k: an introduction. *IEEE Transactions on Electrical Insulation*, 26(3):416–417, 1991.

[52] H.A. Illias. *Measurement and Simulation of Partial Discharges within a Spherical Cavity in a Solid Dielectric Material.* PhD thesis, University of Southampton, 2011.

[53] P. Dordizadeh, K. Adamiak, and G.S. Peter Castle. Study of the impact of photoionization on negative and positive needle-plane corona discharge in atmospheric air. *Plasma Sources Science and Technology*, 25(6):065009, 2016.

[54] P. Dordizadeh, K. Adamiak, and G.S. Peter Castle. Numerical investigation of the formation of trichel pulses in a needle-plane geometry. *Journal of Physics D: Applied Physics*, 48(41):415203, 2015.

[55] C. Lazarou, D. Koukounis, A.S. Chiper, C. Costin, I. Topala, and G.E. Georghiou. Numerical modeling of the effect of the level of nitrogen impurities in a helium parallel plate dielectric barrier discharge. *Plasma Sources Science and Technology*, 24(3):035012, 2015.

[56] C. Lazarou, T. Belmonte, A.S Chiper, and G.E. Georghiou. Numerical modelling of the effect of dry air traces in a helium parallel plate dielectric barrier discharge. *Plasma Sources Science and Technology*, 25(5):055023, 2016.

[57] Y.V. Serdyuk and S.M. Gubanski. Computer modeling of interaction of gas discharge plasma with solid dielectric barriers. *IEEE Transactions on Dielectrics and Electrical Insulation*, 12(4):725–735, 2005.

[58] D. Braun, V. Gibalov, and G. Pietsch. Two-dimensional modelling of the dielectric barrier discharge in air. *Plasma Sources Science and Technology*, 1(3):166, 1992.

[59] L. Testa, S. Serra, and G.C. Montanari. Advanced modeling of electron avalanche process in polymeric dielectric voids: Simulations and experimental validation. *Journal of Applied Physics*, 108(3):034110, 2010.

[60] C. Pan, Y. Meng, K. Wu, Z. Han, K. Qin, and Y. Cheng. Simulation of partial discharge sequences using fluid equations. *Journal of Physics D: Applied Physics*, 44(25):255201, 2011.

[61] A. Villa, L. Barbieri, M. Gondola, A.R. Leon-Garzon, and R. Malgesini. A pde-based partial discharge simulator. *Journal of Computational Physics*, 345:687–705, 2017.

[62] H.A. Illias, T.S. Yuan, A.H.A. Bakar, H. Mokhlis, G. Chen, and P.L. Lewin. Partial discharge patterns in high voltage insulation. In *Power and Energy, 2012. PECon 2012. IEEE International Conference on*, pages 750–755, December 2012.

[63] L. Niemeyer, L. Pietronero, and H. Wiesmann. Fractal dimension of dielectric breakdown. *Physical Review Letters*, 52:1033–1036, 1984.

[64] Y. Lim, J. Lee, W. Kang, and J. Koo. Chaotic analysis of partial discharge (capd) as a novel approach to investigate insulation degradation caused by the various defects. In *Industrial Electronics, 2001. IEEE International Symposium on*, volume 1, pages 413–416, June 2001.

[65] L. Yongfen, J. Haiying, H. Ping, and L. Yanming. Chaotic characteristic of time series of partial discharge in oil-paper insulation. *Plasma Science and Technology*, 13(6):740–746, 2011.

[66] A. Contin, M. Cacciari, and G.C. Montanari. Estimation of weibull distribution parameters for partial discharge inference. In *Electrical Insulation and Dielectric Phenomena, 1994., IEEE 1994 Annual Report., Conference on*, pages 71–78, Oct 1994.

[67] G.C. Montanari. Aging and life models for insulation systems based on pd detection. *IEEE Transactions on Dielectrics and Electrical Insulation*, 2(4):667–675, 1995.

[68] L.A. Dissado. Fractal processes and weibull statistics. In *Conduction and Breakdown in Solid Dielectrics, 1989., Proceedings of the 3rd International Conference on*, pages 538–532, Jul 1989.

[69] R. Altenburger, C. Heitz, and J. Timmer. Analysis of phase-resolved partial discharge patterns of voids based on a stochastic process approach. *Journal of Physics D: Applied Physics*, 35(11):1149, 2002.

[70] A. Contin, A. Cavallini, G.C. Montanari, G. Pasini, and F. Puletti. Digital detection and fuzzy classification of partial discharge signals. *IEEE Transactions on Dielectrics and Electrical Insulation*, 9(3):335–348, 2002.

[71] A. Contin and S. Pastore. Classification and separation of partial discharge signals by means of their auto-correlation function evaluation. *IEEE Transactions on Dielectrics and Electrical Insulation*, 16(6):1609–1622, 2009.

[72] L. Hao, P.L. Lewin, J.A. Hunter, D.J. Swaffield, A. Contin, C. Walton, and M. Michel. Discrimination of multiple pd sources using wavelet decomposition and principal component analysis. *IEEE Transactions on Dielectrics and Electrical Insulation*, 18(5):1702–1711, 2011.

[73] M. Ester, H. Kriegel, J. Sander, and X. Xu. A density-based algorithm for discovering clusters in large spatial databases with noise. In *KDD - 96 Proceedings*, pages 226–231. AAAI Press, 1996.

[74] A. Contin, S. Pastore, and R. Paganin. Evaluation of spaces for the separation of signals due to multiple pd sources. In *2015 IEEE Electrical Insulation Conference (EIC)*, pages 209–213, June 2015.

[75] R.D. Nimmo, G. Callender, and P.L. Lewin. Methods for wavelet-based autonomous discrimination of multiple partial discharge sources. *IEEE Transactions on Dielectrics and Electrical Insulation*, 24(2):1131–1140, 2017.

[76] J.A. Hunter. *An investigation into partial discharge activity within three-phase belted cables*. PhD thesis, University of Southampton, 2013.

[77] C. Pan, K. Wu, Y. Meng, Y. Cheng, and G. Meng. Variation of surface charge distribution in pd sequences. In *Electrical Insulation and Dielectric Phenomena, 2012. CEIDP 2012. Annual Report Conference on*, pages 52–55, Oct 2012.

[78] I.S. Grant and W.R. Phillips. *Electromagnetism*. Wiley, 2nd edition, 1990.

[79] C. Heitz. A generalized model for partial discharge processes based on a stochastic process approach. *Journal of Physics D: Applied Physics*, 32(9):1012–1023, 1999.

[80] S. Kumara, M. Bin, Y.V. Serdyuk, and S.M. Gubanski. Surface charge decay on htv silicone rubber: effect of material treatment by corona discharges. *IEEE Transactions on Dielectrics and Electrical Insulation*, 19(6):2189–2195, 2012.

[81] I.W. McAllister. Decay of charge deposited on the wall of gaseous void. *IEEE Transactions on Electrical Insulation*, 27(6):1202–1207, 1992.

[82] I.W. McAllister. Decay of charge deposited on the wall of a gaseous void. In *High Voltage Engineering, 1991. 7th International Symposium on*, pages 17–20, 1991.

[83] G. Chen and Z. Xu. Charge trapping and detrapping in polymeric materials. *Journal of Applied Physics*, 106(12):123707, 2009.

[84] T. Zhou, G. Chen, R. Liao, and Z. Xu. Charge trapping and detrapping in polymeric materials: Trapping parameters. *Journal of Applied Physics*, 110(4):043724, 2011.

[85] J. Shi, M. Famá, B.D. Teolis, and R.A. Baragiola. Ion-induced electrostatic charging of ice at 15–160 k. *Physical Review B*, 85:035424, 2012.

[86] C. Forssen. *Modelling of cavity partial discharges at variable applied frequency.* PhD thesis, KTH Royal Institute of Technology, 2008.

[87] L. Wang, A. Cavallini, G.C. Montanari, and L. Testa. Evolution of pd patterns in polyethylene insulation cavities under ac voltage. *IEEE Transactions on Dielectrics and Electrical Insulation*, 19(2):533–542, 2012.

[88] G. Callender, J.A. Hunter, P. Rapisarda, and P.L. Lewin. Physical models for field based partial discharge measurements. In *Electrical Insulation Conference, 2015. EIC 2015. IEEE*, June 2015.

[89] J.A. Hunter, L. Hao, P.L. Lewin, C. Walton, and M. Michel. Partial discharge diagnostics of defective medium voltage three-phase pilc cables. In *Electrical Insulation, 2012. ISEI 2012. IEEE International Symposium on*, pages 371–375, June 2012.

[90] J.A. Hunter, L. Hao, D.J. Swaffield, P.L. Lewin, N. Cornish, C. Walton, and M. Michel. Partial discharge in medium voltage three-phase cables. In *Electrical Insulation, 2010. ISEI 2010. IEEE International Symposium on*, pages 1–5, June 2010.

[91] D.J. Swaffield, P.L. Lewin, G. Chen, and S.G. Swingler. Partial discharge characterization of streamers in liquid nitrogen under applied ac voltages. *IEEE Transactions on Dielectrics and Electrical Insulation*, 15(3):635–646, 2008.

[92] L. Lundgaard, D. Linhjell, G. Berg, and S. Sigmond. Propagation of positive and negative streamers in oil with and without pressboard interfaces. *IEEE Transactions on Dielectrics and Electrical Insulation*, 5(3):388–395, 1998.

[93] T.N. Tran. *Surface Discharge Dynamics: Theory, Experiment and Simulation.* PhD thesis, University of Southampton, 2010.

[94] P.C.J.M. van der Wielen. *On-line Detection and Location of Partial Discharges in Medium-Voltage Power Cables.* PhD thesis, Eindhoven University of Technology, 2005.

[95] N.Y. Babaeva, D.V. Tereshonok, and G.V. Naidis. Initiation of breakdown in bubbles immersed in liquids: pre-existed charges versus bubble size. *Journal of Physics D: Applied Physics*, 48(35):355201, 2015.

[96] N.Y. Babaeva, G.V. Naidis, D.V. Tereshonok, and B.M. Smirnov. Streamer breakdown in elongated, compressed and tilted bubbles immersed in water. *Journal of Physics D: Applied Physics*, 50(36):364001, 2017.

[97] N.Y. Babaeva and M.J. Kushner. Structure of positive streamers inside gaseous bubbles immersed in liquids. *Journal of Physics D: Applied Physics*, 42(13):132003, 2009.

[98] Y.V. Yurgelenas and M.A. Leeva. Development of a barrier discharge in air in highly nonhomogeneous electric field caused by the residual dielectric surface charges. *IEEE Transactions on Plasma Science*, 37(6):809–815, 2009.

[99] I. Gallimberti. The mechanism of the long spark formation. *Journal de Physique Colloques*, 40(7):193–250, 1979.

[100] W.S. Kang, J.M. Park, Y. Kim, and S.H. Hong. Numerical study on influences of barrier arrangements on dielectric barrier discharge characteristics. *IEEE Transactions on Plasma Science*, 31(4):504–510, 2003.

[101] A. Bourdon, V.P. Pasko, N.Y. Liu, S. Célestin, P. Ségur, and E. Marode. Efficient models for photoionization produced by non-thermal gas discharges in air based on radiative transfer and the helmholtz equations. *Plasma Sources Science and Technology*, 16(3):656, 2007.

[102] M.B. Zhelezniak, A.K. Mnatsakanian, and S.V. Sizykh. Photoionization of nitrogen and oxygen mixtures by radiation from a gas discharge. *High Temperature Science*, 20(6):357–362, 1982.

[103] P. Ségur, A. Bourdon, E. Marode, D. Bessieres, and J.H. Paillol. The use of an improved eddington approximation to facilitate the calculation of photoionization in streamer discharges. *Plasma Sources Science and Technology*, 15(4):648, 2006.

[104] V. Nikonov, R. Bartnikas, and M.R. Wertheimer. The influence of dielectric surface charge distribution upon the partial discharge behavior in short air gaps. *IEEE Transactions on Plasma Science*, 29(6):866–874, 2001.

[105] N.Y. Babaeva and M.J. Kushner. Self-organization of single filaments and diffusive plasmas during a single pulse in dielectric-barrier discharges. *Plasma Sources Science and Technology*, 23(6):065047, 2014.

[106] P. Wang, H. Xu, J. Wang, A. Cavallini, and G.C. Montanari. The effects of asymmetry repetitive square wave voltages on pd statistics and endurance. In *International Conference on Dielectrics, 2016. ICD 2016. IEEE*, July 2016.

[107] P. Wang, A. Cavallini, G.C. Montanari, and G. Wu. Effect of rise time on pd pulse features under repetitive square wave voltages. *IEEE Transactions on Dielectrics and Electrical Insulation*, 20(1):245–254, 2013.

[108] M. Kaufhold, H. Aninger, M. Berth, J. Speck, and M. Eberhardt. Electrical stress and failure mechanism of the winding insulation in pwm-inverter-fed low-voltage induction motors. *IEEE Transactions on Industrial Electronics*, 47(2):396–402, 2000.

[109] M.S. Moonesan, S.H. Jayaram, and E.A. Cherney. Time to failure of medium-voltage form-wound machine turn insulation stressed by unipolar square waves. *IEEE Transactions on Dielectrics and Electrical Insulation*, 22(6):3118–3125, 2015.